Technische Universität München
Fakultät für Elektrotechnik und Informationstechnik

High Q nanomechanical resonators fabricated from crystalline silicon carbide

Yannick Sebastian Klaß

Vollständiger Abdruck der von der Fakultät für Elektrotechnik und Informationstechnik der Technischen Universität München zur Erlangung des akademischen Grades eines

Doktors der Naturwissenschaften (Dr. rer. nat.)

genehmigten Dissertation.

Vorsitzender:
Prof. Dr. Christian Jirauschek

Prüferinnen der Dissertation:
1. Prof. Dr. Eva Weig
2. Prof. Dr. Elke Scheer

Die Dissertation wurde am 14.06.2022 bei der Technischen Universität München eingereicht und durch die Fakultät für Elektrotechnik und Informationstechnik am 04.08.2022 angenommen.

Abstract

Nanomechanical resonators are widely used as sensors because they are highly susceptible to their surrounding environment. The performance or quality factor of these devices can, for instance, be boosted by increasing the tensile stress or decreasing the amount of material defects. Stressed crystalline materials are particularly interesting as they combine both methods and offer, therefore, unprecedented quality factors. Here, we investigate freely suspended doubly clamped nanomechanical string resonators fabricated from highly stressed crystalline 3C-SiC(111). We develop a new fabrication process that relies on a two step ICP-RIE process. The resulting string resonators are characterized with the help of piezo actuation and an interferometric detection scheme. We measure the Young's modulus with a method based on the eigenmode spectrum of nanomechanical string resonators, which is susceptible to the stress and crystal orientation of the corresponding strings. The resulting values of four different materials are compared to the literature, indicating that the Young's modulus depends on a wafer's growth conditions. We find a universal length dependence of the tensile stress in string resonators. Furthermore, we use an elastic model to describe our findings, revealing that minor geometry adaptions can already boost the stress significantly.

We analyze the quality factor as a function of the length and mode number. An advanced dissipation dilution model developed by Ignacio Wilson-Rae describes our findings almost perfectly. With the extracted dissipation factor from the model and the measured quality factors, we calculate the loss angle and find it to be constant over a wide frequency range.

We measure the string resonator's dissipation and frequency between 4 K and room temperature. The measurements suggest thermally activated defects at 180 K. Furthermore, a hysteresis-like behavior at 23 K is analyzed and compared to another

crystalline material.
Additionally, we implement a dielectric driving scheme that allows tuning of the frequency and dissipation by applying a dc voltage. Finally, the temperature dependence of the an asymmetric avoided crossing of two mechanical modes is discussed.

Zusammenfassung

In dieser Arbeit werden doppelt eingespannte nanomechanische Saitenresonatoren aus stark verspanntem kristallinem 3C-SiC(111) untersucht. Wir entwickeln ein zuverlässiges Herstellungsverfahren, das auf einem neuen zweistufigen ICP-RIE Rezept beruht. Die Saitenresonatoren werden mittels eines Piezoantriebs und einem interferometrischen Ausleseverfahren charakterisiert. In einem nächsten Schritt messen wir das Elastizitätsmodul mit einer neu entwickelten Methode, die auf dem Eigenmodenspektrum der Saitenresonatoren basiert. Dadurch reagiert dieses Verfahren insbesondere auf Stressänderungen im Resonator. Wir ermitteln das Elastizitätsmodul für vier unterschiedliche Materialien und vergleichen diese mit Literaturwerten. Es zeigt sich, dass das Elastizitätsmodul von den Wachstumsbedingungen des Wafers abhängt.
Mithilfe der Euler-Bernoulli Balkentheorie bestimmen wir die Zugpannung von Saitenresonatoren. Wir zeigen für mehrere Materialien eine Längenabhängigkeit der Zugpannung. Zur Beschreibung unserer Ergebnisse wird ein elastisches Modell verwendet, welches zeigt, dass bereits geringe Geometrieanpassungen die Zugpannung deutlich erhöhen können.
Wir messen den Qualitätsfaktor in Abhängigkeit der Länge und der Modennummer. Ein neues, von Ignacio Wilson-Rae entwickeltes, Modell beschreibt unsere Ergebnisse nahezu perfekt. Mit den extrahierten Parametern aus dem Modell und den gemessenen Qualitätsfaktoren berechnen wir die Verluste (loss angle) und stellen fest, dass sie über einen breiten Frequenzbereich konstant sind.
Wir messen die Verluste und die Frequenz des String-Resonators für Temperaturen zwischen 4 K und Raumtemperatur. Die Messungen deuten auf thermisch aktivierte Defekte bei circa 180 K hin. Außerdem diskutieren wir ein hystereseähnliches Verhalten bei 23 K und vergleichen es mit dem Verhalten eines anderen kristalli-

nen Materials. Zusätzlich implementieren wir ein dielektrisches Antriebsschema, welches die Verschiebung der Frequenz und der Dämpfung durch Anlegen einer Spannung ermöglicht. Zuletzt diskutieren wir die Temperaturabhängigkeit der Kopplung zwischen zwei mechanischen Moden.

Contents

1 Introduction

In 1824, J. J. Berzelius accidentally discovered silicon carbide (SiC) during an attempt to produce diamonds.[1–3] Although it was quickly realized that this novel material has exceptional properties, silicon was favored for applications due to an easier fabrication process.[3] Today, nearly every electronic device features at least a few silicon based components.[4] One big branch are microelectromechanical systems (MEMS), which are used as sensors for e.g. pressure and acceleration.[4] Hidden from our eyes, these sensors decide when to deploy a car's airbag, count steps in a smartwatch, and measure the tilting angle in our smartphone. However, Si sensors are not very well suited for applications with high powers, high voltages, or high temperatures. Since SiC excels exactly under these circumstances, the interest in SiC was reignited over 150 years after its discovery.[3,5–7] Initially, SiC MEMS sensors have especially been deployed for gas turbines and combustion engines, where the sensors have to withstand temperatures above 400 °C.[3,6–8] Nowadays, a plethora of different sensors exist, harnessing, among others, SiC's high breakdown field, excellent physical stability, and chemical inertness.[3,5–7,9,10]

Shrinking the size of sensors from micro- to nanometers brings us in the domain of nanoelectromechanical systems (NEMS). The reduced mass allows for ultra low mass,[11–16], force[17,18], and torque sensing,[19,20] with a precision in the yoctogram, zeptonewton and yoctonewtonmeter regime, respectively. One particular NEMS system is a doubly clamped freely suspended string resonator. Introducing tensile stress to the resonator boosts the quality factor, an important figure of merit in the NEMS community, that is closely related to the inverse of the dissipation. Many of these devices are fabricated from amorphous silicon nitride[21–26] and offer very high quality factors.[26] However, crystalline materials, such as SiC, offer a lower defect density and should therefore be able to outperform their SiN counterparts.[27–30] On top of that, the high yield strength[31] and the immense crystal-lattice mismatch between SiC and Si promise a very high tensile stress. Indeed, first measurements

on SiC nanoresonators confirm exceptional quality factors.[27,28] Because SiC is a comparatively new material in nanomechnaics, many material parameters, that are well known for Si or SiN, are still unknown for SiC.[32] In this work we try to further incorporate this amazing material in the field of nanomechanics. More specifically, we analyze doubly clamped freely suspended nanomechanical string resonators fabricated from highly stressed 3C-SiC(111).

The structure of the thesis is as follows: In Chap. 2 the relevant basic theory is introduced. We discuss a string resonator's behavior in the Euler-Bernoulli beam theory framework. Approximating the string by a harmonic oscillator allows us to determine the amplitude response and the quality factor. Additionally, we discuss the dissipation dilution model, the dielectric driving scheme and the coupling of mechanical modes. Chapter 3 starts with a general introduction to SiC. Furthermore, the fabrication process is presented in detail, including our new two step ICP-RIE process to release the string resonators. Our measurement setups for room and low temperatures are discussed in Chap. 4. Additionally, we characterize several string resonators and compare different measurement techniques. In Chap. 5, we present a novel method to extract the Young's modulus from the eigenmode spectrum of the string resonators. This, in turn, allows us to determine the tensile stress, which is discussed in Chap. 6. Additionally, the length dependence of the tensile stress is analyzed with the help of an elastic model, which can be used for further stress engineering. The quality factor as a function of mode number is discussed in Chap. 7 with the help of an advanced loss dilution model developed by Ignacio Wilson-Rae. With the extracted dilution factor and the measured quality factor, we can calculate the loss angle over a frequency span of 80 MHz. In Chap. 8 we take a closer look at the temperature dependence of a string resonator's dissipation and frequency. As discussed in Chap. 8, we implement a dielectric driving scheme with SiC and analyze the avoided crossing of two mechanical modes.

2 Theory Basics

2.1 Nanomechanical String Resonators

The structures analyzed in this thesis are doubly clamped nanomechanical string resonators, which consist of a freely suspended string held in place by two clamping pads as schematically shown in Fig. 2.1. In order to be classified as *nano*, at least one dimension has to be below one micron.[33] As the typical thickness h and width w of our resonators are in the range of (a few) 100 nm, this definition is well fulfilled. The length L, on the other hand, is between 10 and 100 µm.

String resonators have two dominant vibrating directions, namely the out-of-plane (oop) and in-plane (ip) direction as visualized in Fig. 2.1. The mechanical modes of beams (and strings[a]) can be mathematically described by the Euler-Bernoulli

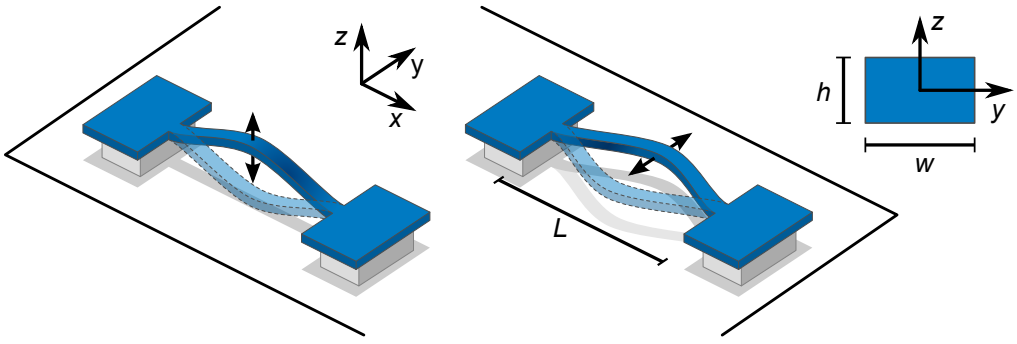

Figure 2.1: Visualization of the fundamental out-of-plane (left) and in-plane (right) modes of a string resonator with length L. The width w and thickness h are shown on the string's cross-section. Adapted from Ref. [34].

[a] Strings are beams under tensile stress.

beam theory, developed in the 18th century by Euler and Bernoulli.[35] A detailed derivation will be omitted at this point but can be found in many books, such as Refs. [33, 36–38]. The theory works best for prismatic beams ($L/h > 10$) with negligible rotational inertia and shear deformation.[33,38] Assuming a doubly clamped beam with tensile stress σ that consists of a linear elastic material (i.e. it obeys Hooke's law), the equation of motion is:[33]

$$EI\frac{\partial^4 u(x,t)}{\partial x^4} - \sigma A\frac{\partial^2 u(x,t)}{\partial x^2} + \rho A\frac{\partial^2 u(x,t)}{\partial t^2} = 0, \tag{2.1}$$

where $u(x,t)$ is the displacement, x the position along the beam, t the time, E Young's modulus, I the area moment of inertia, A the beams's cross section, and ρ the density. This equation can be solved analytically for simply supported boundary conditions (see Fig. 2.2), yielding the theoretical eigenfrequency of the oop mode[33,36,37]

$$f_n = \frac{n^2\pi}{2L^2}\sqrt{\frac{Eh^2}{12\rho}}\sqrt{1+\frac{12\sigma L^2}{n^2\pi^2 Eh^2}}, \tag{2.2}$$

where n is the mode number. If $\frac{12\sigma L^2}{n^2\pi^2 Eh^2} \gg 1$,[b] which holds for a high tensile stress and low mode numbers, Eq. (2.2) simplifies to the string model

$$f_n \approx \frac{n}{2L}\sqrt{\frac{\sigma}{\rho}}. \tag{2.3}$$

As expected from this equation and confirmed by measurements on stress dominated strings, the frequency scales approximately linearly with the mode number n.[39] For a 110 µm long string, for which we measure a frequency of 2.69 MHz, both Eq. (2.2) and (2.3) predict a frequency of 2.79 MHz. This is in agreement with the literature, where it has been reported that the Euler-Bernoulli beam theory slightly overestimates the eigenfrequencies of beam resonators.[35,40]

Simply supported boundary conditions (vanishing curvature at the clamping points, see Fig. 2.2) are valid to determine the eigenfrequencies of strings with negligible flexural rigidity, which is normally a good approximation for strings with high tensile stress.[33] The mode shape of real string resonators, however, is not reproduced correctly, especially close to the clamping points, where the finite flexural rigidity leads to a local bending at the clamping pads.[41] This issue is better addressed by employing doubly clamped boundary conditions (vanishing slope at the clamping points, see Fig. 2.2), which provide a better approximation to the real beam shape. However, the mathematical complexity increases drastically and the equation of motion is therefore solved numerically. In Chap. 7 we present an analytical approximation that is acquired via Taylor expansion.

[b] The flexural rigidity of the string is neglected.

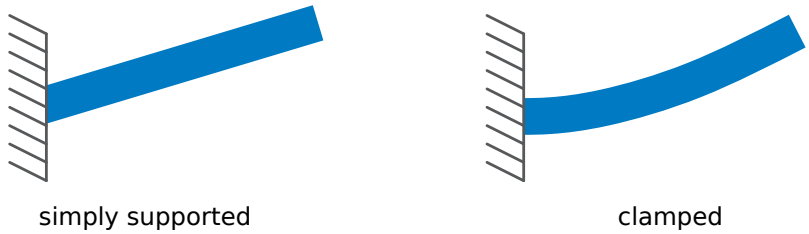

Figure 2.2: Schematic of simply supported (left, vanishing curvature at the clamping points) and clamped (right, vanishing slope at the clamping points) boundary conditions. The latter reproduces the mode shape of an actual string resonator more accurately by including the local bending close to the clamping pads.

2.2 Driven Harmonic Resonator

The behavior of a driven and damped nanomechanical string resonator can be described with the help of a harmonic oscillator. A detailed discussion and derivation can be found for instance in Refs. [33, 37]. For that, the resonator is reduced to a point mass with effective mass m, which depends on the real mass, the resonator's geometry, and the mode in question. For the fundamental oop mode of a doubly clamped string resonator, the effective mass corresponds to half the real physical mass and is located in the center of the antinode.[33,42] For a driven and damped resonator in the linear regime, we get the equation of motion

$$\ddot{z} + \Gamma\dot{z} + \omega_0^2 z = \frac{\tilde{F}}{m}, \tag{2.4}$$

where z is the displacement, Γ the damping rate, $\omega_0 = 2\pi f_0$ the eigenfrequency (i.e. the frequency without damping), and $\tilde{F} = F_d \cos(w_d t)$ the drive at the frequency ω_d. Solving the complexified version[c] of the differential Eq. (2.4) with the ansatz $z(t) = z_0 \exp(i\omega_d t)$ gives us the amplitude response A[33,43]

$$A(\omega_d) = |z_0| = \frac{F_d}{m\sqrt{\left(\omega_0^2 - \omega_d^2\right)^2 + \Gamma^2\omega_d^2}} \tag{2.5}$$

of the driven resonator. The power response (or intensity), which is A^2, and the amplitude response correspond to a Lorentzian and the square root of a Lorentzian function, respectively.

The sharpness of a resonance curve is determined by the damping Γ. A higher damping results in a flatter curve, as visualized in Fig. 2.3. Another figure of

[c]The complexified version reads $\ddot{z} + \Gamma\dot{z} + \omega_0^2 z = \frac{F_d}{m}\exp(i\omega_d t)$.

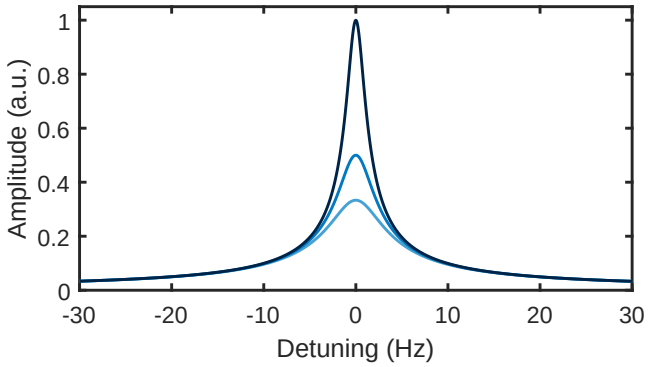

Figure 2.3: Calculated amplitude response (see Eq. (2.5)) as a function of detuning $(\omega_d - \omega_0)$ around the resonance frequency for three different damping rates Γ.

merit, which is closely related to the damping, is the quality factor Q. It is defined as the ratio of stored energy W to dissipated energy ΔW during one resonance cycle:[33]

$$Q = 2\pi \frac{W}{\Delta W} = \frac{\omega_0}{\Gamma} \sqrt{1 - \frac{\Gamma^2}{2\omega_0^2}}. \tag{2.6}$$

In case of high Q resonators (i.e. $\frac{\Gamma^2}{2\omega_0^2} \ll 1$), Eq. (2.6) can be reduced to

$$Q \approx \frac{\omega_0}{\Gamma} = \frac{\omega_0}{\Delta\omega}, \tag{2.7}$$

where $\Delta\omega$ is the full width at half maximum. A reliable method to determine the quality factor (or damping) of a resonator is to fit the square root of a Lorentzian to its amplitude response.

Ring down measurements are another possibility to extract the quality factor. They are particularly useful for very high Q resonators, where the recording of resonance curves gets increasingly difficult due to the low required bandwidth (see Sec. C). To that end, we measure the amplitude or energy decay over time. Fitting an exponential function of the form

$$\begin{aligned} |z(t)| &\propto \exp\left(-\frac{t - t_0}{2\tau}\right) \qquad \text{(amplitude decay)}, \\ |z(t)|^2 &\propto \exp\left(-\frac{t - t_0}{\tau}\right) \qquad \text{(energy decay)} \end{aligned} \tag{2.8}$$

yields the decay time $\tau = \Gamma^{-1}$, from which we can calculate the quality factor or damping. Here, t_0 corresponds to the time at which the power is switched off as explained in more detail in Sec. C.

2.3 Dissipation Dilution

Stressed nanomechanical systems outperform their unstressed counterparts by several orders of magnitude in terms of quality factors, but the underlying mechanism remained elusive until the concept of dissipation dilution was introduced. The basic idea routes back to González et al., who worked on a mass suspended by an inelastic wire in the course of the LIGO project.[44,45] One decade later, Unterreithmeier et al. explained the mode dependent damping of highly stressed silicon nitride (SiN) string resonators via an oscillation of the local strain[46] and in 2012 Yu et al. introduced the dissipation dilution model as it is known today.[47]

The oscillation of a string resonator gives rise to a strain and stress spatial distribution as visualized in Fig. 2.4 (b). If they are not perfectly in phase, energy is dissipated, which can mathematically be described with a complex Young's modulus $\tilde{E}$:[46]

$$\tilde{E} = E_{\mathrm{Re}} + iE_{\mathrm{Im}}. \tag{2.9}$$

Here, $E_{\mathrm{Re}} = E$ is the conventional Young's modulus (also called storage modulus), which is in phase with the strain, and E_{Im} is the so called loss modulus, which is out of phase with the strain.[48] Assuming δ to be the phase between stress and strain, the loss tangent $\tan(\delta)$ can be written as[48]

$$\tan(\delta) = \frac{E_{\mathrm{Im}}}{E_{\mathrm{Re}}} = Q_{\mathrm{intr}}^{-1}, \tag{2.10}$$

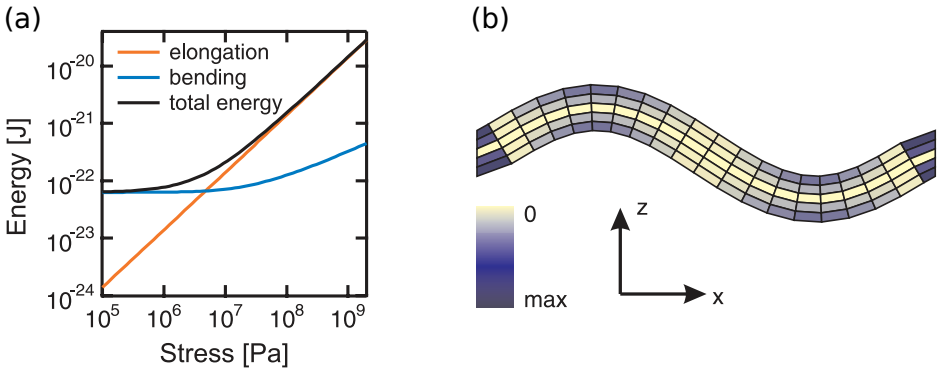

Figure 2.4: (a) Elastic energies as a function of the tensile stress for a 35 µm string resonator. In the model by Unterrethmeier et al. the Euler-Bernoulli beam theory is solved numerically for doubly-clamped boundary conditions. Therefore, it does take into account the bending close to the clamping points. (b) Color coded strain distribution of the second mode of a string resonator.
Reprinted figure with permission from Ref. [46]. Copyright (2022) by the American Physical Society. Small adaptations in (a).

where Q_{intr} is the intrinsic quality factor of the material (i.e. an unstressed version of the resonator). Note that Q_{intr} is frequency independent as shown in Chap. 7 and Refs. [49, 50].
As we know from Eq. (2.6), the quality factor is the total stored energy divided by the dissipated energy during one oscillation cycle. The stored energy can be divided into a part originating from the bending and a part from the overall elongation.[51] The dissipated energy, on the other hand, is only proportional to the bending energy but does not depend on the elongation energy.[46] Furthermore, the elongation energy scales linearly with the tensile stress while the bending energy depends only very weakly on it as shown in Fig. 2.4 (a). Therefore, the stored energy increases much faster than the dissipation when the tensile stress raises. In other words, a higher tensile stress leads to a higher quality factor. In order to obtain quantitative values with this theory, we have to take into account the local bending at the clamping pads.[46] To this end the Euler-Bernoulli beam theory has to be solved with the boundary conditions of a doubly clamped beam, which requires numerical methods as demonstrated in the work by Unterreithmeier et al.[51].
The dissipation dilution model from Yu et al., on the other hand, gives us the quality factor without the need for numerical calculations. Here, the intrinsic quality factor of a stressed string resonator is given analytically by[47,52]

$$Q_{\text{intr},\sigma} = Q_{\text{intr}} \left(\underbrace{2\lambda}_{\text{clamping}} + \underbrace{n^2\pi^2\lambda^2}_{\text{antinode}} \right)^{-1} \quad \text{with} \quad \lambda = \frac{h}{L}\sqrt{\frac{E}{12\sigma}}, \tag{2.11}$$

where n is the mode number, h the thickness, L the length, and σ the tensile stress. The expression in brackets enhances Q_{intr} for $\lambda \ll 1$, which holds true for stressed string resonators,[d], and is therefore called enhancement factor or dilution factor. It is composed of two contributions: The left term originates from the curvature of the string close to the clamping points and the right term from the bending of the antinodes.[52] As $\lambda \ll 1$ for the string resonator considered in this work, the left term (bending at the clamping pads) is dominant for small mode numbers. However, since the right term depends on the mode number n, it dominates $Q_{\text{intr},\sigma}$ for high mode numbers.

2.4 Dielectric Actuation Scheme

In 2009 Unterreithmeier et al.[51] presented the on-chip dielectric driving scheme that we employ in this work. In comparison to a magnetomotive[53] or capacitive[54–56]

[d]For a typical SiC string resonator ($h = 110\,\text{nm}$ $L = 110\,\mu\text{m}$, $\sigma = 1.1\,\text{GPa}$) as used in this work, $\lambda \approx 0.0055$.

drive, it does not require a metallized resonator, which would increase the damping.[56–58] A direct current (dc) voltage U_{dc} applied to a set of electrodes, which are placed adjacent to the string resonator, gives rise to an inhomogeneous electric field, polarizing the dielectric resonator. This polarization effect can be well approximated by dipoles which interact with the electric field $\vec{E}$ and are, thus, subject to the force $\vec{F}$[59]

$$\vec{F} = \vec{p}\,\nabla\vec{E}, \tag{2.12}$$

where $\vec{p} = \alpha\vec{E}$ is the electric dipole moment and α the polarizability. This force, which is known as Kelvin polarization force,[e] pulls the string resonator towards the highest field gradient.[41] Note that the force would vanish for a homogeneous electric field ($\nabla\vec{E} = 0$). To this end, the electrodes are placed with a small vertical and horizontal offset with respect to the resonator, resulting in an inhomogeneous electric field in the vicinity of the resonator. If an additional radio frequency (rf) voltage U_{rf} is applied to the electrodes, this force is modulated and the resonator is actuated. The resulting force can be approximated by[51]

$$F\left(U_{\mathrm{dc}} + U_{\mathrm{rf}}\right) \propto \left(U_{\mathrm{dc}} + U_{\mathrm{rf}}\right)^2 \approx U_{\mathrm{dc}}^2 + 2U_{\mathrm{dc}}U_{\mathrm{rf}}. \tag{2.13}$$

Both U_{dc} and U_{rf} influence the strength of the drive: While the rf voltage drives the oscillation of the resonator, the dc voltage independently controls the strength of the polarization.[51] Hence, for $U_{\mathrm{dc}} = 0\,\mathrm{V}$ the driving force vanishes completely.[f] As derived in Ref. [63], the dc voltage gives rise to an additional electrically induced spring constant k_e, which influences the resonance frequency:

$$f(k_e) = \frac{1}{2\pi}\frac{\sqrt{k_0 + k_e}}{m} \approx f_0 + c_{\mathrm{dc}}U_{\mathrm{dc}}^2, \tag{2.14}$$

where f_0 is the resonance frequency for zero dc voltage and c_{dc} is a parameter, depending, among others, on the sample geometry, frequency, and mass. For our sample geometry, c_{dc} has a different sign for the oop and ip mode, i.e. they tune in different frequency directions as demonstrated in Sec. 9.1.

Interestingly, not only the frequency but also the damping (and thus the quality factor) is affected by the applied dc voltage. Similar to Eq. (2.14), we get a quadratic dependence of the total damping[63]

$$\Gamma = \Gamma_0 + \Gamma_{\mathrm{d}}(U_{\mathrm{dc}}) = \Gamma_0 + c_\Gamma U_{\mathrm{dc}}^2 \tag{2.15}$$

on the dc voltage. Here, Γ_0 is the damping with zero dc voltage, Γ_{d} the dielectric damping, and c_Γ a constant that is closely related to c_{dc}.

[e] The same mechanism is used in biophysics to manipulate and control particles.[60–62]

[f] In Eq. (2.13) we neglected the term U_{rf}^2, which is valid for the drive powers used in this work. Note that it would actuate at twice the drive frequency as we get $U_{\mathrm{rf}}^2 = \left(U_d\cos(\omega_d t)\right)^2 = \frac{U_d^2}{2}\left(\cos(2\omega_d t) + 1\right)$ for a drive of the form $U_{\mathrm{rf}} = U_d\cos(\omega_d t)$.

2.4.1 Dielectric Coupling of Two Mechanical Modes

The following section is mostly based on my Master's thesis:

Y. S. Klaß, *"Multi-electrode geometries for refined dielectric control of nanoelectromechanical systems"*, Master's thesis at Universität Konstanz (2017). Ref. [64].

The text of this work was written by me and therefore the following section contains original passages.

The strong coupling regime can be reached with a plethora of different systems, e.g. coupling of a single photon to a superconducting qubit,[65] a mechanical mode to an optical cavity,[66,67] a single quantum dot to a cavity,[68–70], an atom to a microresonator,[71] and different mechanical modes of a drum resonator.[72] Generally speaking, the strong coupling regime requires the coupling rate Γ_c to exceed the damping rate Γ of the system. Mathematically, this corresponds to the relation

$$\Gamma_c \gg \Gamma. \tag{2.16}$$

In our experiment, we have strong coupling between the mechanical oop and ip mode, similar to the findings of Refs. [23, 73, 74]. Due to the rectangular cross-section of the string, the frequencies of the oop and ip mode are separated by approximately 100 kHz when no voltage is applied. However, by applying a dc voltage, we can tune both modes into resonance, where they are able to exchange energy. As expected from the strong coupling regime, the frequency of the modes do not cross but repel each other, leading to the typical avoided crossing (see Sec. 9.2). The coupling of those mechanical modes can be described with the help of the differential equations of two coupled harmonic oscillators.[73,75] For the sake of simplicity, the detailed calculations will be omitted at this point. The frequency splitting is given by[73]

$$\Gamma_c = \sqrt{\frac{k_0 + 2k_c}{m}} - \sqrt{\frac{k_0}{m}}, \tag{2.17}$$

where m is the string's effective mass, k_c the coupling spring constant, and k_0 the spring constant at the voltage with zero detuning.

3 SiC – a Novel Material for Nanomechanics

3.1 Basic Information about SiC

SiC is a IV-IV semiconductor formed by silicon (Si) and carbon (C) atoms bonded in a tetrahedron as depicted in Fig. 3.1 (a). Each tetrahedron has four Si atoms at the corners and one C atom in the middle (or equivalently four C atoms and one Si atom). The distance between Si-Si (or C-C) atoms is 3.08 Å[76] and the distance between neighboring Si-C atoms is 1.89 Å.[76–78] As typical for a tetrahedron, the angles Si-Si-Si and Si-C-Si (also called tetrahedral bond angle) are $\alpha = 60°$ and $\beta = 109.5°$, respectively.

Because the atomic order is fixed in two dimensions, we have bilayers[a] of Si-C as can be seen in Fig. 3.1 (d,e).[5,6,80–82] In the remaining direction, however, the bilayers can form different stacking sequences, defining the unit cell of the corresponding polytype. To maintain the tetrahedral bonds, each bilayer can only be oriented in three ways, denoted as A, B, and C, with the restriction that it can not match the orientation of its neighboring bilayers, as visualized in Fig. 3.1 (c).[76] This one dimensional polymorphism is called polytypism.[7,81,83] In total, there exist over 250 polytypes, some of them with stacking sequences of hundreds of bilayers.[81,83] Among all these, the most relevant polytypes are 4H-SiC, 6H-SiC and 3C-SiC.[81,84] Here, the number indicates the periodicity in the stacking sequence and the following letter the crystal symmetry (C - cubic, H - hexagonal, and R - rhombohedral). Historically, SiC with a cubic symmetry is also called β-SiC and SiC with a hexagonal or rhombohedral symmetry is called α-SiC. For example, 6H-SiC has a stacking order of ABCACB ABCACB . . . with hexagonal symmetry (Fig. 3.1 (e)). 3C-SiC, on the other hand, has a stacking

[a] Note that each tetrahedron contributes with three Si atoms and one C atom to this bilayer. The remaining Si atom belongs already to the next bilayer.

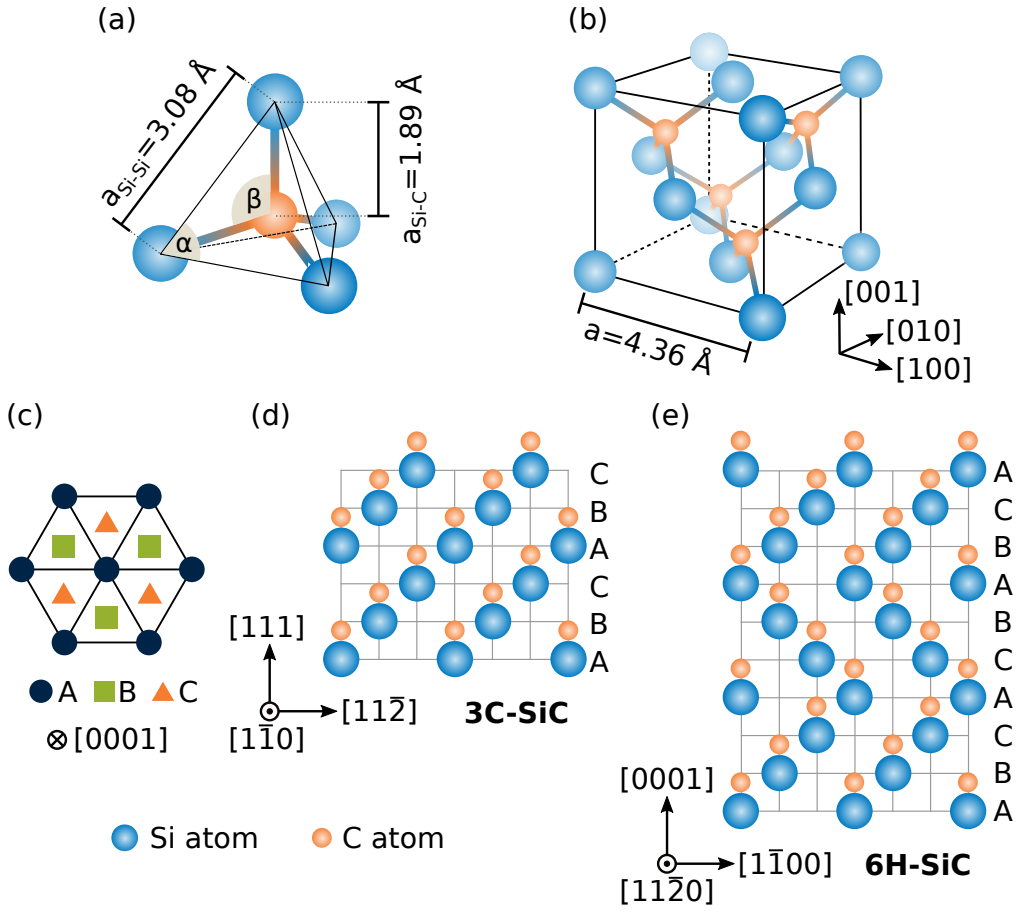

Figure 3.1: (a) Tetrahedron composed of three Si atoms in the corners and one C atom in the middle. The distance between Si-Si (or C-C) atoms is $a_{\text{Si-Si}} = 3.08$ Å[76] and the distance between neighboring Si-C atoms is $a_{\text{Si-C}} = 1.89$ Å.[76–78] The angle Si-Si-Si is $\alpha = 60°$ and the angle Si-C-Si $\beta = 109.5°$. (b) Visualization of the 3C-SiC zinc blende structure, which exhibits a lattice constant of $a_{3C} = 4.36$ Å.[76,77,79] Note how the unit cell is constructed from multiple tetrahedrons. (c) Different lattice sites that can be occupied by the Si-C bilayers are denoted as A,B, and C. (d,e) Stacking sequence of 3C-SiC (d) and 6H-SiC (e). In horizontal direction there is only one stacking order possible, ABC ABC . . ., no matter the polytype.
(c) Adapted from Ref. [76]. (d,e) Adapted from Refs. [5, 80].

order of ABC ABC . . . (Fig. 3.1 (d)) and it is the only known polytype with a cubic symmetry (zinc blende) as schematically depicted in Fig. 3.1 (b).[7] Although based on the same material, different polytypes exhibit different physical properties. The indirect band gap for instance ranges from 2.4 eV (3C-SiC) to 3.0 eV (6H-SiC) to 3.2 eV (4H-SiC).[6] Furthermore, SiC is one of the hardest elements on earth with a

Mohs hardness of 9.[84] Due to its high chemical resistance, it can be employed in very harsh environments.[84]

3.1.1 Thin Film 3C-SiC on Si

Epitaxial growth of thin film 3C-SiC[b] on Si is a challenging task due to the immense lattice mismatch of approximately 20 %, which has been leading to unsatisfactory results for decades (e.g. cracks, nonuniform layers).[86–88] In 1982 Shigehiro et al.[87] laid the foundation for the modern SiC deposition technique by introducing a buffer layer between Si and SiC. A (low pressure) chemical vapor deposition (LPCVD) reactor, whose working principle is explained in Ref. [89], is used for a two step growing procedure that we describe in the following.[c]

First, a buffer layer is generated by carbonization[d] of silicon.[87,88,90] For that purpose, the CVD reactor is rapidly heated up to around 1000 °C[e] and supplied with a hydrocarbon gas (e.g. C_3H_8 or C_2H_2), that serves as a carbon source.[87,90] The C atoms penetrate the Si wafer's surface and form a SiC buffer layer.[91,92] By changing different parameters during the carbonization process, the resulting layer's properties (thickness, appearance, roughness) can be altered significantly.[89,92] Hu et al. reported that the carbonized thickness and the C/Si atomic ratio saturate at approximately 1.4 nm and 0.9 - 1, respectively, after eight minutes of carbonization.[92] Additionally, it is shown that both under and over carbonization reduces the quality of the later grown SiC film.[92] The carbonization process gives rise to defects in the Si-SiC interface that are called voids or etch pits.[88,91,93,94] They have a triangular shape on Si(111) surfaces as shown in Fig. 3.2. For Si(100), on the other hand, they are smaller and have a square shape.[88,93,94] It is widely accepted that these voids form by out diffusion of Si from the substrate.[88,91,94,95] Fine tuning the carbonization parameters can reduce the number of voids significantly[88] or make them disappear entirely.[95] Second, crystalline 3C-SiC is grown on top of the buffer layer. For that the reactor is again heated to approximately 1000 °C and silane (e.g. SiH_4) and hydrocarbon gases (e.g. C_3H_8 or C_2H_2) serve as Si and C sources.[87–91] Importantly, the Si substrate dictates the crystalline direction of the SiC film, i.e. SiC(111) grows on Si(111) and SiC(100) on Si(100).[96] By regulating the temperature, atomic ratio of the incoming C/Si atoms, and other parameters the properties of the SiC film can be altered as explained in Sec. 3.1.2 for the tensile

[b] 4H- and 6H-SiC can also be grown epitaxially. For that, however, a hexagonal substrate is required, as discussed in Refs. [84, 85].

[c] Before these two steps, a cleaning step normally takes place, which is not described here.

[d] Sometimes it is also called nucleation

[e] In the literature there exist many recipes with vastly different carbonization times, temperatures, and gases. The given number is just an order of magnitude.

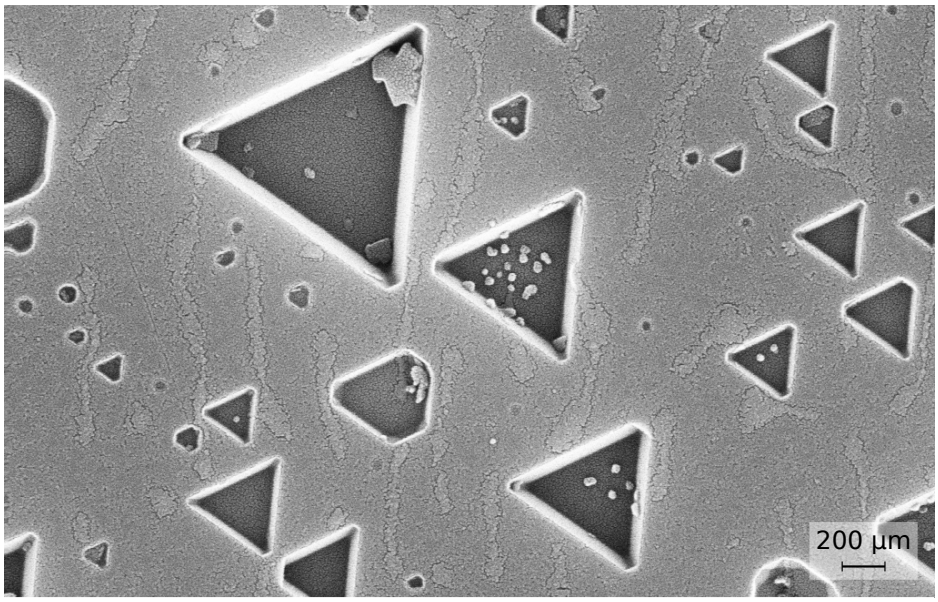

Figure 3.2: SEM image of the Si(111) surface after the removal of the overlying 3C-SiC(111). One can clearly see the typical triangular voids that originate from the carbonization process.

stress.[84,91,95,97–100]

3.1.2 Tensile Stress in 3C-SiC Films

To achieve the best possible mechanical quality factors, it is crucial to have a high tensile stress in the device layer as already discussed in Sec. 2.3. Normally, the stress of crystalline materials can be calculated via the lattice mismatch of the substrate and the device layer.[101] For SiC, however, the immense lattice mismatch demands a buffer layer as explained in the previous Sec. 3.1.1. Therefore, we can not determine the tensile stress from the crystal structure. In the literature one can find some information about what kind of material, orientation, and growing parameters should be used to achieve the maximal tensile stress.
Although SiC(111) and SiC(100) should, in principle, feature a similar lattice mismatch and thermal expansion coefficient (and thus a similar stress), Iacopi et al.[96] demonstrated that SiC(111) films exhibit a significantly higher tensile stress. To be more precise, for a thickness of 60 nm they found a stress of 360 MPa for SiC(100) and a stress of 900 MPa for SiC(111). The difference can be attributed to a more efficient stress relief via defects (e.g. stacking faults) in SiC(111).[96]
The thickness of the film is another possibility to manipulate the residual stress of SiC. It has been shown that the carbonization layer is highly compressed with

up to 800 MPa. To this end, really thin films (< 25 nm) exhibit a compressive or very small tensile stress.[95] Increasing the thickness to around 200 nm also raises the tensile stress continuously for SiC(111).[95] For SiC(100), on the other hand, the stress decreases slightly from 100 nm onward.[95] For thicknesses in the micrometer regime, the tensile stress of SiC(111) remains relatively constant, while it drops to approximately 180 MPa for SiC(100).[96] Again, this can be explained with the more efficient stress relief via stacking faults.
For the sake of completeness, it should also be mentioned that the atomic ratio C/Si during the growth,[97,102], the growth duration,[97,103], the carbonization temperature,[96] the growth temperature,[96,100,103] and the location on the wafer (the tensile stress is higher in the center of the wafer)[103] significantly affect the tensile stress. In conclusion, to maximize the tensile stress, we would need a SiC(111) wafer that has been grown with a high C/Si atomic ratio, a high carbonization temperature, a high growth temperature, a thickness of around 150(50) nm, and with a long growth duration (small growth rate).

3.2 Fabrication Process

Developing the top-down fabrication process of doubly clamped, highly stressed string resonators made out of 3C-SiC(111) has been one of the major parts of this thesis. Our wafers consist of approximately 110 nm SiC epitaxially grown on top of 1000 µm Si by NovaSiC. All wafers used during my work are listed in App. A. To ensure evenly sized chips with clean edges, the wafers are diced up in squares of 5×5 mm^2 by Wafer & Glassubstrate Dicing GmbH & Co. KG, as indicated in Fig. 3.3. These chips are the basis for all further fabrication steps. In Sec. 3.2.1 and 3.2.2 the fabrication process for strings only and strings with adjacent electrodes is presented, respectively. Both are summarized tabularly in App. B.

3.2.1 A Harp of Strings

The harp like structure employed in this work hosts a set of eleven resonators with lengths ranging from 10 µm to 110 µm in steps of 10 µm, as visualized in Fig. 3.4. The required fabrication steps are explained in the next sections.

Labeling and Cleaning

Because SiC is a crystalline material, where certain material parameters like the tensile stress and the Young's modulus can depend on the crystal direction, it is important to know the crystal orientation. To this end, many wafers feature a flat,

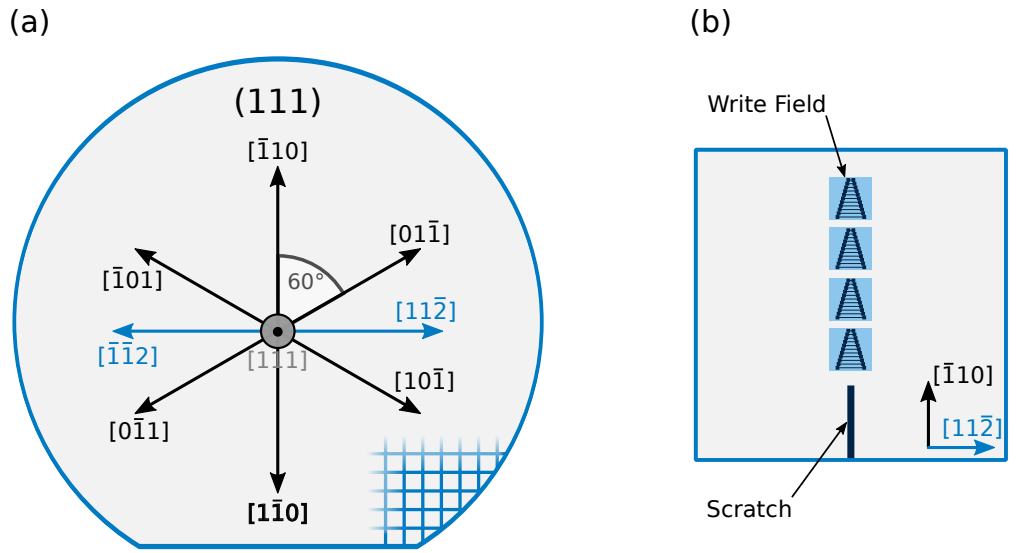

Figure 3.3: Visualization of important crystal directions for a (111)-Wafer. The wafer's flat marks the $[11\bar{2}]$ direction. On the bottom right, the individual squared chips are indicated. A zoomed-in version of one of them can be seen in (b), showing the scratch, which is used to preserve knowledge about the crystal directions, and four write fields (blue squares).

marking a particular crystal direction. For our (111) wafers, the flat is parallel to the $[11\bar{2}]$ direction, as visualized in Fig. 3.3 (a). At the very beginning of our fabrication process, the 5×5 mm^2 chip is marked with a scratch perpendicular to the wafer's flat (i.e. parallel to the $[\bar{1}10]$ direction) on the side closer to the flat. On the backside, it is additionally labeled with a unique code. After that, it is thoroughly cleaned in acetone and isopropyl alcohol (IPA) to provide a clean surface for the upcoming processing, cf. Fig. 3.5 (a).

Electron Beam Lithography for Resonators

For our structure, it is sufficient to deposit a single layer of electron beam resist. A spin coater is used to get a uniform 450 nm polymethyl methacrylate[f] (PMMA) layer on the clean chip. This is achieved with a 30 s spin at a speed of 5000 rpm. It is important to thoroughly clean the chip's underside with acetone in order to avoid PMMA residues that would lead to a slight tilt in the upcoming lithography step. By placing the chip for 90 s on a 180 °C hot plate, the PMMA is tempered. No conductive layer (like chromium or electra[g]) is required because the silicon substrate features a sufficient conductivity. This holds true for all tested SiC wafers,

[f] Allresist PMMA 950k A6 (672.06)
[g] Allresist Protective Coating PMMA-Electra 92

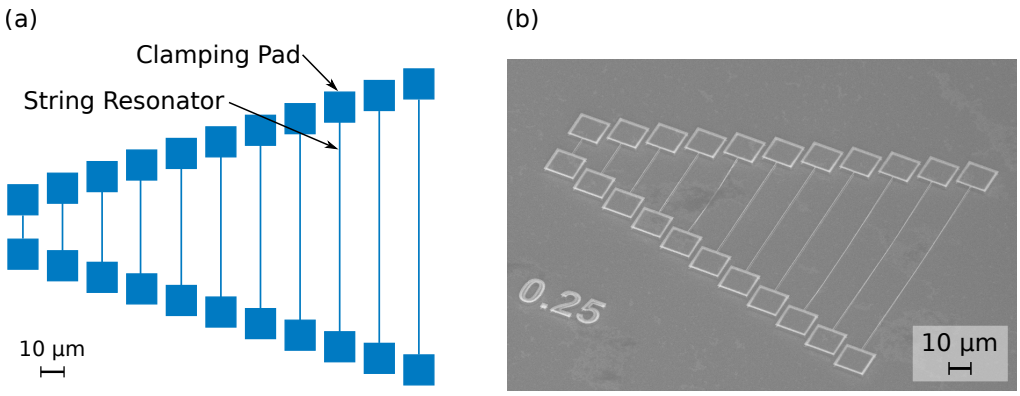

Figure 3.4: (a) Lithographic structure of string resonators with a length ranging from 10 µm up to 110 µm in steps of 10 µm. (b) SEM image of a finished sample showing the harp like structure. Note that undercut areas at the edge of the clamping pads appear white.

even those not intentionally doped.
All structures presented in this work have been exposed with a Zeiss Crossbeam 1540XB with the software neomicra smile 2 at the University of Konstanz. Dose tests have been used to fine tune the exposure parameters. We recommend the following settings: a working distance of 8.6 mm, an acceleration voltage of 10 kV, an aperture of 20 µm, a dose of 170 µC cm^{-2} for the clamping pads and 255 µC cm^{-2} for the string resonators. Since PMMA is a positive resist and we use later Cr as an etch mask, we expose the areas where the resonators will later be located, as visualized in Fig. 3.5 (b). To develop the sample, it is first dipped in MIBK:IPA (1:3) for 50 s and then in IPA to stop the development process. This removes the previously exposed resist.

Evaporation of the Resonator Etch Mask

Thermal or electron beam evaporation is used to deposit a 30 nm chromium etch mask on the sample, as shown in Fig. 3.5 (c). We recommend an evaporation rate of 1 Å s^{-1}. In Sec. 3.3.2, we discuss the difference between an etch mask made out of aluminum (Al) and Cr.
The PMMA and the chromium on top are removed by placing the sample in acetone in an ultrasonic bath set to the lowest power for approximately five minutes. After this lift-off step (Fig. 3.5 (d)), we clean the sample in IPA for another two minutes. Cutting the lift-off procedure short can result in residual chromium sticking to the surface.

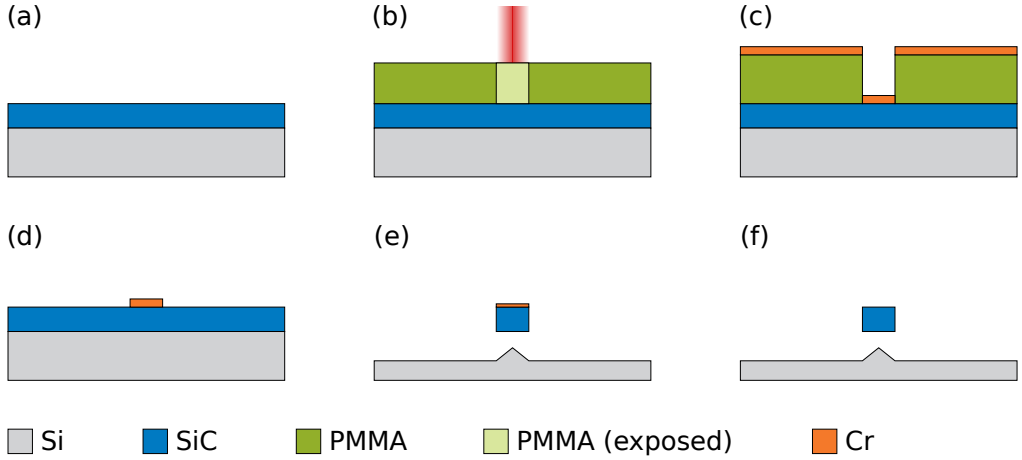

Figure 3.5: Step-by-step explanation of the fabrication of a doubly clamped string resonator made out of 3C-SiC(111) without any electrodes. Different colors correspond to different materials. The individual figures show: (a) blank chip, (b) electron beam lithography of a PMMA covered chip, (c) evaporation of chromium, (d) lift-off, (e) ICP-RIE step, and (f) final removal of the chromium etching mask.

Releasing the Resonator

Inductively coupled plasma reactive ion etching (ICP-RIE)[h] is utilized to define the structure laterally and to undercut the string resonators. For that we run a process with the gases sulfur hexafluoride SF_6 and argon Ar for 150 s at 10 °C. Here, we take advantage of the fact that silicon is etched not only vertically but also horizontally during this process. After the ICP-RIE step, the string resonator is already fully released, as displayed in Fig. 3.5 (e). The chromium etch mask, which is still partially on the sample, reacts with the SF_6, rendering it very resilient against chemical removal. To circumvent this problem a followup ICP-RIE argon mill is used to remove the affected layer of chromium. For that purpose a 45 s etch at 10 °C is sufficient. More details about the exact settings of the ICP-RIE and the ICP-RIE etching step in general can be found in App. B and Sec. 3.3, respectively. Next, we have to remove the chromium etch mask from our structures. The chip is immersed in IPA and afterward transferred into two consecutive water baths. A 40 s dip in Chromium Etchant[i] removes the remaining etch mask. Again two consecutive water baths are utilized to clean the sample thoroughly before immersing it in IPA again. When moving the chip between two beakers, always ensure that a small droplet of liquid remains on it. Otherwise, the surface tension

[h] ICP-RIE Oxford Plasmalab 100
[i] Transene Company Inc. Chromium Etchant 1020

could damage the fragile resonators.
In the last step, the sample is dried with the help of a Critical Point Dryer.[j] Here, IPA is slowly exchanged with liquid CO_2 and then heated under high pressure to reach the supercritical phase. The pressure is slowly released to bring it to the gas phase. Like this, we avoid the harmful surface tension. A schematic of the finished sample can be seen in Fig. 3.5 (f). Fig. 3.4 (b) shows an SEM image of a finished harp.

3.2.2 Strings with Adjacent Electrodes

In order to apply the dielectric drive that our group is employing for silicon nitrite strings, we need two adjacent electrodes next to the resonators. After a lot of refinement, the lithographic design converged to the one shown in Fig. 3.6 (a,b). Compared to the string only design, we have notably enlarged the clamping pads to compensate for longer ICP etching times, which are needed to reliably undercut the resonators. Furthermore, we have increased the width of the electrodes (compared to designs used for SiN, see e.g. Refs. [64, 104]) to prevent a full undercut of the electrodes, which would detach them from the underlying material.
While some fabrication steps are identical to those presented in Sec. 3.2.1, some vary a bit or are completely new. For the sake of completeness, all fabrication steps are mentioned, but only the new ones are elaborated.

Labeling and Cleaning

This step remains completely unchanged. The sample is labeled and scratched to preserve the knowledge about the crystal orientation. Then it is cleaned in acetone and IPA.

Electron Beam Lithography for Electrodes

We start with fabricating the electrodes and alignment markers.[k] As described in detail in Sec. 3.2.1, PMMA is applied via spin coating at a speed of 5000 rpm and afterward tempered on the hotplate. To reduce the SEM's writing time, we use two different apertures, namely 20 µm and 60 µm. It is essential to align them to each other as they normally have a slight offset. Details regarding this alignment can be found in the manual of the respective SEM software. First, the delicate

[j] Baltec CPD 030

[k] Note that we can not easily change the fabrication order. It is important that we first process the electrodes as they are made out of gold, which is well visible in the SEM. The etch mask for the strings, on the other hand, is made out of chromium, which is hardly visible in the SEM. Hence, aligning the electrodes and strings would be much more difficult.

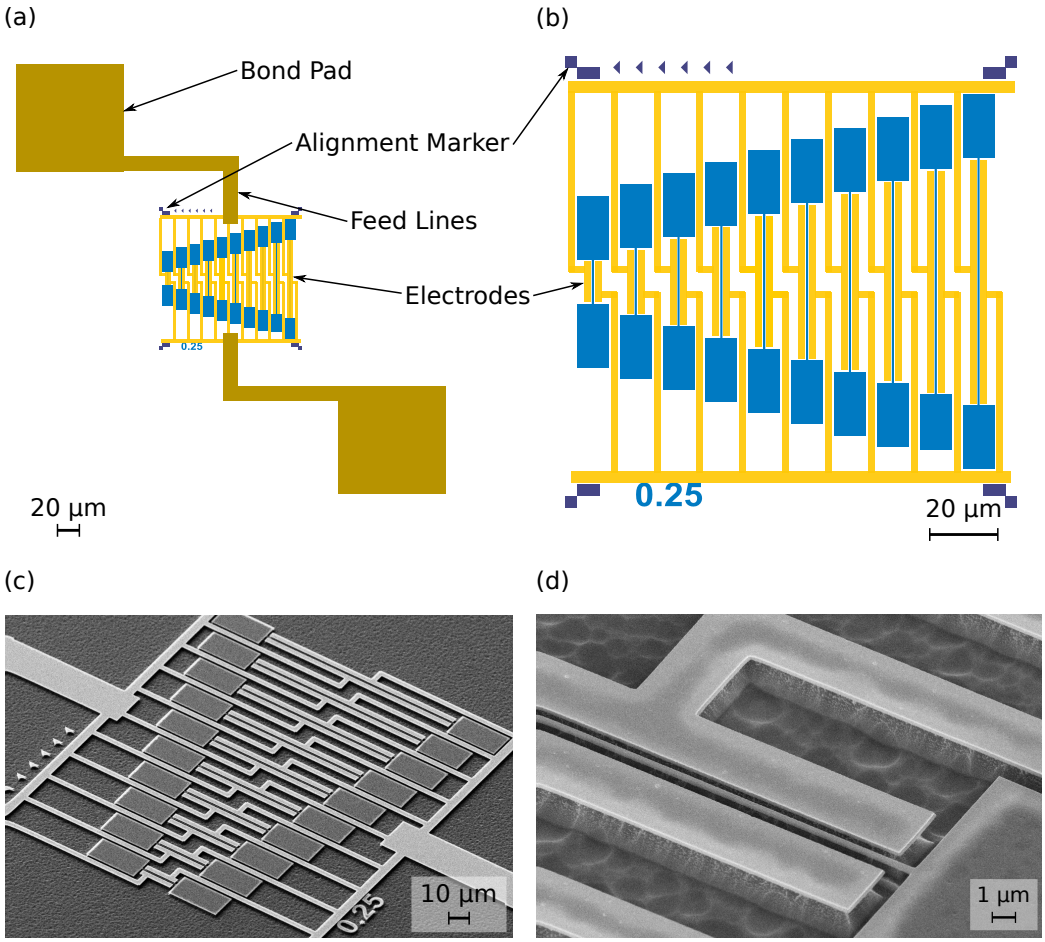

Figure 3.6: (a) Schematic write field of strings with adjacent electrodes. Blue corresponds to clamping pads and string resonators, purple to alignment markers, light yellow to electrodes, and dark yellow to bond pads. The blue digits *0.25* reflect the nominal width of the string resonators. For easier alignment a set of triangles (purple) pointing to the first marker are present. The dark yellow bond pads are written with an aperture of 60 µm and the remaining structure is written with a 20 µm aperture. A zoomed-in version of the inner structure can be seen in (b). SEM images of finished samples are shown in (c) and (d). On (d) one can clearly see that the string resonator is underetched.

electrodes and markers (light yellow and purple in Fig. 3.6 (a)) are written with the high resolution 20 µm aperture, as visualized in Fig. 3.7 (b). Second, the large bond pads and feed lines to the electrodes (dark yellow in Fig. 3.6 (a)) are written with the faster 60 µm aperture. To accommodate a small offset of the structures written with the two different apertures, an overlap of the big leads and the electrodes are included in the design (see Fig. 3.6 (a)).

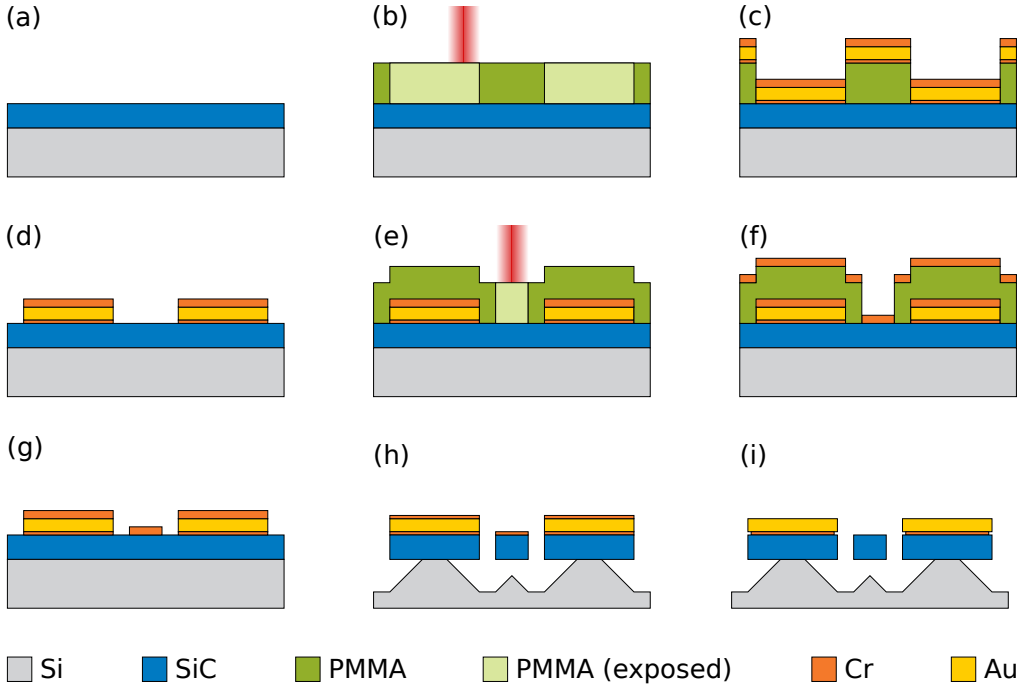

Figure 3.7: Step-by-step explanation of the fabrication of a doubly clamped string resonator made out of 3C-SiC(111) with adjacent gold electrodes. Different colors correspond to different materials. The individual figures schematically show: (a) blank chip, (b) electron beam lithography for the electrodes and markers, (c) evaporation of chromium and gold, (d) lift-off, (e) electron beam lithography for the string resonators, (f) evaporation of chromium, (g) lift-off, (h) ICP-RIE step, and (i) final removing of the chromium etch mask.

Afterward, we develop the sample in MIBK:IPA for 50 s and stop the development process with a rinse in IPA.

Evaporation of the Electrodes

Thermal or electron beam evaporation is used to deposit 5 nm[1] of chromium, 50 nm of gold, and 30 nm of chromium on the sample. In Fig. 3.7 (c) one can see a visualization of this stack. We recommend an evaporation rate of 1 Å s^{-1} for both chromium and gold. While the first thin layer of chromium serves as an adhesive layer between SiC and gold, the second thicker layer of Cr corresponds to an etch mask for the electrodes. In a lift-off process, we remove the remaining PMMA together with the metal layers on top, as presented in Fig. 3.7 (d).

[1]We have found that 5 nm Cr offer considerable more adhesion than 3 nm.

Adding String Resonators

Now we can exactly follow the steps presented in Sec. 3.2.1 with one little exception: In the SEM we have to precisely align the strings to the already existing electrodes. Note that we can not simply take a look at the whole structure as this would expose the PMMA. Therefore, we only scan the close vicinity of the four alignment markers and manually mark the center of each of them.[m] Based on these marks, the software is able to determine the location of the electrodes by correcting for tilt, magnification, and lateral and horizontal offset. This correction has to be repeated every time the stage is moved, e.g. when going to a different write field. After the alignment, we can now fabricate the string resonator exactly as described earlier in Sec. 3.2.1. This means we write the string with the 20 µm aperture (Fig. 3.7 (e)), develop the sample, evaporate 30 nm of chromium (Fig. 3.7 (f)), perform the lift-off (Fig. 3.7 (g)), run an ICP-RIE etch (Fig. 3.7 (h)), remove the remaining chromium layer (Fig. 3.7 (i)), and finally dry the sample in the CPD. Fig. 3.6 (c) and (d) show SEM micrographs of finished samples with electrodes.

3.3 ICP-RIE Etch

The ICP-RIE etch step is a crucial part of our fabrication process, in which SiC and Si are etched anisotropic and isotropic, respectively. A detailed analysis of the etching of Si in a SF_6 ICP-RIE step can be found in Refs. [105–107]. Panduranga et al.[105] have analyzed the isotropy of a SF_6 etching step for different structures. It turns out that Si is approximately etched twice as fast in vertical than in horizontal direction. The exact value, however, depends on the etching time, the employed ICP-RIE recipe, and the distance between the structures. To be more precise: the shorter the distance between two etched structures, the lower the isotropy.[105]

3.3.1 Determining the ICP-RIE Etch Rate

In order to develop a working ICP-RIE recipe to fabricate string resonators, it is crucial to know the etch rate of SiC. For that purpose, we create a sample with multiple rectangular aluminum (Al) structures with both a width and a distance to each other of 10 µm. The Al serves as an etch mask. Then we etch the sample for a certain time span, remove the Al, and measure the step height of multiple rectangles.

[m] For the initial localization of a new write field, we are always searching for the top left marker. For this purpose, we have guiding triangles that lead towards the correct marker, as visualized in Fig. 3.6 (b). As soon as this marker is successfully located, we can easily find the remaining three markers and scan them for alignment.

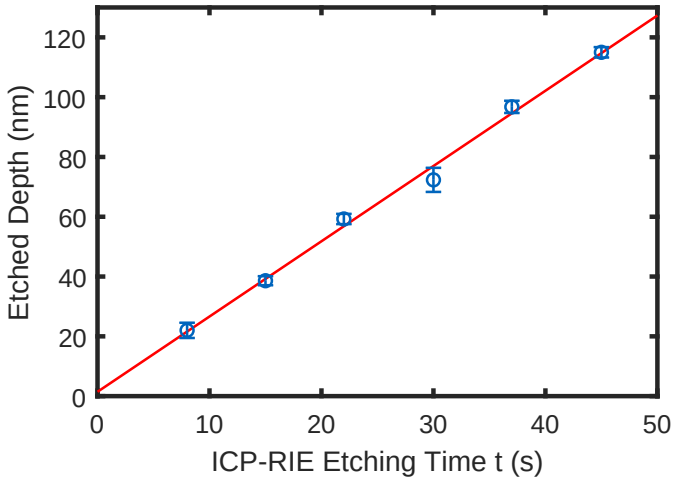

Figure 3.8: Etched depth as function of the ICP-RIE etch time for a SiC sample. Blue dotes and error bars correspond to the mean and the standard deviation, respectively. The red line is a linear fit with the equation $2.5\,\mathrm{nm\,s^{-1}} \cdot t + 1.5\,\mathrm{nm}$. For etching we used our SF_6 and Ar recipe on a sample consisting of 110 nm 3C-SiC(111) on top of Si(111) substrate (Wafer A, see App. A).

From that data we calculate the mean and standard deviation and repeat the same procedure for six different times t. The resulting plot can be seen in Fig. 3.8. Note that the SiC has a thickness of 110 nm, i.e. after a 45 s etch we just breach the SiC-Si interface. As expected, we get a linear dependence between etching time and depth. Fitting the data with a linear function yields $2.5\,\mathrm{nm\,s^{-1}} \cdot t + 1.5\,\mathrm{nm}$, i.e. we have an etch rate of $2.5\,\mathrm{nm\,s^{-1}}$ or $150\,\mathrm{nm\,min^{-1}}$.

3.3.2 Chromium vs. Aluminum Etch Mask

Here, we compare chromium and aluminum as a material for etch masks. As the etch masks directly imprint their smoothness on the underlying material (this could be a resonator, clamping pad, or electrode) during the ICP-RIE etch, it is crucial for them to have smooth edges. Resonators with rough edges have reduced quality factors. While Cr delivers really smooth edges, Al has a rough surface with big clusters as clearly visible in Fig. 3.9. To improve the overall smoothness for Al, we have tried various countermeasures: First, we tried to increase the evaporation rate from $1\,\mathrm{Å\,s^{-1}}$ to $2\,\mathrm{Å\,s^{-1}}$, the resulting structure is depicted in Fig. 3.9 (c). The higher rate results in more grain and bigger clusters and, therefore, a rougher resonator. This is in agreement with Bordo and Rubahn[108] who analyzed the dependency of the evaporation rate (from $1\,\mathrm{Å\,s^{-1}}$ to $20\,\mathrm{Å\,s^{-1}}$) on the grain size and smoothness for evaporated Al. They found that a reduction of the evaporation rate benefits

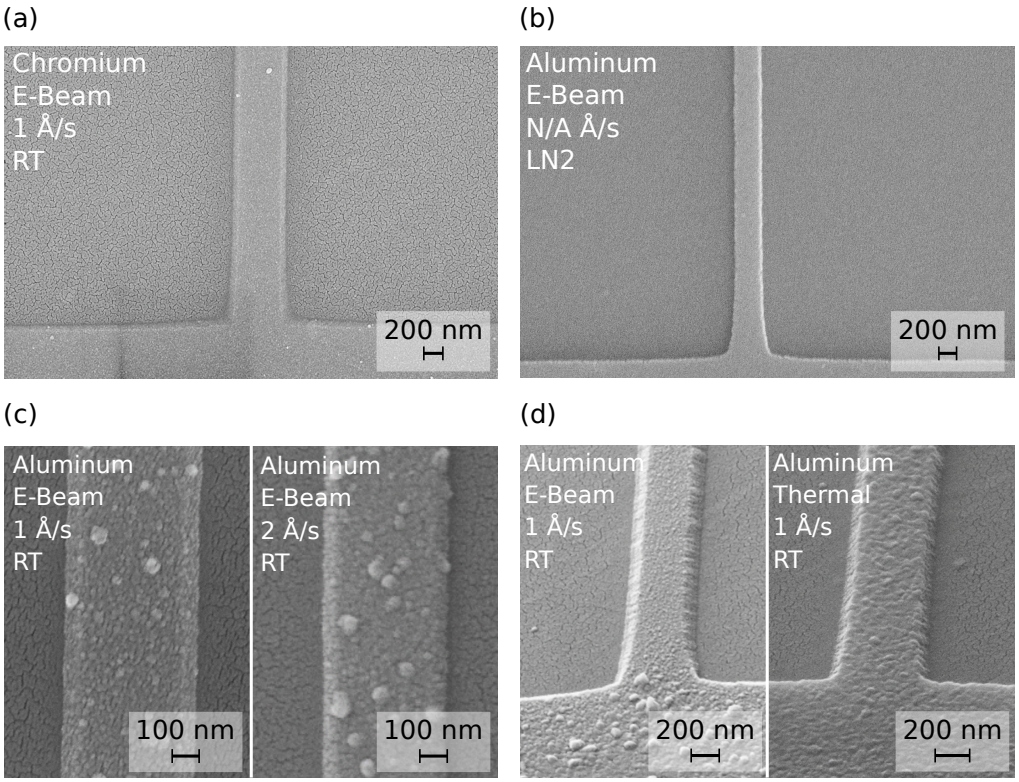

Figure 3.9: SEM images of etch masks fabricated out of chromium (a) and aluminum (b-d). On (a,b,d) one can see the transition between the etch mask for the clamp (bottom part of the images) and for the string resonator (upper part of the images). On (c), just a small section of the string is displayed. White text on the upper left side of all the images indicate the settings used for the corresponding evaporation process, where *E-Beam* stands for electron beam evaporation, *Thermal* for thermal evaporation, *RT* for room temperature, and LN_2 for liquid nitrogen temperature. (a) and (b) show the best etch mask we can fabricate with the respective material. (c) and (d) compare two evaporation rates and two evaporation methods, respectively. The small cracks originate from gold sputtering, which increases the contrast and prohibits charging effects in the SEM. This is necessary as all samples are made out of SiN on fused silica.

the smoothness.[108] We have not tried to evaporate slower than 1 Å s^{-1}, but this could potentially increase the smoothness. Second, we compared electron beam and thermal evaporation, as displayed in Fig. 3.9 (d). Thermal evaporation offers noticeable smaller clusters and an overall smoother etch mask, but it still has some surface roughness. Lastly, we tried to cool the sample with liquid nitrogen (LN_2) during electron beam evaporation. This was done by my colleague Anh Tuan Le in

Prof. Dr. Elke Scheer's laboratory at the University of Konstanz. Unfortunately, we are not able to recall the evaporation rate. As can be seen in Fig. 3.9 (b), evaporating on a cooled sample nearly completely eliminates the formation of clusters. The edges are the smoothest of all the tried methods, but still it can not compete with the nearly perfect surface of evaporated chromium (see Fig. 3.9 (a)). Additionally, cooling the sample to LN_2 temperature is also time consuming.
Note that cobalt has been used by our group extensively with very reliable results some years ago (not shown here). If chromium can not be used due to any fabrication issues or restrictions, this is an alternative worth considering.

3.3.3 Chromium Removal – Argon Mill

As mentioned earlier, the chromium etch mask reacts with the SF_6 during the ICP-RIE etch, rendering it very resilient against chemical removal. Clean Cr has an etch rate of 60 nm s^{-1} in Chromium Etchant.[n] After the ICP-RIE, this rate drops by a factor of 2000 to 0.03 nm s^{-1}. This process would not only be time consuming but would also dissolve the Cr below the gold electrodes (i.e. the adhesive layer), which is hardly affected by the SF_6. To circumvent this problem a followup ICP-RIE argon mill is used to remove the affected Cr layer. Afterward, the original etch rate is restored. It is still important to leave the sample as short as possible (40 s) in the Chromium Etchant to avoid the removal of the electrodes.

3.4 KOH Wet Etch

As an alternative to the ICP-RIE to undercut the SiC samples, potassium hydroxide (KOH) can be used as it etches Si but does barely react with SiC. Chemically, the etching works as follows:[109–111]

$$\mathrm{Si} + 2\ \mathrm{OH^-} + 2\ \mathrm{H_2O} \rightarrow\ \mathrm{SiO_2(OH)_2^{2-}} + 2\ \mathrm{H_2}.$$

The aggravating part here is the formation of hydrogen gas (H_2) at the sample surface. Small hydrogen gas bubbles can stick to the surface, preventing the KOH from reaching the Si underneath. Therefore, they act as random micromasks that stop the etching process locally.[112] In order to remove these bubbles upon creation, a magnetic stirrer is added to the KOH solution. Through this constant movement, they detach from the sample surface and thus interfere less with the etching process. Furthermore, the etching process is very sensitive to temperature. As expected, a higher temperature leads to a higher etch rate. The concentration,

[n] For the sake of completeness, it should be mentioned that 25 nm Al dissolve in 7 min, leading to an etch rate of 0.06 nm s^{-1}. We have not analyzed if the etch rate of Al is affected by the ICP.

on the other, hand has a much weaker influence.[110,113,114] Hence, a thermometer is used to precisely monitor the temperature to ensure consistent etch rates. The magnetic stirrer guarantees a uniform heat distribution within the KOH solution. The crystal direction plays also an important role for the etch rate. Most importantly, in the $[111]$ direction nearly no etching is observed compared to the other crystal directions.[110] According to Seidel et al.[110] the etch rate ratio $[110] : [100] : [111]$ is $160 : 100 : 1$ at room temperature and $50 : 30 : 1$ at 100 °C. Therefore, our vertical etching depth ($[111]$) is still primarily determined by the ICP-RIE.

To undercut a string without adjacent electrodes, we use 10 g KOH pellets dissolved in 100 mL at a temperature of 40 °C for 15 min. If the sample features adjacent electrodes, the etch rate is decreased due to the narrow gap between the electrodes and resonators. In this case, we recommend increasing the temperature to 50 °C and reducing the time to 10 min. However, as we can fully undercut our string resonators with the ICP-RIE, the KOH etching step is obsolete, especially as the ICP-RIE delivers more consistent results.

4 Characterization of String Resonators

In this chapter we establish the experimental framework used in all the experiments of this work. In particular, this chapter introduces the measurement setups at room and low temperature and describes the three different measurement methods employed in this work.

4.1 Experimental Setups

In order to detect the vibrations of our nanomechanical string resonators we rely on an optical detection scheme, namely, a Fabry-Pérot interferometer. This measurement scheme is implemented in two different setups, one at room temperature (RT) and one at low temperatures (LT). For the sake of simplicity, the first setup is explained with a piezo and the second one with a dielectric drive. However, the electronic wiring and thus the drive mechanism are interchangeable.

4.1.1 Room Temperature Setup

A schematic visualization of the setup for RT measurements with piezo actuation is shown in Fig. 4.1. The light from a 1550 nm fiber based laser[a] is collimated and centered into a free space beam. The light is then guided through a half-wave ($\lambda/2$ in Fig. 4.1) and quarter-wave plate ($\lambda/4$) which allow for the control of the polarization state of the light beam. The polarized light passes a PBS; depending on the polarization direction the amount of reflection and transmission is determined, allowing for a precise reduction of the laser power. The polarization state of the light is then transformed into circular polarization by another quarter-wave

[a] NKT Photonics Koheras Basic E15

plate. An objective[b] focuses the light on the string resonator, where the light is reflected. Because our laser spot exceeds the width of our string resonator, the light is also reflected from the substrate and interferes with the light coming from the resonator, imprinting the movement of the resonator on the light. The quarter-wave plate converts the circular to a linear polarization. Due to a phase shift of π that occurred during the reflection, the light is reflected at the PBS and focused onto photo detector. The signal is then send to the vector network analyzer (VNA). For imaging, a LED and a camera are added to the setup with the help of two 92:8 beam splitters. The LED illuminates the sample which is then pictured by the camera. This allows for a precise positioning of the individual string resonators with respect to the laser spot. An Attocube three axis positioning system is used to move the sample in the vacuum chamber. The vacuum is kept below 1×10^{-4} mbar to exclude gas damping. The sample holder, which is thoroughly described in Sec. 4.1.3, hosts the sample and the piezo. The piezo is driven by a radio frequency (rf) signal emitted by the VNA.

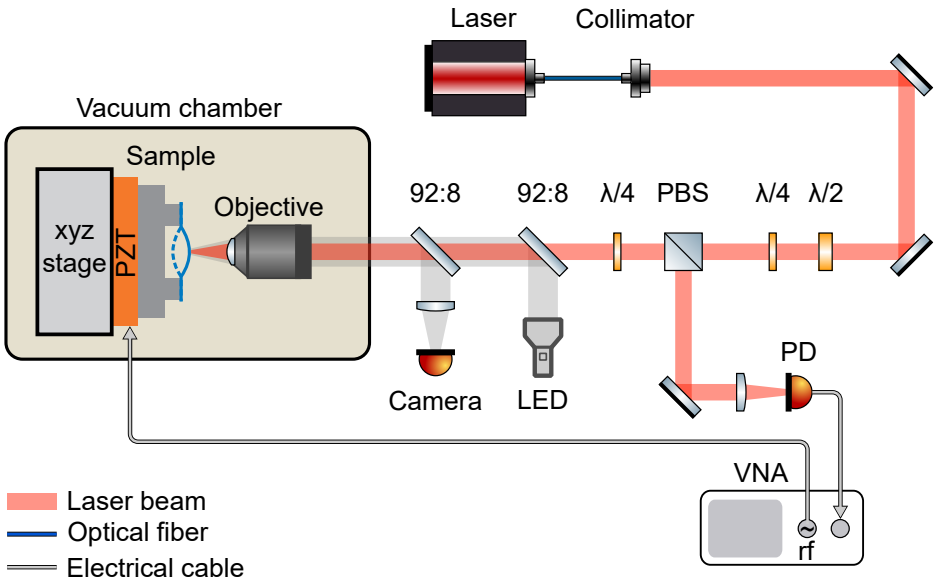

Figure 4.1: Visualization of the measurement setup with piezo actuation at room temperature that is used to detect the vibrations from nanomechanical string resonators. PBS - polarizing beam, PD - photo detector, PZT - piezo, VNA - vector network analyzer. Adapted from Ref. [34].

4.1.2 Low Temperature Setup

The working principle of the optical detection in the LT setup is identical to the one presented in Sec. 4.1.1, although the setup is arranged slightly differently. The free space PBS, and the quarter- and half-wave plates are replaced by a fiber based circulator as visualized in Fig. 4.2. Both the VNA and the spectrum analyzer are connected to the electrical output of the photo detector. This is required for ring-down measurements, which are explained in Sec. 4.4 and App. C. For the dielectric drive, the VNA's rf signal and a direct current (dc) signal are combined with the help of a bias tee. It is then guided via the sample holder (see Sec. 4.1.3 for details) and bond wires to the electrodes. The underlying drive mechanism is explained in Sec. 2.4.

The optical dry cryostat[c] is cooled with a helium compressor that is connected to the cold head, which is the coldest place in the cryostat. The cold head and all the parts that are directly connected to it, such as the stage and the screws, are fabricated from titanium. A three axis positioning system (stage) is used to position the string

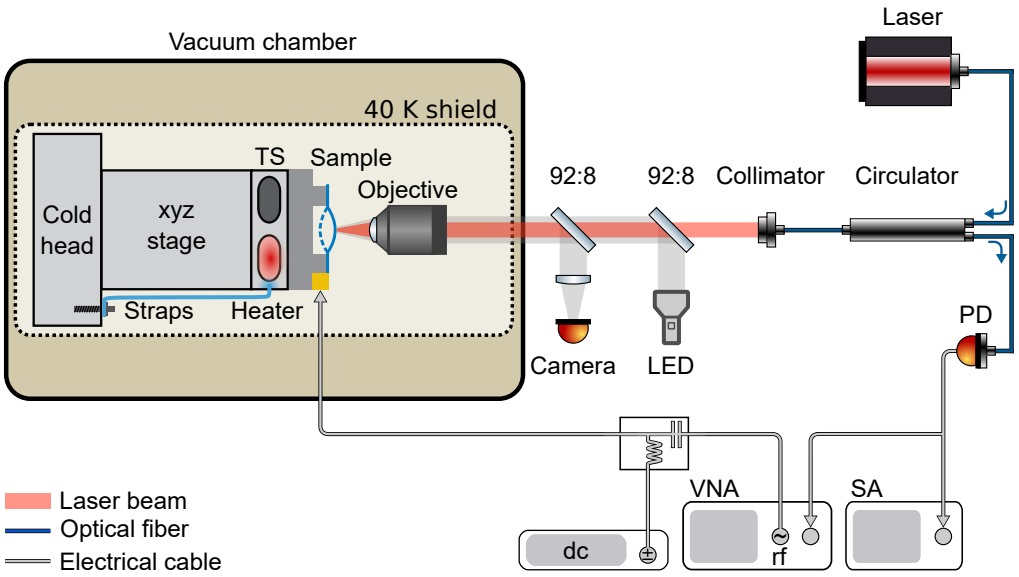

Figure 4.2: Visualization of the measurement setup with a dielectric drive at low temperatures that is used to detect the vibrations from nanomechanical string resonators. Additionally, we are able to perform ring-down measurements with this electronic setup. The yellow square on the sample indicates a bond pad. SA - spectrum analyzer, PD - photo detector, TS - temperature sensor, VNA - vector network analyzer. Adapted from Ref. [34].

[b] Mitutoyo Plan Apo NIR 100X, numerical aperture 0.5
[c] Attocube attoDRY800

resonators with respect to the laser. On top of the stage, a temperature sensor (TS) and a resistive heater allow for a precise control of the sample's temperature. In order to improve the thermalization of the sample, thermal straps are directly connecting the cold head to the plate below the sample holder, containing the temperature sensor and the heater as indicated in Fig. 4.2. Note that the objective[d] is also directly mounted on the cold head and therefore cooled to low temperatures. The cold head and the components attached to it are completely encapsulated by a 40 K shield made out of aluminum. It is essential that the shield is sealed as good as possible, because even small holes lead to a significant increase in temperature. The whole setup is mounted on an air damped table to prevent vibrations of the compressor to interfere with the measurement.

4.1.3 Sample Holder

Each of our sample holders serves two prime purposes: First, it safely connects the sample to the positioning and cooling systems and, secondly, gives us electrical access to the sample. All sample holders are based on a metal (mostly aluminum) plate with four screw holes that are used to attach them to the positioners from Attocube (see Fig. 4.3 (a-c)). To establish a piezo drive, a piezo element is glued to the metal plate with a thin layer of indium.[e] A droplet of old photoresist or conductive silver (low temperature measurements) attaches the sample onto the piezo. Figure 4.3 (d) shows a detailed sketch of the used materials. For electrical access, a two pin header is glued with epoxy to the base plate. One of the pins is soldered to the plate (ground) and the other one on top of the piezo as shown in Fig. 4.3 (a,b).
For samples with electrodes, a special gold coated printed circuit board (PCB) comes into play as depicted in Fig. 4.3 (d,e). Indium is used to glue the board to the metal plate. By that the gold plated areas with holes in them are electrically connected to the sample holder and therefore to ground. Bond wires link the string's electrodes to two different ports of the PCB, which in turn lead to pin heads. No matter the driving technique, the pin heads are electrically connected to our measurement devices.

In the course of this work, several improvements have been implemented to increase the quality of the sample holders especially in terms of thermalization. The very first generation of sample holders, which is shown in Fig. 4.3 (a), is based on a 2.5 mm thick metal plate cut with a big cutter from bulk material. Due to this procedure, the whole base plate is slightly bent (see Fig. 4.3 (a)), reducing the thermal contact to the underlying cold plate of the cryostat significantly. To

[d] attoMICROSCOPY LT-LWDO/0.55 CFM I 50X, numerical aperture 0.55
[e] Research Kit from Indium Corporation of America

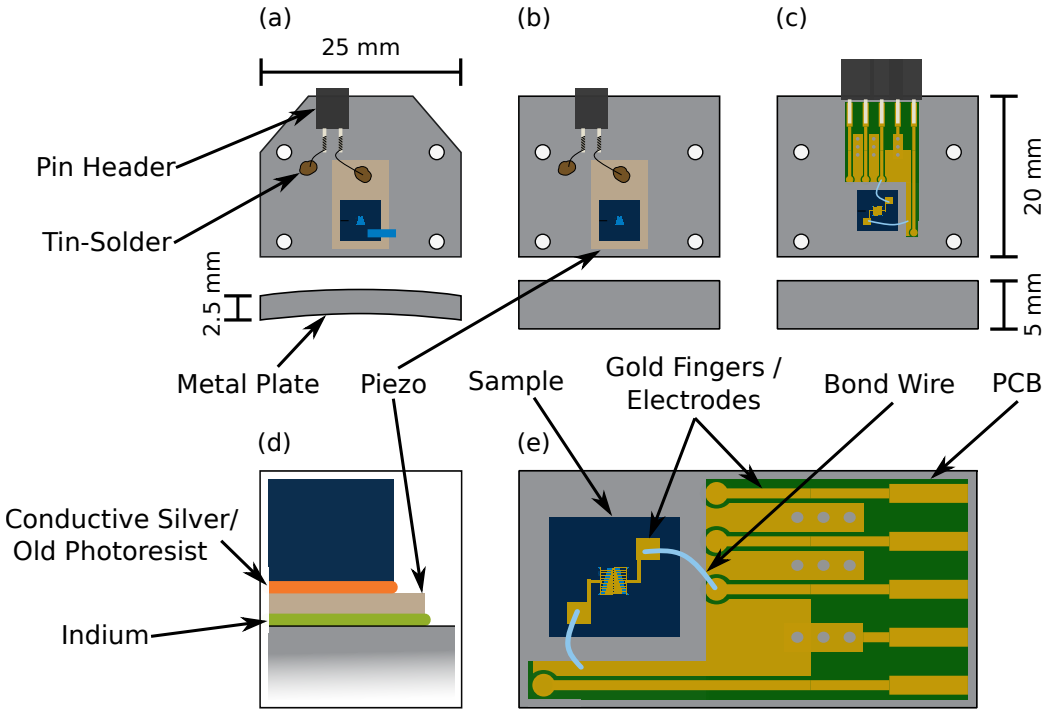

Figure 4.3: Top and side view of the first (a) and second generation (b,c) of sample holders. For samples with electrodes, where we want to utilize the dielectric drive, a special electric board is used as shown in (c). In (e) a close-up of the board and its connections to the sample is shown. The cross section, at the position marked by the blue line in (a), is visualized in (d).

overcome this issue, thicker plates are cut and smoothed with the help of a lathe as shown in Fig. 4.3 (b,c).
To further improve the thermal contact, the old photoresist, which glues the sample to the holder, is replaced by conductive silver. Additionally, photoresist gets brittle at low temperature, which can result in the sample detaching from the sample holder.
Lastly, the piezo and the indium layer are removed for samples that can be driven dielectrically. This should again enhance the thermalization because ceramics have a bad thermal conductivity. Hence, the sample is directly glued to the metal base plate as shown in Fig. 4.3 (c).

4.1.4 Is a Good Laser Worth It?

A bad laser with a lot of phase noise leads to a scattering over time of the measured quality factor of an InGaP string resonator.[f] This is shown in Fig. 4.4, where we display the quality factor measured over time, first with a noisy laser (*Agilent 81940A Tunable Laser*, Laser 1) and second with a low noise laser (NKT Photonics Koheras Basic E15, Laser 2). Clearly, the scattering of the quality factor is reduced significantly by using a low noise laser. While the mean value is hardly affected, the standard deviation drops by a factor of 5 from 7.8×10^4 to 1.5×10^4. Therefore, nearly all measurements within this work are recorded with Laser 2.

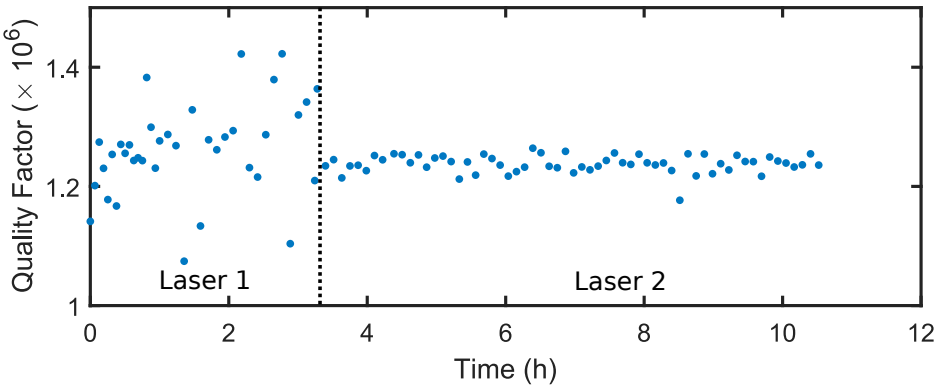

Figure 4.4: Quality factor as a function of time, measured with Agilent 81940A Tunable Laser (Laser 1) and NKT Photonics Koheras Basic E15 (Laser 2). The Quality factor is measured via a ring-down (see Sec. 4.4). The data was recorded on sample C at 33 K.

4.2 VNA Measurement

One way to determine the resonance frequency and quality factor of a resonator is to perform a frequency sweep with a vector network analyzer (VNA). By fitting a Lorentzian function to the data, we are able to extract the frequency and quality factor as shown in Fig. 4.5 for three different strings. As expected from Euler-Bernoulli beam theory, shorter strings offer higher frequencies (compare Fig. 4.5 (a-c)). In order to gain reliable results of the quality factor, it is mandatory to choose an adequate bandwidth and a power for which the resonator remains in the linear regime. The data shown in Fig. 4.5 (a), for instance, is recorded with a power of −110 dBm and a bandwidth of 1 Hz, leading to a measurement time of around 30 min. Fluctuations and drifts during this time can influence the data. Ring-downs

[f] This sample was fabricated by my colleague Maximilian Bückle.

are a faster and more reliable method in these cases, shown in Sec. 4.4 and App. C. For strings with slightly lower quality factors, however, VNA measurement are a feasible option as visible in Fig. 4.5 (b,c).

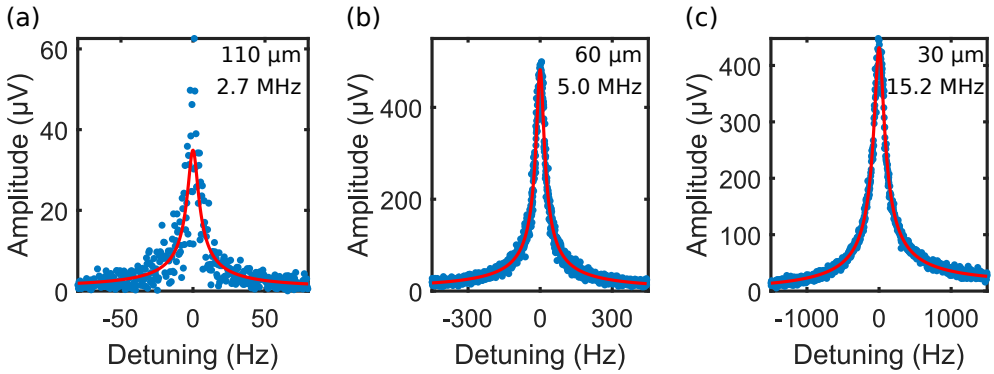

Figure 4.5: Amplitude as a function of frequency for three different string resonators recorded with a VNA. Blue points and red lines corresponds to measured data and a Lorentzian fit, respectively. The length, resonance frequency and quality factor are: (a) 110 µm, 2.7 MHz, 360 000; (b) 60 µm, 5.0 MHz, 160 000; (c) 30 µm, 15.2 MHz, 80 000. The data was recorded on sample A at room temperature.

4.3 Calibration with Thermal Motion

Even in the absence of an active drive a thermal force is actuating our resonator, resulting in the so called thermal or Brownian motion. Conveniently, it can be utilized to translate the measured voltage signal into an actual amplitude in meters. Here we follow the procedure presented by Hauer et al.[42] For that we introduce the one-sided displacement power spectral density $S_{zz}(\omega)$ (units $m^2\,Hz^{-1}$), which is the density of power as a function of frequency. By integrating $S_{zz}(\omega)$ over all frequencies, we can directly recover the mean-square amplitude $\langle z^2 \rangle$ of the resonator:[42,115]

$$\langle z^2 \rangle = \frac{1}{2\pi} \int_0^\infty S_{zz}(\omega)\, d\omega. \tag{4.1}$$

The SA, however, delivers a voltage power spectral density $S_{vv}(\omega) = \frac{U(\omega)^2}{B}$ (units $V^2\,Hz^{-1}$), where U is the measured voltage and B the SA's bandwidth, from which we can not directly retrieve the amplitude. Generally, the power spectral density of

the driving force $S_{\mathrm{FF}}(\omega)$ and $S_{\mathrm{zz}}(\omega)$ are related via

$$\begin{aligned} S_{\mathrm{zz}}(\omega) &= |\chi(\omega)|^2 \, S_{\mathrm{FF}}(\omega), \\ &= \frac{1}{m^2 \left(\left(\omega_0^2 - \omega^2\right)^2 + \left(\omega\Gamma\right)^2 \right)} \cdot S_{\mathrm{FF}}(\omega), \end{aligned} \tag{4.2}$$

where χ is the mechanical susceptibility. If the resonator is only driven by thermal noise, $S_{\mathrm{FF}}(\omega)$ can be replaced by a frequency independent force $S_{\mathrm{FF}}^{\mathrm{th}}$. The corresponding mean-square amplitude is (see App. I)

$$\langle z^2 \rangle = \frac{S_{\mathrm{FF}}^{\mathrm{th}}}{4\Gamma\omega_0^2 m^2}, \tag{4.3}$$

with the effective mass m.[g] Additionally, the equipartition theorem can be used to determine $\langle z^2 \rangle$ due to the thermal excitation:[42,116,117]

$$\frac{1}{2} m \omega_0^2 \langle z^2 \rangle = \frac{1}{2} k_{\mathrm{B}} T, \tag{4.4}$$

where k_{B} is the Boltzmann constant and T the temperature.[h] Combining Eq. (4.3) and (4.4) yields

$$S_{\mathrm{FF}}^{\mathrm{th}} = 4\Gamma k_{\mathrm{B}} T m. \tag{4.5}$$

By inserting this into Eq. (4.2), we get

$$S_{\mathrm{zz}}(\omega) = \frac{4\Gamma k_{\mathrm{B}} T}{m \left(\left(\omega_0^2 - \omega^2\right)^2 + \left(\omega\Gamma\right)^2 \right)}, \tag{4.6}$$

which is the theoretical amplitude power spectral density of our thermally driven resonator. Next we connect the theoretical $S_{\mathrm{zz}}(\omega)$ and measured $S_{\mathrm{vv}}(\omega)$ power spectral density with a conversion factor α (units m V^{-1}):

$$S_{\mathrm{vv}}(\omega) = S_{\mathrm{vv}}^{\mathrm{nf}} + \frac{1}{\alpha^2} S_{\mathrm{zz}}(\omega), \tag{4.7}$$

where $S_{\mathrm{vv}}^{\mathrm{nf}}$ is the noise floor. If we know α, we can transform our measured voltage to actual amplitudes.

[g] Note that this approximation is only valid if $2\omega_0 > \Gamma$, which holds true for our high Q resonators.

[h] In the literature this equation is often given as $\frac{1}{2} k \langle z^2 \rangle = \frac{1}{2} k_{\mathrm{B}} T$, where k is the effective spring constant. Since $\omega_0^2 = \frac{k}{m}$, it is identical to Eq. (4.4).

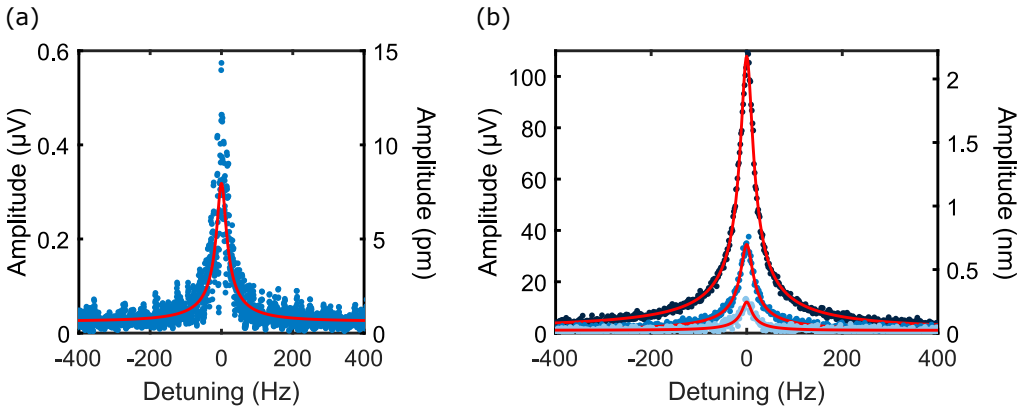

Figure 4.6: Amplitude as a function of detuning for a thermal (a) and external (b) drive. Colored dots correspond to measured data and red lines to fits to the data. Fitting Eq. (4.7) to the data shown in (a) yields a conversion factor $\alpha = 20\,\mu\text{m}\,\text{V}^{-1}$. In (b) the drive powers are −55 dBm (dark blue), −65 dBm (blue), and −75 dBm (light blue). Note that the setup, sample, and laser spot on the sample remained completely unchanged between the measurements (a) and (b) to guarantee a constant conversion factor α. The data was recorded on a 110 µm string of sample B at room temperature.

In Fig. 4.6 (a) you can see the thermal motion of sample B at room temperature. By fitting Eq. (4.7) to the data, we are able to extract the conversion factor $\alpha = 20\,\mu\text{m}\,\text{V}^{-1}$, allowing us to determine the amplitude in meters. As shown on the right axis of Fig. 4.6 (a), the thermal motion of this 110 µm string is 8 pm, which just below the 11.7 pm measured for a similar string in Ref. [118]. Note that the quality factor of sample B ($Q \approx 100\,000$) is considerable smaller than the one presented in Ref. [118] ($Q \approx 400\,000$). Driving the sample with an external drive increases the amplitude significantly as shown in Fig. 4.6 (b). For a drive power of −55 dBm, we can for instance reach an amplitude of more than 2 nm. The conversion factor α depends massively on the setup, the sample, and, unfortunately, the current position of the laser spot on the string resonator. As it is impractical to recalibrate after every move of the sample, we normally present the amplitude in units of volt. The conversion factor α and the noise floor $S_{\text{vv}}^{\text{nf}} = 9.5 \times 10^{-16}\,\text{V}^2\,\text{Hz}^{-\frac{1}{2}}$ yield a sensitivity of[42]

$$\eta = \sqrt{S_{\text{vv}}^{\text{nf}}\,\alpha^2} = 0.6\,\text{pm}\,\text{Hz}^{-\frac{1}{2}}, \tag{4.8}$$

which is very close to the 2 pm $\mathrm{Hz}^{-\frac{1}{2}}$ presented by my colleague Jana Ochs[i] for a similar setup.[119]

4.4 Ring-Down Measurement

Ring-down measurements are a fast and reliable option to determine the quality factor of high Q resonators. The measurement principle is explained in App. C. Figure 4.7 shows two ring-down measurements, recorded on sample A and B. The data is fitted with Eq. (2.8), yielding decay times of 0.015 s and 0.007 s. The quality factor can then be calculated with

$$Q = 2\pi f_0 \tau, \tag{4.9}$$

where f_0 is the resonance frequency. For the aforementioned decay times, we get quality factors of 250 000 and 95 000, respectively. Determining even higher quality factors, as shown in Chap. 8, is also feasible via ring-downs. On the other hand, for very small quality factors and/or very high frequencies, the decay times are very small. At this point, it gets very challenging to capture and evaluate ring-downs. VNA measurements are, therefore, the better option for these circumstances as they appear e.g. for very high harmonics (see Chap. 5, 6, and 7).

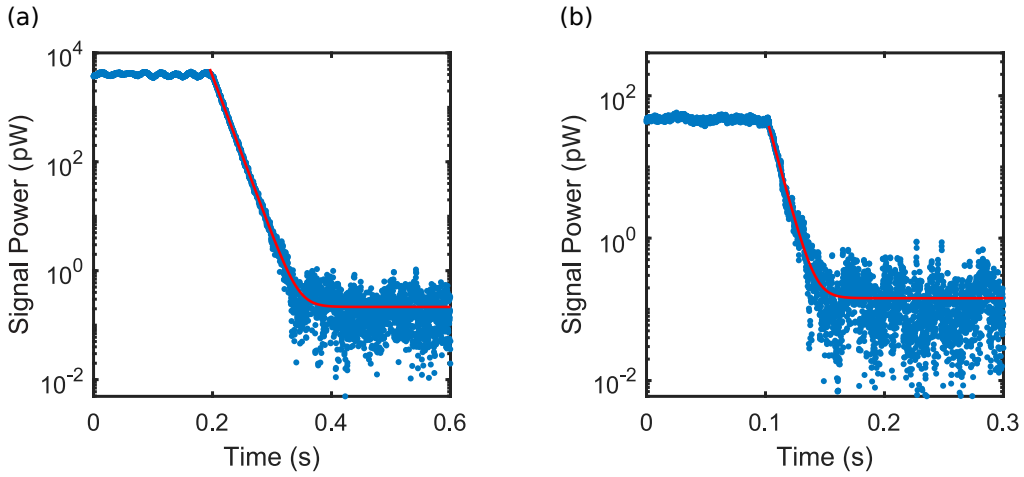

Figure 4.7: Ring-down measurement of sample A (a) and B (b). The extracted quality factors are 250 000 and 95 000, respectively. The red line is an exponential decay (Eq. (2.8)) fitted to the data (blue dots).

[i]Here we are referring to the data presented in Appendix C.2,[119] which is recorded on a SiC sample driven dielectrically and measured optically. Our sample B, on the other hand, is actuated by a piezo. A noise floor of $S_{\mathrm{vv}}^{\mathrm{nf}} = 5.9 \times 10^{-11}\,\mathrm{V^2\,Hz^{-\frac{1}{2}}}$ and a conversion factor of $\alpha = 0.3\,\mu\mathrm{m\,V^{-1}}$ are given in the text.

4.5 Comparing Quality Factors

In the previous sections, we introduced three different measurement techniques to determine the quality factor of a string resonator. Here, we compare them for different scenarios with the results summarized in Tab. 4.1.
As mentioned before, the VNA sweep, the SA thermal motion (if the signal to noise is sufficient) and ring-down measurements can be used to determine the quality factor of resonators with Qs below 100 000.
In the case of a high Q resonator, where the quality factor of the fundamental mode is in the range of 300 000 to 500 000, the ring-down is the best method. Depending on the fluctuations and drifts of the resonance frequency, the VNA measurement may also be a valid option. The recording of the thermal motion, on the other hand, is much faster but does not, at least for most of our measurement, deliver the desired precision. This can for instance be seen in the first line of Tab. 4.1 and is consistent within a multitude of our measurements.
For even higher quality factors, which are reached in essentially all our low temperature measurements, the ring-down is the only available option. Both the VNA sweep and the thermal motion erratically over- or underestimate the quality factor, depending on the fluctuations. Note, however, that both VNA as well as the SA

Table 4.1: Comparison of the extracted quality factor for the aforementioned methods: VNA frequency sweep (Sec. 4.2), SA thermal motion (see Sec. 4.3), and ring-down (see Secs. 4.4 and App. C). Italic values are not very trustworthy. The VNA measurement of Sample A and F as well as all thermal motions were recorded with a bandwidth of 1 Hz. RT and LT correspond to room and low temperatures. Note that Sample A suffered from some non reversible degradation over time (more than a year), i.e. different measurements can not be directly compared. However, all quality factors shown in a single line in this table have been measured within very short time intervals and are therefore comparable. Note that we only included data measured on the fundamental mode of various 110 µm SiC string resonators.

Sample	VNA ($\times 10^3$)	Therm. Motion ($\times 10^3$)	Ring-Down ($\times 10^3$)
Sample A (RT)	363	*270*	356
Sample A (LT)	–	*2900*	2500
Sample A (LT)	–	*2200*	3600
Sample B (RT)	98	96	95
Sample F (LT)	*700*	–	800

are able to reliably extract the frequency at low temperatures. Further, we want to point out again that both the frequency and the quality factor for higher harmonics (i.e. high frequency and low quality factor) can only be extracted with the help of VNA sweeps.

5

Determining Young's Modulus

The following chapter is based on our manuscript:

Y. S. Klaß, M. Bückle, J. Doster, R. Braive, and E. M. Weig, *"Determining Young's modulus via the eigenmode spectrum of a nanomechanical string resonator"*, submitted manuscript (2022). Ref. [32]

The samples were fabricated by M. Bückle (InGaP, material provided by R. Braive) and me (SiC and SiN). The measurements were performed by M. Bückle (InGaP and SiN) and me (SiC). Some preliminary measurements were performed by J. Doster. Data analysis was done by E. M. Weig and me. The manuscript was written by E. M. Weig and me. Therefore, the following chapter contains many original passages. This includes the chapter's introduction, Sec. 5.2 with all subsections, but excludes Sec. 5.1, which is not part of the manuscript. Figures are reproduced from Ref. [32].

Young's modulus of a material determines its stiffness under uniaxial loading. It is a crucial material parameter for many applications involving mechanical or acoustic degrees of freedom, including nano- and micromechanical systems,[135] cavity optomechanics,[136] surface or bulk acoustic waves, including quantum acoustics,[137,138] nanophononics,[139] or solid-state-based spin mechanics.[140] The precise knowledge of Young's modulus is necessary for quantitative prediction or characterization of those devices' performance. However, the value of Young's modulus of most materials has been known to strongly depend on growth and even nanofabrication conditions such that relying on literature values may lead to significant deviations.[98–100,141] This is apparent from Fig. 5.1 where we show exam-

ples of experimentally and theoretically determined values of Young's modulus along with common literature values for three different materials. For instance, for amorphous stoichiometric Si_3N_4 grown by low pressure chemical vapor deposition experimental values between 160 GPa[46] and 370 GPa[125] have been reported. The situation is considerably more complex for crystalline materials, for which additional parameters such as the crystal direction or the specific crystal structure affect the elastic properties. For these materials, Young's modulus can, in principle, be calculated via the elastic constants of the crystal[101]. However, its determination may be impeded by the lack of literature values of the elastic constants of crystal structure under investigation because the database for theoretical values is scarce for some materials. This is seen for the ternary semiconductor alloy $In_{1-x}Ga_xP$, where even the gallium content x influences Young's modulus.[101] For 3C-SiC theoretical predictions vary between 125 GPa[130] and 466 GPa[134] because the literature provides differing values of the elastic constants, even surpassing the spread of experimentally determined values. This is demonstrated in detail in Sec. 5.1.

While Young's modulus of macroscopic bulk or thin film samples is conveniently characterized using ultrasonic methods[120,142] or static techniques such

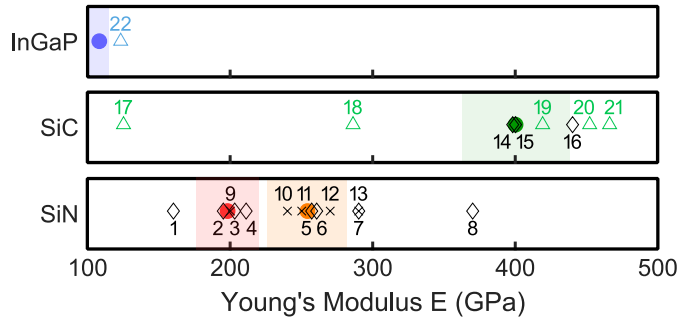

Figure 5.1: Young's modulus for $In_{0.415}Ga_{0.585}P$, 3C-SiC, and LPCVD Si_3N_4. Our measured values and uncertainties are shown as filled colored circles and colored shades, respectively, whereas literature values are represented as open symbols. Colored open triangles correspond to values computed form literature values of the elastic constants, matching the crystal direction of the investigated resonators. Measured and other literature values are shown as open black diamonds and crosses, respectively. For the sake of visibility we omit all stated uncertainties. Values are taken from: 1[46], 2[120], 3[121], 4[24], 5[122], 6[123], 7[124], 8[125], 9[126], 10[52], 11[26, 127],12[128],13[129], 14[95], 15[96] , 16[100], 17[130], 18[131], 19[132], 20[133], 21[134], 22[101]. Labels for measured values are found below the corresponding symbol, while all other labels are situated above. Adapted from Ref. [32].

as nanoindentation[96], load deflection[121,125] or bulge testing[95,122,124], determining its value on a nanostructure is far from trivial. For freely suspended nanobeams and cantilevers, a dynamical characterization via the eigenfrequency provides reliable results.[24,98,99,123,143] However, this method is severely limited for nanomechanical devices such as membranes or strings subject to a strong intrinsic tensile prestress where the contribution of the bending rigidity and thus Young's modulus to the eigenfrequency becomes negligible.[a] In Sec. 5.2, which is based on our manuscript,[32] we present a method to determine Young's modulus of a string resonator that is susceptible to the stress and orientation of the material.

5.1 Calculating Young's Modulus

As long as we are within the linear regime (Hooke's law), stress σ and strain ϵ are related via[144]

$$\sigma = C\epsilon, \tag{5.1}$$

$$\epsilon = S\sigma, \tag{5.2}$$

where C and S are the compliance and stiffness tensor, respectively.[145–147] In case of an isotropic material like SiN this simplifies to the well known form $\sigma = E\epsilon$. For an anisotropic material (e.g. SiC, InGaP), C and S have to be fourth grade tensors ($3^4 = 81$ entries per tensor) to fully capture the problem. Utilizing 3C-SiC's cubic symmetry enables us to reduce these to 6×6 matrices with only 3 independent entries, yielding[144]

$$\begin{pmatrix} \sigma_1 \\ \sigma_2 \\ \sigma_3 \\ \sigma_4 \\ \sigma_5 \\ \sigma_6 \end{pmatrix} = \begin{pmatrix} c_{11} & c_{12} & c_{12} & 0 & 0 & 0 \\ c_{12} & c_{11} & c_{12} & 0 & 0 & 0 \\ c_{12} & c_{12} & c_{11} & 0 & 0 & 0 \\ 0 & 0 & 0 & c_{44} & 0 & 0 \\ 0 & 0 & 0 & 0 & c_{44} & 0 \\ 0 & 0 & 0 & 0 & 0 & c_{44} \end{pmatrix} \begin{pmatrix} \epsilon_1 \\ \epsilon_2 \\ \epsilon_3 \\ \epsilon_4 \\ \epsilon_5 \\ \epsilon_6 \end{pmatrix} \tag{5.3}$$

for Eq. (5.1), where c_{ij} are the elastic constants of the respective material. Here, we used Voigt notation, thus σ_1, σ_2, and σ_3 correspond to the normal stress in the crystal direction $[100]$ (x-axis), $[010]$ (y-axis), and $[001]$ (z-axis), respectively. On the other hand, σ_4, σ_5, and σ_6 represent different shear stress components. Young's modulus of the $[100]$ direction (x-axis) can be calculated by inverting the very first entry of the stiffness matrix s_{11}, i.e.

[a] The fit does in fact converge to a similar value as we find with our new method. This, however, is only true if we use all available eigenmodes. Reducing the number of modes leads to a significant deviation from the expected value. While the Matlab fitting command *fitnlm*, which is normally used by our group, does not work correctly, the command *nlinfit* is able to fit the data. Note that the resulting stress is complex and one has to take the real part.

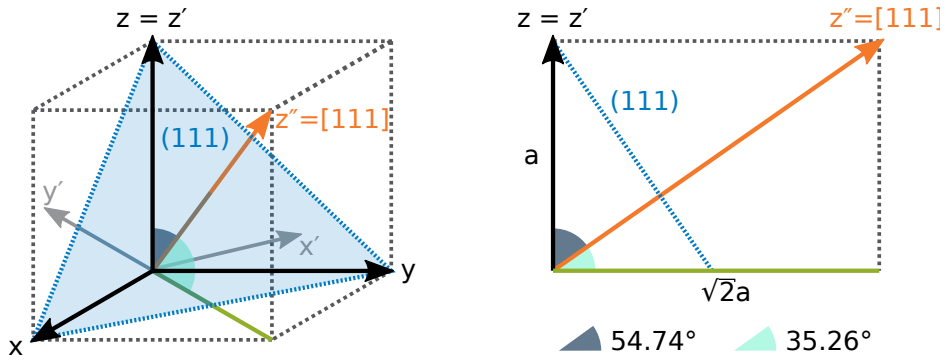

Figure 5.2: Visualization of the required axis rotations to calculate Young's modulus. On the right side we assume a length of a for the cube, leading to a diagonal length of $\sqrt{2}a$.

$$E_{[100]} = (s_{11})^{-1}\,. \tag{5.4}$$

In order to calculate Young's modulus in an arbitrary direction we have to rotate the matrix in a way that the rotated x-axis aligns with the desired direction. Note that the exact mathematical expressions for these operations can be found in Refs. [34, 147]. In order to calculate Young's modulus for the (111)-plane, we first have to rotate our matrix by $\frac{3\pi}{4}$ about the original z-axis, which aligns the new x′-axis[b] with the $[-110]$ direction. Next, we perform a rotation by $\arctan\left(\sqrt{2}\right) \approx 54.74°$ (see Fig. 5.2) about the x′-axis, tilting the z′-axis (identical to the original z-axis) in the $[111]$ direction. Note that both the x″-axis (identical to the x′-axis) and the y″-axis are located in the (111)-plane.[c] Therefore, if we now rotate our matrix by an angle θ about the z″-axis, we can utilize Eq. (5.4) to extract Young's modulus in this direction. As the resulting equation $E(\theta)$ is very lengthy, it is omitted at this point. By inserting the three elastic constants c_{11}, c_{12}, and c_{44} of SiC we can finally determine Young's modulus for every direction on our (111)-wafer. However, a wide range of different elastic constants can be found in literature, leading to Young's moduli of 125 GPa,[130] 286 GPa,[131] 419 GPa,[132] 452 GPa,[133], 466 GPa,[134] or 517 GPa[148] in the $[\bar{1}\bar{1}2]$ direction, which corresponds to the orientation of our SiC string resonators. As we will show in Sec. 5.2, the elastic constants

[b]Here we use the following notation: For every rotation applied to the system, we add one *prime* to the axis' names, i.e. x′, and x″-axis are rotated once, and twice, respectively.

[c]If the plane (hkl) contains the direction $[uvw]$ (or is parallel to it), the relation $hu+kv+lw = 0$ holds. For example, the direction $[\bar{1}\bar{1}2]$, which corresponds to the orientation of our SiC resonators, is within the (111)-plane, because $-1-1+2=0$.

$$
\begin{aligned}
c_{11} &= 352\,\text{GPa}, \\
c_{12} &= 140\,\text{GPa}, \\
c_{44} &= 233\,\text{GPa},
\end{aligned}
\tag{5.5}
$$

from Ref. [132] fit the best to our measured Young's modulus of 400 GPa. These values result in Young's modulus $E(\theta)$ shown in Fig. 5.3. Clearly, Young's modulus is almost perfectly isotropic with a value of approximately 419 GPa. Note that all analyzed elastic constants (Refs. [130–134, 148]) suggest a very high isotropy of Young's modulus in the (111)-plane. In other planes, however, this does not hold true.

5.2 Determining Young's Modulus via the Eigenmode Spectrum

5.2.1 Theoretical Considerations

According to the Euler-Bernoulli beam theory the out-of-plane flexural eigenfrequencies of a doubly clamped string subjected to tensile stress with simply supported boundary conditions is given by Eq. (2.2). Slightly rewriting this equa-

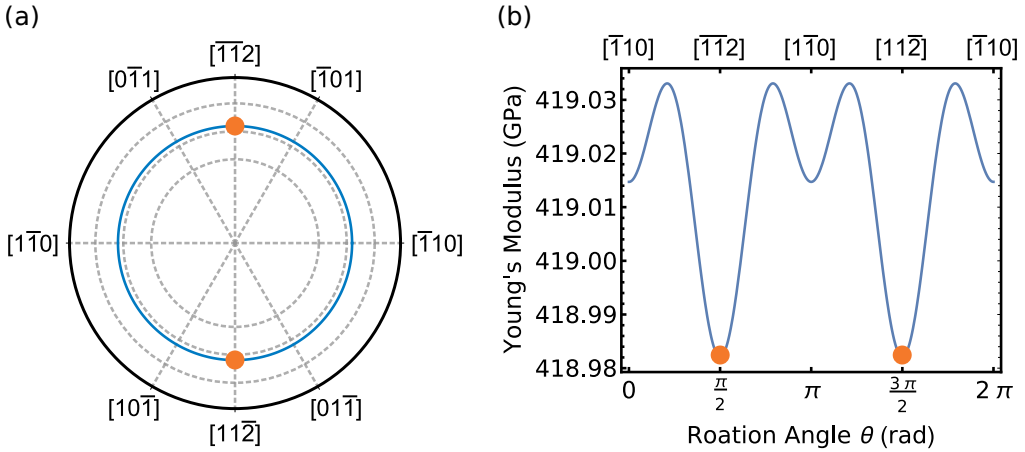

Figure 5.3: Dependence of Young's modulus on the crystal direction in the (111)-plane with the elastic constants from Ref. [132] (see Eq. (5.5)). The results are shown in polar (a) and cartesian coordinates (b). The dashed circular lines in (a) correspond to values of 300 GPa, 400 GPa, and 500 GPa, respectively (from inside to outside). Orange dots indicate the crystal directions that are parallel to our SiC string resonators.

tion gives us

$$f_n = \frac{n^2\pi}{2L^2}\sqrt{\frac{Eh^2}{12\rho} + \frac{\sigma L^2}{n^2\pi^2\rho}}, \tag{5.6}$$

where n is the mode number, L the length and h the thickness of the resonator, ρ the density, E Young's modulus and σ the tensile stress. For the case of strongly stressed nanostrings, the bending contribution to the eigenfrequency, i.e. the first term under the square root, has only a minor contribution compared to the significantly larger stress term. Hence, the eigenfrequency-vs.-mode number diagram will approximate the linear behavior of a vibrating string, $f_n \approx (n/2L)\sqrt{\sigma/\rho}$. So, even for, a large number of measured harmonic eigenmodes, only minute deviations from linear behavior imply that Young's modulus can only be extracted with large uncertainty. However, computing f_n^2/n^2 for two different mode numbers and subtracting them from each other allows it to cancel the stress term from the equation, yielding

$$\frac{f_n^2}{n^2} - \frac{f_m^2}{m^2} = E\frac{\pi^2 h^2(n^2 - m^2)}{48L^4\rho}, \tag{5.7}$$

with $m \neq n$. This equation can be solved for Young's modulus

$$E = \frac{48L^4\rho}{\pi^2 h^2(n^2 - m^2)} \cdot \left(\frac{f_n^2}{n^2} - \frac{f_m^2}{m^2}\right), \tag{5.8}$$

which allows us to determine Young's modulus from just the basic dimensions of the string resonator, the density, and the measured eigenfrequency of two different modes.

5.2.2 Propagation of Uncertainty

In order to get a better understanding of the contributions to the individual uncertainty of the measured Young's modulus, we calculate the propagation of uncertainty. To this end, we assume an uncertainty for the eigenfrequency δf, length δL, thickness δh, and density $\delta\rho$, leading to:

$$\begin{aligned}\delta E = \frac{48L^4\rho}{\pi^2 h^2}\Bigg(&\left|\frac{2f_n}{n^2(n^2-m^2)}\right| \cdot \delta f_n + \left|\frac{2f_m}{m^2(n^2-m^2)}\right| \cdot \delta f_m \\ &+ \left|\frac{f_n^2}{n^2(n^2-m^2)} - \frac{f_m^2}{m^2(n^2-m^2)}\right| \left[\frac{4}{L}\delta L + \frac{2}{h}\delta h + \frac{1}{\rho}\delta\rho\right]\Bigg).\end{aligned} \tag{5.9}$$

This enables us to determine the complete error δE for each combination of n and m by inserting the measured frequencies $f_{n,m}$. In order to interpolate between the integer values of n and m, we insert the eigenfrequencies of the Euler-Bernoulli

beam theory (see Eqs. (5.6) and (2.2)) in Eq. (5.9) and obtain the simplified expression

$$\delta E = \frac{48L^4\rho}{\pi^2 h^2}\left(\left|\frac{2f_n}{n^2(n^2-m^2)}\right|\cdot\delta f_n + \left|\frac{2f_m}{m^2(n^2-m^2)}\right|\cdot\delta f_m\right) + \frac{4E}{L}\delta L + \frac{2E}{h}\delta h + \frac{E}{\rho}\delta\rho. \tag{5.10}$$

Interestingly, only the contribution of the eigenfrequency uncertainty depends on the mode numbers n and m (and hence their difference Δ), whereas the contributions of the other three uncertainties are constant. The four summands of Eqs. (5.9) (color points) and (5.10) (solid lines) are plotted individually in Fig. 5.4 as a function of the mode number n for a 110 µm SiC string and the uncertainties shown in Tab. 5.1. The second mode number m is fixed exemplary to $m = 1$ and 20. For small n and for $n \approx m$, the eigenfrequency uncertainty provides the dominant contribution to δE. For all other values of n, δE is dominated by the constant uncertainties of the resonator thickness, the density, and the length, whereas the contribution of the eigenfrequency uncertainty becomes negligible. Therefore, a precise determination of Young's modulus calls for a large number of measured harmonic eigenmodes, leading to large $\Delta = |m-n|$ and, hence, smaller uncertainties. Note that all three constant contributions are proportional to Young's modulus, resulting in a similar relative uncertainty of approximately 10 % as shown in Tab. 5.2.

5.2.3 Measuring the Eigenmode Spectrum

To validate the proposed method, we are analyzing samples fabricated from four different wafers on the three material platforms outlined already in Fig. 5.1. First,

Table 5.1: Parameters used for the calculations, including the measured length of the strings, the density, and the uncertainty of the frequency. Adapted from Ref. [32].

	SiN-FS	SiN-Si	SiC	InGaP
h (nm)	100(2)	100(2)	110(2)	100(1)
L string 1 (µm)	107.7(5)	100.4(5)	109.9(5)	110.5(5)
L string 2 (µm)	88.0(5)	90.3(5)	99.9(5)	90.5(5)
L string 3 (µm)	78.2(5)	70.2(5)	89.8(5)	80.5(5)
ρ (g/cm^3)	3.1(1)[149–151]	3.1(1)[149–151]	3.2(1)[78,152]	4.4(1)[153]
δf (‰)	0.25	0.25	0.25	0.25

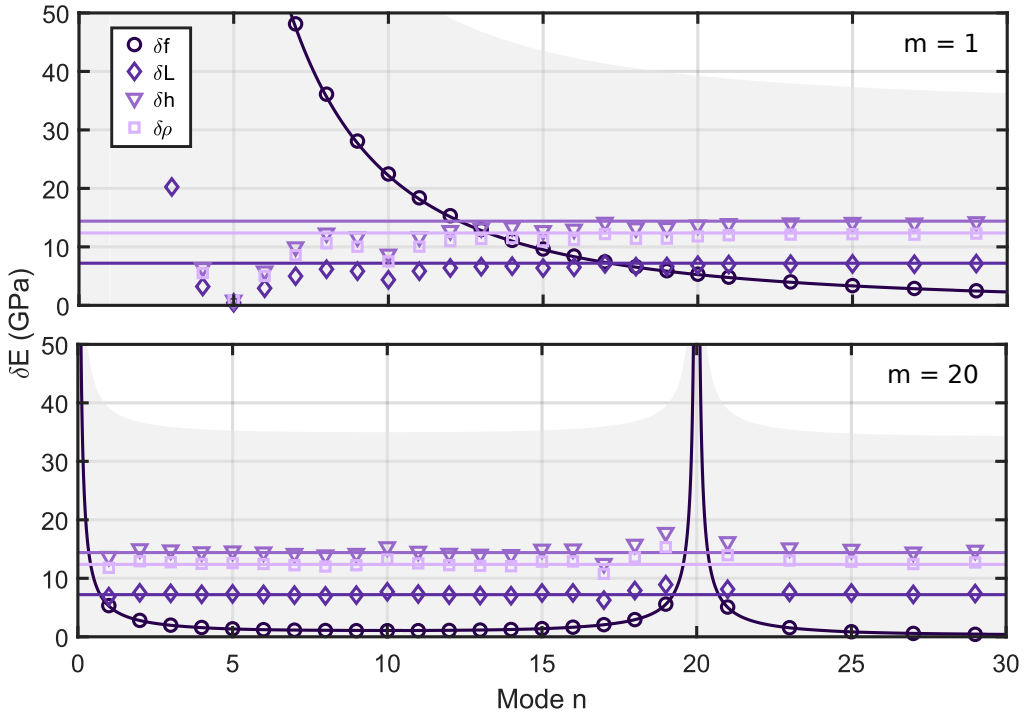

Figure 5.4: Contributions of the individual uncertainties of the 110 µm SiC string for two fixed mode numbers $m = 1$ (top) and $m = 20$ (bottom). The colored symbols are calculated with Eq. (5.9) and the measured frequencies $f_{n,m}$. The colored solid lines are computed with Eq. (5.10) where we used the values of $f_{\mathrm{n,m}}$ predicted by Euler–Bernoulli beam theory. The data was recorded on a 110 nm string of sample A. Adapted from Ref. [32].

we use wafer W1, which consists of 110 nm 3C-SiC on a Si substrate (denoted as SiC). Two wafers consist of 100 nm LPCVD-grown amorphous stoichiometric Si_3N_4 on a fused silica substrate (denoted as SiN-FS) and on a sacrificial layer of SiO_2 atop a silicon substrate (SiN-Si), respectively. The fourth wafer comprises a 100 nm thick $In_{0.415}Ga_{0.585}P$ film epitaxially grown atop a sacrificial layer of $Al_{0.85}Ga_{0.15}As$ on a GaAs wafer (denoted as InGaP). All four resonator materials exhibit a substantial amount of intrinsic tensile prestress. Details regarding the wafers are listed in App. A.

On all these wafers we fabricate a harp of nanostrings, which we introduced in Sec. 3.2.1. As a reminder, the length of the resonator on such a harp range from 10 µm to 110 µm in steps of 10 µm. Since the length has a significant impact on the stress of the string resonator (see Chap. 6 and Ref. [39]) and the stress might have an impact of Young's modulus,[154] we focus solely on the three longest strings of each sample for which the tensile stress converges to a constant value.[39] The

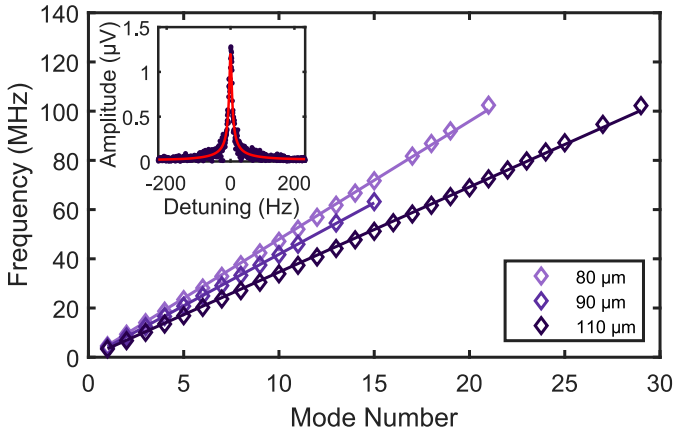

Figure 5.5: Measured eigenfrequency as a function of the mode number for the three longest SiN-FS strings including fits of the string model (solid lines). Inset depicts the frequency response of the fundamental mode ($n = 1$, $L = 110\,\mu\text{m}$, $f_1 = 3.37\,\text{MHz}$), including a Lorentzian fit (solid lines) to the data (dots). The data was recorded on a 110 nm string of sample D. Adapted from Ref. [32].

frequency response of a series of higher harmonics is measured via VNA sweeps in combination with the RT setup and piezo actuation (see Sec. 4.1.1 and 4.2). Figure 6.1 depicts the results for the three longest SiN-FS strings, exhibiting up to 29 eigenmodes. In order to demonstrate the nearly linear behavior, the data is fitted with the string model (see Eq. 2.3) with σ being the only free parameter. The slight deviation observed for high mode numbers is a consequence of the bending contribution neglected in this approximation. Note the fit of the full model (Eq. (5.6), not shown here), which we utilize in Chap. 6, yields a somewhat better agreement, however, Young's modulus can not be reliably extracted as a second free parameter in the stress-dominated regime.

5.3 Determining Young's Modulus

Combining the measured eigenmode spectrum with Eqs. (5.8) and (5.9) allows us to finally determine Young's modulus along with its uncertainty. All input parameters as well as their uncertainties are listed in Tab. 5.1. To get as much statistics as possible, we introduce the difference of two mode numbers $\Delta = |m - n|$ as a parameter. For instance, $\Delta = 5$ corresponds to the combinations $(n = 1, m = 6)$, $(2, 7)$, $(3, 8)$, ... For each Δ we calculate the mean value of $\overline{E}$ and $\overline{\delta E}$, respectively. The obtained values of Young's modulus are depicted as a function of Δ for all four materials in Fig. 5.6. Note that only Δ values comprising two or more combinations

Table 5.2: Young's modulus including the total uncertainty determined for the four different materials. Adapted from Ref. [32].

	SiN-FS	SiN-Si	SiC	InGaP
E (GPa)	254(28)	198(22)	400(38)	108(7)

of mode numbers are shown. The individual combinations $E(\Delta)$ contributing to $\overline{E}$ for a specific Δ are visualized as gray dots, whereas the mean values of Young's modulus $\overline{E}$ for each value of Δ are included as colored circles. Clearly, Young's modulus of each material converges to a specific value for increasing Δ. These values are extracted by averaging over the obtained values of $\overline{E}$ and summarized in Tab. 5.2. Note that only the upper half of the available Δ points are included in the averaging process to avoid some systematic distortions appearing for low Δ. The uncertainty associated with the mean Young's modulus $\overline{\delta E}$ is indicated by gray shades. As discussed in detail in Sec. 5.2.2, the Δ-dependence of the uncertainty arises solely from the uncertainty in the eigenfrequency determination. Therefore, this contribution to the total uncertainty is highlighted separately as colored error bars. For small Δ, a large uncertainty in the eigenfrequency determination is observed which dominates the complete uncertainty $\overline{\delta E}$. It coincides with a considerable scatter of the individual combinations, which is also attributed to the impact of the eigenfrequency determination. As expected, for increasing Δ, the uncertainty in the eigenfrequency determination decreases, such that the complete uncertainty $\overline{\delta E}$ becomes dominated by the constant contribution originating from the uncertainties in the density, thickness and length of the string. The total uncertainty is obtained by averaging $\overline{\delta E}$ over the upper half of the available Δ points. It is also included in Tab. 5.2.

5.3.1 Discussion

Our determined values of Young's modulus are included in the literature overview shown in Fig. 5.1 as colored dots. Clearly, the determined values coincide with the parameter corridor suggested by our analysis of the existing literature: For InGaP, where no independent literature values are available we rely on the value presented by my colleagues M. Bückle et al. in Ref. [101]. Similar to Sec. 5.1, they utilized the elastic constants of InGaP with the appropriate Ga content ($x = 0.585$) and crystal orientation ([110]) to calculate Young's modulus, yielding $E^{\text{th}}_{\text{InGaP}} = 123\,\text{GPa}$,[101,153], which is rather close to our experimentally determined value of $E_{\text{InGaP}} = 108(7)\,\text{GPa}$. For SiC we measure a Young's modulus of $E_{\text{SiC}} = 400(36)\,\text{GPa}$ which is in perfect agreement with the experimentally determined literature values of 398 GPa[95] and 400 GPa[96] by Iacopi et al.. It is also in good

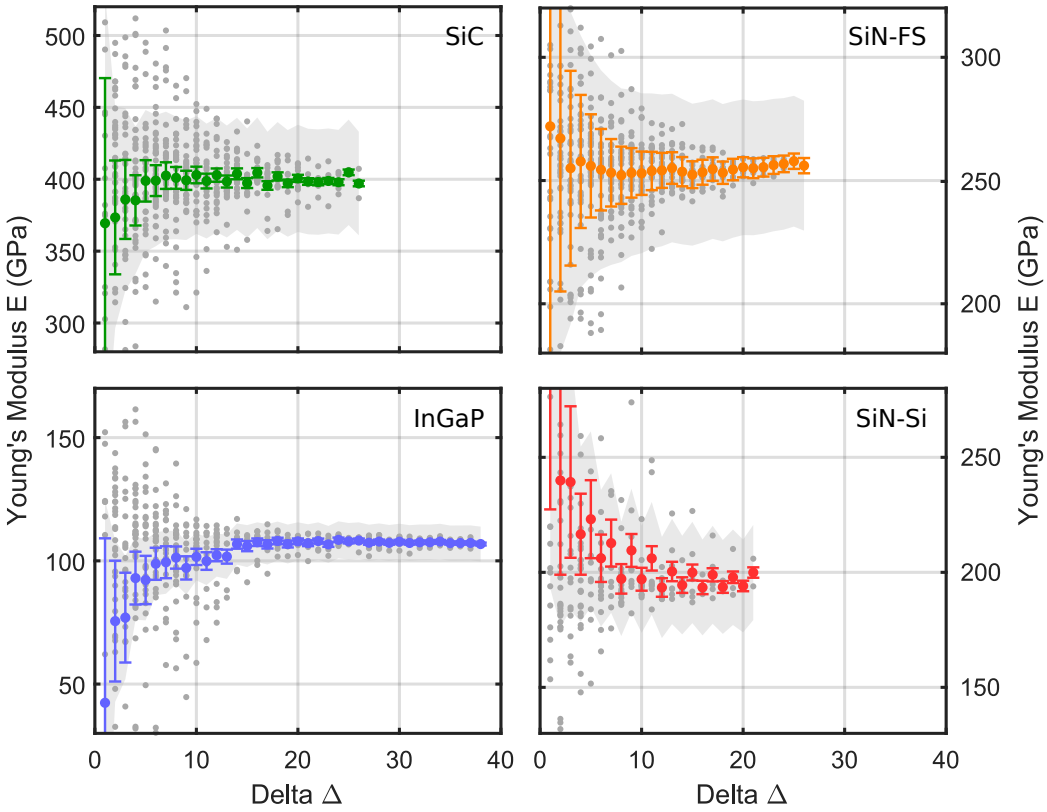

Figure 5.6: Determined Young's modulus as a function of Δ for the four different materials SiC (green), SiN-FS (orange), SiN-Si (red), and InGaP (blue). Gray dots correspond to individual combinations of $|m - n|$. Their mean values $\overline{E}(\Delta)$ are shown as colored dots. While all combinations of n, m are included in the calculation of $\overline{E}$ for a given Δ, not all of them are shown as gray dots as some heavy outliers appearing mostly for low values of Δ have been truncated for the sake of visibility. The complete uncertainty is represented by the gray shade, whereas its Δ-dependent contribution arising from the uncertainty in the eigenfrequency determination is represented by the colored error bars. The data was recorded on sample A, C, D, and E. Adapted from Ref. [32].

agreement with the elastic constants published by Li and Bradt,[132] yielding 419 GPa for the orientation of our string resonators. Interestingly, SiN-FS and SiN-Si exhibit significantly different Young's moduli of $E_{\text{SiN-FS}} = 254(26)$ GPa and $E_{\text{SiN-Si}} = 198(21)$ GPa, respectively. In Fig. 5.1 we can see two small clusters of measured Young's moduli around our determined values, suggesting that the exact Young's modulus depends on growth conditions and the subjacent substrate material even for the case of an amorphous resonator material.

5.4 Conclusion

In this chapter, we investigate a new method to determine Young's modulus via the eigenmode spectrum of nanomechanical string resonators. It is susceptible to the stress and orientation of the resonator's material. We extract Young's modulus for four different materials, including a well-defined uncertainty. A comparison with literature reveals not only very small deviations but also a growth dependence of Young's modulus.

6

Universal Length Dependence of Tensile Stress

The following chapter is based on our publication:

M. Bückle†, Y. S. Klaß†, F. B. Nägele, R. Braive, and E. M. Weig, *"Universal length dependence of tensile stress in nanomechanical string resonators"*, Physical Review Applied 15, 034063 (2021). Copyright (2022) by the American Physical Society. Ref. [39].

The samples were fabricated by M. Bückle (InGaP, material provided by R. Braive) and me (SiC and SiN). The measurements were performed by M. Bückle (InGaP and SiN) and me (SiC). Some preliminary measurements were performed by F. B. Nägele. The theoretical model and data analysis was joint work from M. Bückle and me. The manuscript was written by E. M. Weig, M. Bückle and me. Therefore, the following chapter contains many original passages.
Figures are reproduced from Ref. [39].

† These authors contributed equally to this work.

The one-dimensional tensile stress in the string resonators is not solely determined by elastic material properties, but significantly depends, as we show in this chapter, on its length and other geometric parameters. This allows one to increase the tensile stress by approximately 50 % by using shorter strings and thus boost the dissipation dilution. As discussed in Chap. 2.3, a higher tensile stress directly translates into higher quality factors. Since the same behavior is observed for four different wafers (the same as in Chap. 5) featuring the three complementary

device layers SiC (Wafer A), SiN, and InGaP, the observed length dependence of the tensile stress seems to be material independent. We explain the model we developed that captures the observed features. It describes the geometric reconstruction of the string resonator by a combination of two effects that determine the stress distribution in the device layer: The vertical release of the string leads to a deformation of the clamping structure, while the subsequent lateral release undercuts the clamping pads. This is explained in depth in Sec. 6.2.

6.1 Extracting the Tensile Stress

As a first step we have to determine the tensile stress of individual string resonators. Similar to Chap. 5, we utilize for that the data of the frequency f_n as a function of the mode number n. This time, however, all available lengths are considered. The data is fitted with the solution of the Euler–Bernoulli beam theory (in Chap. 5 we used only the string model) for a doubly clamped string with simply supported boundary conditions (Eq. 2.3) as shown in Fig. 6.1. As the tensile stress σ is the only free fitting parameter, we can directly extract it from the fit algorithm. For the Young's modulus we used the parameter determined in Chap. 5. The obtained stress values are shown as a function of the resonator length for all four materials

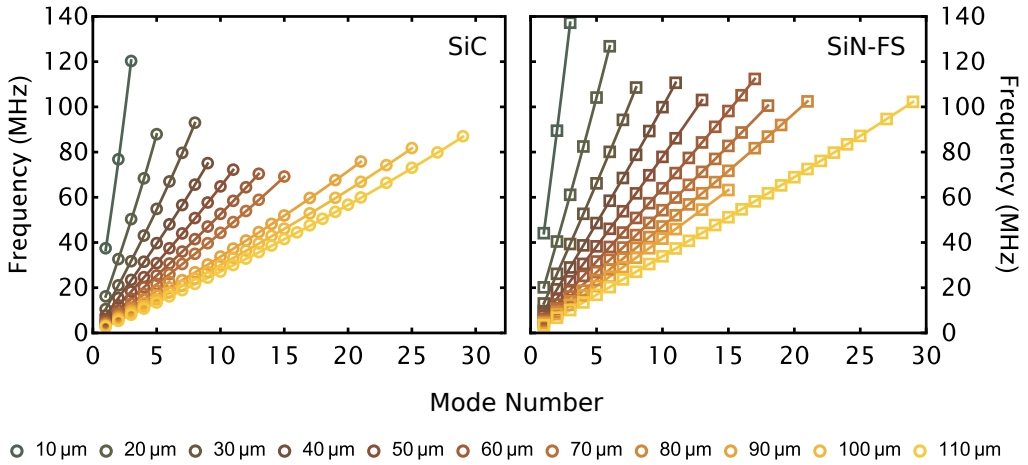

Figure 6.1: Eigenfrequencies of the out-of-plane modes as a function of the mode number for SiC (left) and SiN-FS (right) string resonators. The resonator lengths range from 10 µm to 110 µm for both materials. Fits of the eigenfrequencies using the full Euler-Bernoulli model (Eq. (2.2)) are included as solid lines. The data was recorded on sample A and D. The right plot is adapted from Ref. [39].

in Fig. 6.2.[a] Clearly, the tensile stress is not constant, but decreases for increasing resonator length. The same qualitative behavior is observed in all four material systems.

6.2 Elastic Model

To describe this behavior, we have developed a model that is based on elastic theory. As such, it is material independent and can be applied to all materials under investigation. The model assumes a prismatic string of length L, width w and thickness h_1. Its cross-sectional area is $A_\mathrm{s} = w\,h_1$. On both ends, the string is attached to a rectangular clamping structure. It consists of a clamping pad in the device layer with lithographic dimensions $2a_x$ and $2a_y$, as well as thickness h_1 (Fig. 6.3 (a)), which is supported by a pedestal of height h_0 in the underlying

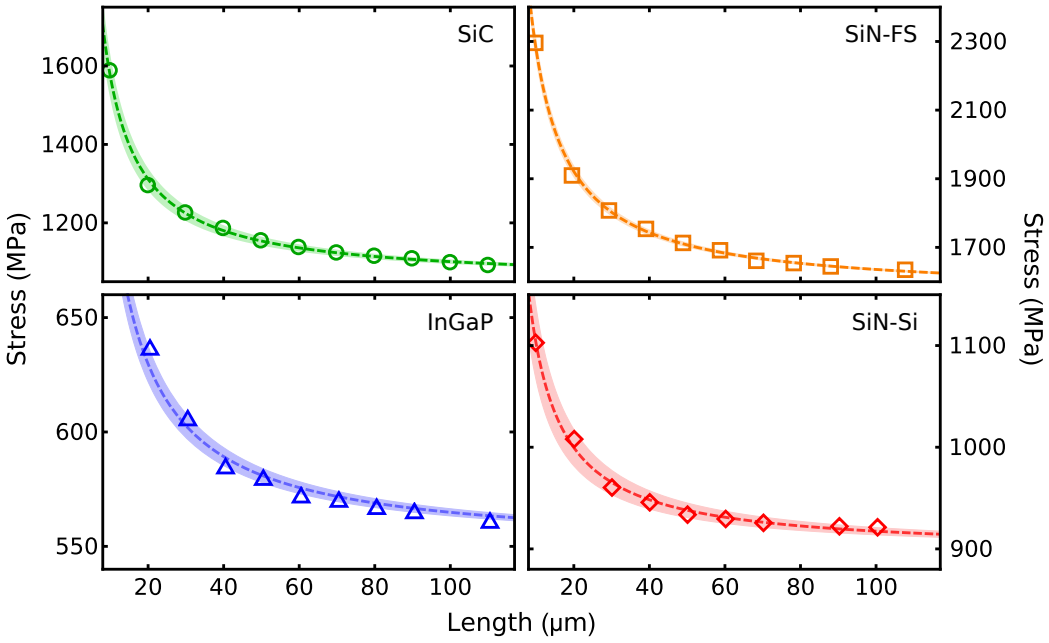

Figure 6.2: Experimentally determined tensile stress as a function of the length of the nanostring for all four material systems. Fits of Eq. (6.9) are included as solid lines. The obtained fit parameters are summarized in Tab. 6.2. The shaded areas indicate the uncertainty resulting from measurement errors of the pedestal height h_0 and undercut a_uc. The data was recorded on sample A, C, D, and E. Adapted from Ref. [39]

[a] As a reminder: In contrast to our publication [39], we use here the previously determined Young's moduli from Chap. 5. At the time of publication, we relied on literature values. Consequently, values and figures are marginally different to the ones presented in our publication.

sacrificial or substrate layer (Fig. 6.3 (b,c)). As a result of the isotropic wet (InGaP, SiN) or dry (SiC) etching process required to release the nanostrings, the clamping pads exhibit a certain undercut a_{uc}, i.e. the width of the pad $2a_x$ is larger than that of the remaining pedestal $2a_{\mathrm{p}} = 2a_x - 2a_{\mathrm{uc}}$. The cross-sectional area of the clamping pad (in yz-plane) is $A_{\mathrm{p}} = 2a_y\, h_1$. The geometric parameters of the four investigated samples are summarized in Tab. 6.1. To achieve accurate results it is crucial to know the exact dimensions of the individual structures.[b] A sketch of the relevant dimensions is shown in Fig. 6.3. The thickness of the device layers h_1 are taken from the growth protocol of the manufacturers. For SiC we confirmed

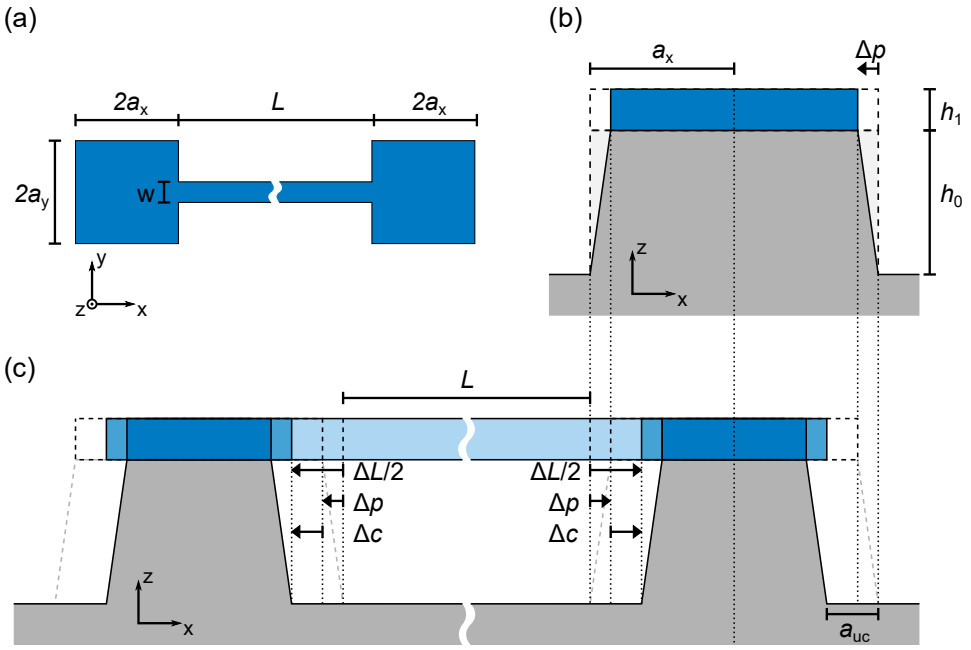

Figure 6.3: Sample geometry and parameters of the model. (a) Lithographic dimensions of the nanostring and its clamping pads. (b) Cross section through the clamping structure illustrating the shearing contraction of the pedestal following the vertical release of the structure. (c) Cross section through the clamping structure illustrating the lateral contraction of the undercut areas of the clamping pad following the horizontal release. Combining the vertical and horizontal releases leads to the string's length change of ΔL. Areas supported by a pedestal are colored in dark blue, undercut areas of the clamping pads are indicated by a lighter color and the string is marked with the lightest blue. Dotted lines serve as guides to the eye. Adapted from Ref. [39].

[b] As a reminder in Chap. 5, we only needed the exact length and thickness of the string resonator.

Table 6.1: Geometric parameters of the investigated samples. Adapted from Ref. [39].

	h_1 (nm)	h_0 (nm)	$2a_x$ (µm)	$2a_y$ (µm)	a_{uc} (nm)	w (nm)
SiN-FS	100(2)	460(20)	13.7(2)	13.6(2)	570(100)	420(25)
SiN-Si	100(2)	365(20)	14.1(2)	15.0(2)	410(150)	340(25)
SiC	110(2)	570(40)	14.2(2)	15.0(2)	860(150)	360(30)
InGaP	100(1)	990(10)	12.7(2)	13.3(2)	640(170)	250(15)

the thickness by means of ellipsometry.[c] The pedestal height h_0 is determined with the help of an atomic force microscope.[d] All the remaining dimensions are extracted via SEM imaging as demonstrated in Fig. 6.4. While the length and width of both the string and pedestal are straight forward to extract (see Fig. 6.4 (b-d)), the undercut a_{uc} is a more challenging task. For InGaP, SiC and SiN-FS, there is a clear contrast change between supported and unsupported areas of the clamping pad, which is sufficient to measure the undercut, as can be seen in Fig. 6.4 (c,e). However, SiN-Si does not have a clear contrast change as shown in Fig. 6.4 (b). To overcome this challenge, parts of the pedestal are removed with a focus ion beam (FIB), exposing the undercut (see in Fig. 6.4 (f)) and allows for a precise measurement of the undercut. As already mentioned in previous chapters, all material parameters are listed in App. A.

As we show in the following, the tensile stress in the device layer atop an unstressed sacrificial layer or substrate gives rise to a balance of forces that in turn leads to a length- and geometry-dependent change in the one-dimensional tensile stress of the nanostring. To quantify the contributing forces, we roughly follow the process sequence required to fabricate a freely suspended nanostring (see Sec. 3.2.1). First, we consider the vertical release of the nanostructure. It comprises all vertical etching contributions, notably the ICP-RIE dry etch and the isotropic chemical wet etch (only InGaP and SiN). Consequently, we neglect horizontal contributions from the ICP-RIE and chemical wet etch at this point. The vertical release penetrates both the device layer and the sacrificial (InGaP and SiN-Si) or substrate layer (SiC and SiN-FS) and defines the height of the pedestal h_0. Following this vertical release, the tensile-stressed device layer will slightly contract and induce a certain amount of shear in the pedestal (Fig. 6.3 (b)). As a result, the tensile stress in the pad relaxes to a value σ_{p}.
Second, the lateral release is considered. It accounts for the lateral etching during

[c] The measurement and analysis was performed by Gillian Kiliani at the University of Konstanz.
[d] This measurement was peformed by Ralf Messmer.

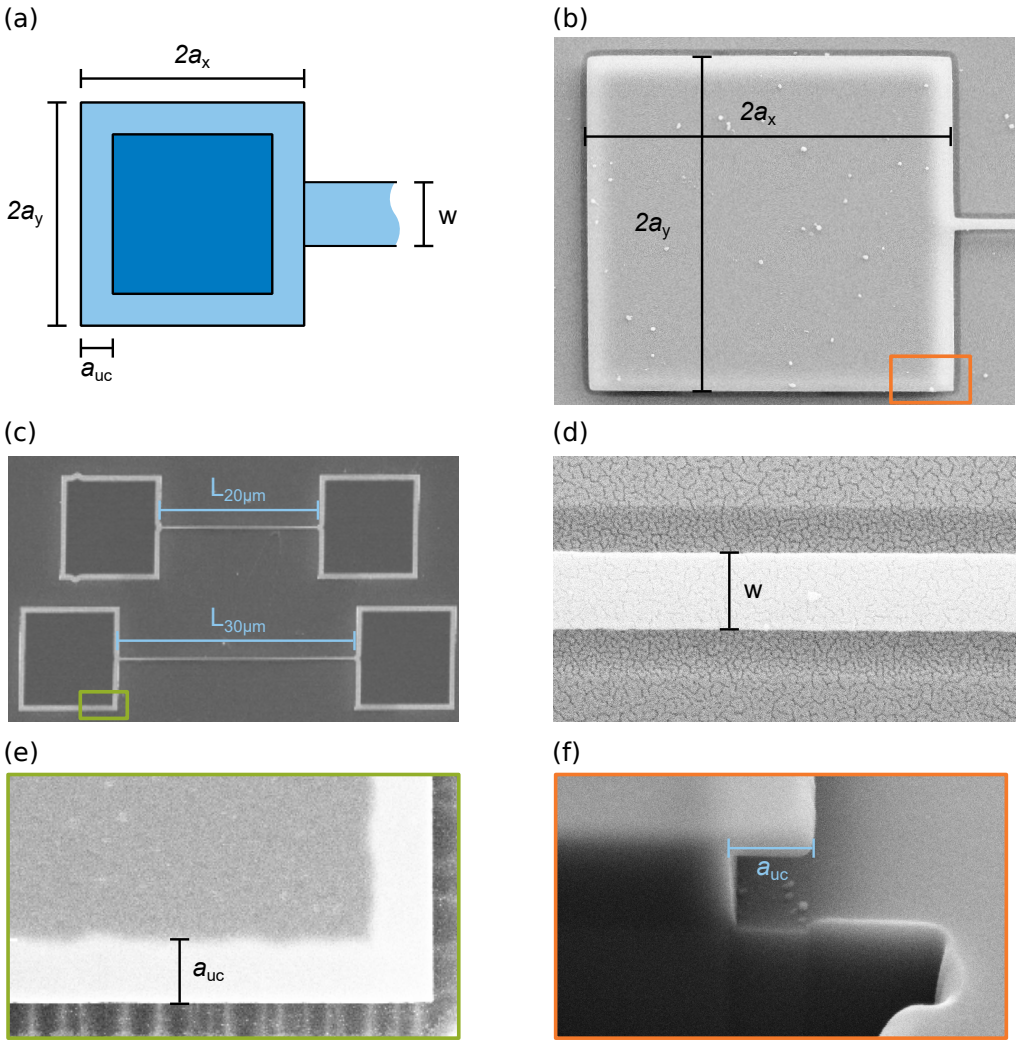

Figure 6.4: Extraction of the required dimensions. (a) Schematic sketch of the clamping structure including the undercut and the pedestal. Dark and light blue correspond to supported and undercut areas, respectively. (b) SEM image of a SiN-Si clamping structure to determine the pedestal widths. (c) SEM image of an InGaP sample that is used to extract the length of the strings. (d) Close-up SEM image of a SiN-Si string resonator to determine the width of the string. (e) Close-up of a InGaP clamping pad. The clear contrast change between supported and unsupported areas can be used to determine the undercut. It corresponds to the location indicated by the green square in (c). (f) Angled SEM image of the SiN-Si clamping pad. A FIB was used ot expose the undercut by removing material at the edge of the clamping structure. It corresponds to the location indicated by the orange square in (b).

the nanostring release. As a result of this lateral release, the two-dimensional stress in the nanostring relaxes in the direction perpendicular to the string (y direction). At the same time, the now undercut parts of the tensile-stressed clamping pad contract because they are no longer strained by the underlying material. Therefore, additional stress is applied on the nanostring (Fig. 6.3 (c)). The combination of the described effects gives rise to the tensile stress experienced by the nanostring σ. The model assumes a clear separation between the vertical and lateral release, which are described in the following two sections, respectively, and neglects geometric and elastic reconfigurations of the sheared pedestal and stressed clamping pad arising from the lateral releases, which we can safely assume to be small.

Pedestal Shear from Vertical Release

To evaluate the shear of the pedestal induced by the vertical release of the structure, we first consider an isolated clamping structure and focus on its cross section along the x-z direction as indicated in Fig. 6.3 (b). The resonator will be included at a later stage. Following the vertical release of the structure, the strong tensile stress in the device layer leads to a contraction of the clamping pad in order to minimize internal forces. This contraction leads to a shear of the pedestal (see Fig. 6.3 (b)). The reconfiguration of the clamping structure stops once equilibrium between the reduced tensile force and the counteracting shearing force is reached. The shear stress τ of such a shear-constrained material system can be expressed as[155]

$$\tau = \sigma_{2\mathrm{D}} h_1 k \tanh\left(k a_x\right), \quad k = \sqrt{\frac{G_0}{h_0}\frac{1}{E_1 h_1}} \tag{6.1}$$

where h_0 and h_1 are the heights of the pedestal and the clamping pad, respectively, G_0 is the shear modulus of the pedestal, E_1 is Young's modulus of the clamping pad, and σ_{2D} is the initial two-dimensional stress in the device layer. This results in the contraction of the clamping pad by Δp from its original half-width a_x:

$$\Delta p = \frac{h_0}{G_0}\tau = \frac{\sigma_{2\mathrm{D}}}{E_1 k}\tanh\left(k a_x\right). \tag{6.2}$$

In consequence, the tensile stress in the clamping pad is reduced to

$$\sigma_\mathrm{p} = \sigma_{2D} - E_1 \frac{\Delta p}{a_x} \tag{6.3}$$

according to Hooke's law. Note that a similar model that also accounts for additional shear in the device layer is presented in Ref. [156]. For the sake of simplicity, we neglect the minute counterforce exerted by the presence of the resonator, which will lead to a slightly reduced contraction of the pad to which it is attached. An experimental verification of the contraction of the clamping pad following the vertical release is discussed in Sec. 6.4.

Undercut of Clamping Pads from Lateral Release

The lateral release of the nanostrings results in an undercut of the clamping pads. More specifically, the width of the pedestal is reduced by a_{uc} from all sides such that the rim of the clamping pad gets freely suspended as shown in Figs. 6.3 (c) and 6.4 (f). This enables a relaxation of the tensile force in the undercut parts of the pads (as they are no longer counteracted by the material underneath) that gives rise to a contraction by an amount Δc. The resulting contracting force acting on the interface between the clamping pad and the nanostring can be expressed as

$$F_{\mathrm{c}} = \sigma_{\mathrm{p}} A_{\mathrm{p}} - E_1 \frac{\Delta c}{a_{\mathrm{uc}}} A_{\mathrm{p}}, \tag{6.4}$$

where σ_{p} is the remaining tensile stress in the clamping pad following the vertical release, and $E_1 \frac{\Delta c}{a_{\mathrm{uc}}}$ is its reduction in the undercut part of the clamping pad, again according to Hooke's law. Note that in the absence of the nanostring, the suspended part of the clamping pad fully relaxes such that $F_{\mathrm{c}} = 0$. In the presence of the nanostring, however, the contracting force of the clamping pad is counteracted by a second force acting on the interface between the clamping pad and the nanostring which is associated with the elongation ΔL of the nanostring

$$F_{\mathrm{s}} = \sigma_{\infty} A_{\mathrm{s}} + E_1 \frac{\Delta L}{L} A_{\mathrm{s}}, \tag{6.5}$$

where σ_{∞} is the one-dimensional stress of an infinitely long nanostring after the lateral release, and $E_1 \frac{\Delta L}{L}$ is its modification according to Hooke's law.

The equilibrium condition for the clamping pad - nanostring interface

$$F_c = F_s \tag{6.6}$$

determines the final geometric reconfiguration of the clamping pad and the string, under the boundary condition that the total length of the compound between the centers of the clamping pads has to be conserved,

$$2\Delta p + 2\Delta c = \Delta L. \tag{6.7}$$

Equations (6.6) and (6.7) form a second-order system of linear equations with the unknown parameters ΔL and Δc. The third unknown Δp is determined using Eq. (6.2). Solving for the elongation of the resonator yields

$$\Delta L = 2L \, \frac{(A_{\mathrm{p}} a_{\mathrm{uc}} \sigma_{\mathrm{p}} + A_{\mathrm{p}} E_1 \Delta p - A_{\mathrm{s}} a_{\mathrm{uc}} \sigma_{\infty})}{E_1 \, (2 A_{\mathrm{s}} a_{\mathrm{uc}} + A_{\mathrm{p}} L)}. \tag{6.8}$$

This length change of the resonator directly translates into an additional strain $\varepsilon = \Delta L/L$, giving rise to a length-dependent stress $\sigma(L)$ of the doubly clamped string resonator via Hooke's law

$$\sigma(L) = \sigma_\infty + E_1 \frac{\Delta L}{L}. \tag{6.9}$$

To validate the theoretical model, we fit Eq. (6.9) to the experimental data measured on all four material systems, using the geometric and material parameters specified in Tabs. 6.1 and A.4. The initial two-dimensional stress σ_{2D}, which is needed to determine σ_p, can be calculated from the epitaxial lattice mismatch of the crystalline InGaP sample. Following the calculations of Ref. [101], we obtain a value of of 0.95 GPa, which is used as a input parameter for the model. In principle, the same argument can be made for SiC which is also an epitaxially grown crystalline thin-film material. However, as already discussed in Sec. 3.1.1, the crystallization of 3C-SiC atop a Si wafer is more complex due to the large lattice mismatch. Therefore, the tensile stress can not be calculated and we set σ_{2D} as an additional fit parameter for SiC. The same applies for the amorphous thin-film materials SiN-FS and SiN-Si. The one-dimensional stress σ_∞ is employed as a fit parameter for all material systems. The results of the fits are included in Fig. 6.2 as solid lines. The shaded area represents the model's uncertainty arising from the error of the input parameters. As long as $A_s \ll A_p$ and $a_{uc} \ll L$, the length dependence of Eq. (6.9) can be approximated as $\sigma(L) \propto 1/L$. This holds true for all nanostrings under investigation, such that a $1/L$ dependence of the stress can be assumed. We find remarkable agreement between the model and the experimental data. This is particularly noteworthy for the case of the InGaP samples for which only one fit parameter, σ_∞, is employed. In the above approximation of small $A_s a_{uc}$ it corresponds to a vertical offset and thus the limit $\sigma(L \to \infty)$. Also the results for SiN and SiC, which involve two fitting parameters, show good agreement between the model and the experimental data. Again, σ_∞ can be interpreted as the tensile stress of an infinitely long string, whereas the two-dimensional stress in the as-grown device layer σ_{2D} can, at least to some extent, be compared to literature values.

In Tab. 6.2 we summarize the parameters obtained from the elastic model as well as the fit parameters for the case of the longest strings. The as-grown two-dimensional stress in low-pressure chemical vapor deposition (LPCVD) grown stoichiometric SiN on silicon is found to depend on growth conditions, but has been reported to amount to 1.1 GPa[26,157] and 1.4 GPa,[51] which is close to the value found here. The same applies for high stress 3C-SiC(111), for which an as-grown two-dimensional stress of 1.3 GPa has been reported,[95] which is somewhat lower than our result. But, as thoroughly discussed in section 3.1.2, the tensile stress in SiC depends

Table 6.2: Parameters of the elastic model for the case of a long string, as well as two-dimensional and one-dimensional stress. Adapted from Ref. [39].

	Δp (nm)	Δc (nm)	ΔL (nm)	σ_{2D} (GPa)	σ_∞ (GPa)
SiN-FS	8	6	28	3.18[a]	1.56[a]
SiN-Si	3	2	10	1.20[a]	0.90[a]
SiC	3	4	13	1.97[a]	1.05[a]
InGaP	3	5	15	0.95[b]	0.55[a]

[a]From fit
[b]Calculated with $\sigma_{2D} = \varepsilon^{\parallel} E_1/(1-\nu_1)$.[101]

significantly on the growth parameters. The growth of high stress SiN on a fused silica substrate is poorly characterized, and no comparison with the literature could be obtained. Certainly, all observed two-dimensional stress values are well within the yield strength of the respective material, which amounts to approximately 6-7 GPa (or even 12 GPa according to Ref. [158]) for high stress LPCVD-deposited SiN[26,157,159] and 21 GPa for SiC.[31]

A more general consideration of the length dependence of the tensile stress according to Eqs. (6.8) and (6.9) reveals that two geometric parameters, the height of the pedestal h_0 and the undercut of the pedestal a_{uc}, dominate the stress enhancement of short nanostrings. This suggests that maximum tensile stress can be achieved for short strings with large h_0 and a_{uc}. However, it has to be noted that this limit can only be achieved for sufficiently large clamping pads avoiding a softening of the entire clamping structure under overly large undercuts, an unwanted side effect that is not accounted for in our model.

Finally, we discuss the relation between σ_∞ and σ_{2D}. For a one-dimensional nanostring processed from a thin film under biaxial and isotropic stress, the one-dimensional stress follows from the initial two-dimensional stress according to

$$\sigma_{1D} = \sigma_{2D}(1-\nu_1). \tag{6.10}$$

For the nanostrings under investigation, this simple picture does not hold, as the stress relaxation along the y direction upon releasing the string assumes a more complicated stress configuration following the contraction of the device layer described by the first part of our model. Not only does the contraction of the clamps by an amount Δp reduced the two-dimensional stress in the clamping pads from σ_{2D} to σ_p. A similar contraction also occurs along the y direction of the string, such that the tensile stress in the string before the lateral release cannot be considered

isotropic. Additionally, we wish to note that high-resolution x-ray diffraction measurements performed on $In_{1-x}Ga_xP$ wafers have shown a compositional variation in the direction normal to the substrate.[101] This can furthermore lead to strain gradients inside the device layer. A similar observation has been made for 3C-SiC in Ref. [27]. This suggests that a more thorough analysis of the length-dependent stress should assume a three-dimensional strain tensor accounting for a vertical strain gradient rather than a biaxial isotropic thin-film stress σ_{2D}.

6.3 Finite Element Method Simulations

The geometric reconfiguration of the pedestal, the clamping pad and the string was explored in more detail by finite element method (FEM) simulations to validate our theoretical considerations. To this end, the individual 10 µm long and 300 nm wide SiN-FS string resonator held in place by two SiO_2 pedestals on a SiO_2 substrate shown in Fig. 6.5 is simulated. The thickness of the device layer is set to 100 nm, a 500 nm undercut and a pedestal height of 1 µm is assumed, as well as an initial two-dimensional tensile stress of 2.9 GPa. A perfectly matched layer is included to mimic an infinite substrate, but did not noticeably influence the result. A close look at Fig. 6.5 clearly reveals the shearing of the pedestal as well as the contraction of the clamping pad due to the stressed device layer. Also apparent is the resulting elongation and enhanced tensile stress in the string, which, for the case of the extremely short length of the simulated string, even exceeds the remaining tensile stress in the clamping pad. These observations qualitatively support all assumptions of the elastic model. Further FEM simula-

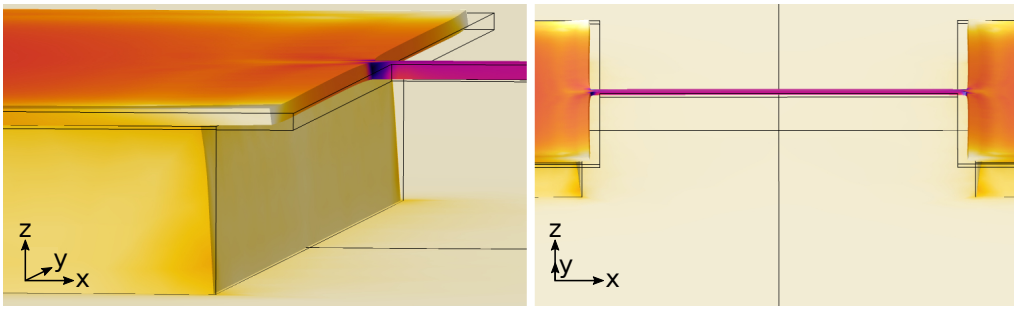

Figure 6.5: FEM simulations of a single string resonator with an initial stress of 2.9 GPa. The stress is color coded (the darker the color the higher the stress). Furthermore, we set a thickness of 100 nm for the device layer, a 500 nm undercut and a pedestal height of 1 µm. The black lines correspond to the original size of the individual structure. The deformation is exaggerated for better visibility. Adapted from Ref. [39].

tions and an in-depth analysis can be found in the thesis of Maximilian Bückle [34].

6.4 Measuring the Pedestal Contraction

To further support our elastic model, we have experimentally quantified the shearing of the pedestal using the test structures discussed in the following. An array of quadratic pedestals is fabricated on SiN-FS (see Fig. 6.6 (a,c)), the material for which the biggest contraction is expected (see Tab. 6.2). As shown in Fig. 6.6 (a,b), the uncontracted width of a pedestal is $2a$ and the pedestal-pedestal distance is d. An anistropic ICP-RIE etch step (etching depth of around 350 nm) allows for a contraction of the pedestal by $2\Delta p$ to $2a_{\mathrm{con}} = 2a - 2\Delta p$. Because the contraction

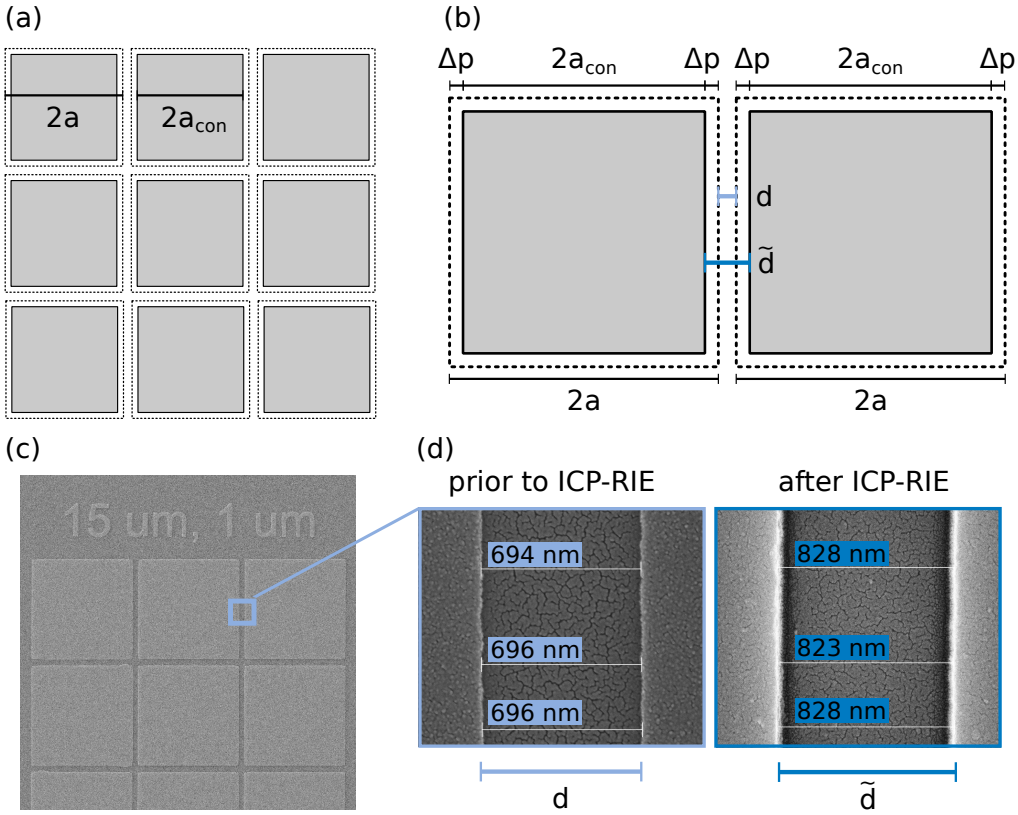

Figure 6.6: Array of pedestals (a) and a close up (b) including length annotations. Dashed lines and solid lines correspond to the pedestal before and after contraction, respectively. (c) SEM image of the array structure before it was etched. (d) SEM image of the gap between two pedestals before (left) and after (right) contraction. Taken from Ref. [39].

is in the nanometer regime and the pedestal in the micrometer regime, we can not simply image the whole pedestal and directly measure $2a$ and $2a_{\mathrm{con}}$ and calculate the contraction $2\Delta p$, as this is beyond the resolution of our scanning electron microscope. However, as indicated schematically in Fig. 6.6 (b), the separation of two closely-spaced pedestals of the test structure can be mapped out with a higher resolution. Comparison of their spacing before and after the contraction, d and $\tilde{d}$, respectively, indeed yields an increase of the gap as shown in Fig. 6.6 (d), indicating a contraction of the clamping structure. For our sample chip we measure an average value of $d = 793(6)$ nm.

6.5 Conclusion

In this chapter, we investigate the length dependent stress of nanomechanical string resonators fabricated on four different material platforms. For that, the stress of individual string is determined by fitting Euler-Bernoulli beam theory to its eigenmode spectrum. Across all four materials, we find that shorter strings are considerable more stressed. A simple elastic model, relying on the geometric reconstruction during vertical and lateral release, is used to describe the experimental findings. To a good approximation, the stress follows a $1/L$ dependence. Our model predicts that changes of the string's geometry can increase or decrease the resulting stress allowing to stress-engineer the quality factor.

7 Generalized Loss Dilution Model

The following chapter is based on our unpublished manuscript, which is in preparation:

Y. S. Klaß, I. Wilson-Rae, and E. M. Weig, *"Constancy of the undiluted inverse Q from the stress-diluted dissipation of crystalline nanomechanical resonators"*, unpublished manuscript (2022). Ref. [49]

The sample was fabricated by me (SiC). All measurements were performed by me. The theory was developed by Ignacio Wilson-Rae. The data analysis was performed by I. Wilson-Rae and me. The interpretation presented in this work relies on discussions of E. M. Weig, I. Wilson-Rae, and me. The theory is reproduced with the permission of I. Wilson-Rae. Figures are reproduced from Ref. [49].

So far, we have solely focused on the frequency of the measured eigenmode spectrum. Now we want to discuss the quality factor as a function of mode number. Ignacio Wilson-Rae developed a novel loss dilution model that is not limited to high stress string resonators in contrast to the often used model from Yu et al.[47]. As these models are very susceptible to the tensile stress values, we use Euler-Bernoulli beam theory with realistic doubly clamped boundary conditions to extract the resonator's stress from their eigenmode spectrum (see Sec. 7.1). With the dilution factor predicted by the model and the measured frequency, we can determine the intrinsic quality factor and loss angle over a frequency range of 80 MHz as shown in Sec. 7.3.

7.1 Euler-Bernoulli Beam Theory with Clamped Boundary Conditions

Simply supported boundary conditions (see Fig. 2.2), that are often utilized in the Euler-Bernoulli framework to describe string resonators, do not perfectly reproduce the actual shape of the eigenmodes, as already discussed in Sec. 2.1. It does offer, however, a very good approximation and, most notably, an exact analytical solution. Clamped boundary conditions reproduce the mode shape better but, up to date, there is no exact solution available (without e.g. Taylor expansion). Here, we present an analytical approximation. The calculations were performed by Ignacio Wilson-Rae and the derivation will be presented in our publication [49]. The out-of-plane frequency of a string resonator in the Euler-Bernoulli framework with doubly clamped boundary conditions can be approximated by[49]

$$f_n = \frac{n}{2L}\sqrt{\frac{\sigma}{\rho}\left(1+\frac{2}{L}\sqrt{\frac{Eh^2}{3\sigma}}+\frac{1}{L^2}\frac{Eh^2}{\sigma}\right)+\left(\frac{n\pi}{L}\right)^2\frac{Eh^2}{12\rho}}\,, \tag{7.1}$$

where L is the length of the resonator, n the mode number, σ the tensile stress, ρ the density, E the Young's modulus, and h the thickness of the device layer. Figure 7.1 shows a fit of Eq. (7.1) to the SiC eigenmode spectrum, which we already used in Chap. 5 and 6. The fit reproduces the measured data nearly perfectly for all available lengths. Interestingly, we get exactly the same course for clamped and

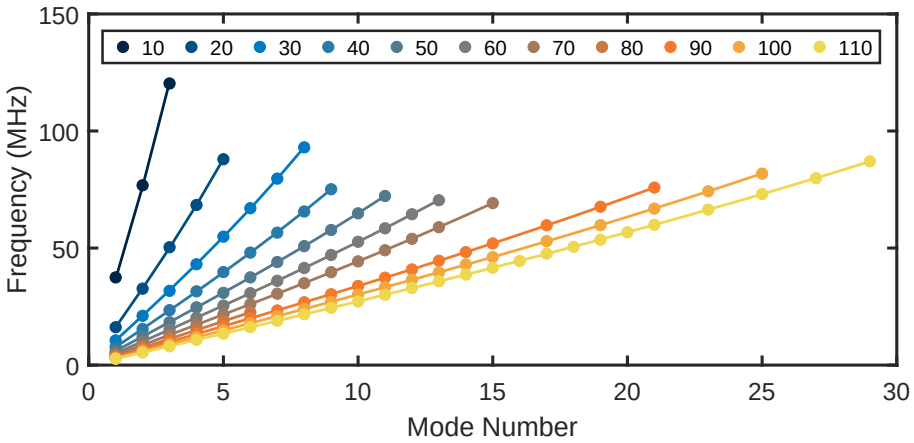

Figure 7.1: Eigenfrequencies of the oop modes as a function of the mode number. The measured frequencies of resonators of different lengths are shown as colored dots. Solid lines represent a fit of Eq. (7.1), i.e. the Euler-Bernoulli model with clamped boundary conditions. The data was recorded on sample A. Reproduced from Ref. [49].

simply supported boundary conditions (see App. D for a comparison). However, the fit with clamped boundary conditions yields slightly lower stress values, especially for the shorter strings.[a]

7.2 Generalized Dilution Model

In order to describe the behavior of the quality factor as a function of mode number, we introduce a new generalized loss dilution model. We omit here the derivation, but it will be included in our upcoming publication [49]. The loss dilution model has the general form

$$Q^{-1} = Q_{\text{intr}}^{-1}\, D_n^{-1}, \tag{7.2}$$

with Q_{intr} the intrinsic quality factor and D the mode dependent dilution factor. Additionally, we define the loss angle (sometimes also referred to as loss tangent or loss) as the inverse undiluted quality factor

$$\phi \coloneqq Q_{\text{intr}}^{-1}. \tag{7.3}$$

In the model derived by Ignacio Wilson-Rae the dilution factor is[49]

$$D_{\text{o/e,n}}^{-1} = \frac{k_n^2}{\kappa(k_n)^2}\, \frac{1 \pm \frac{\sin(k_n L)}{k_n L} \mp \frac{\kappa(k_n)}{k_n^2 L}\, \frac{1 \mp \cos(k_n L)}{1 \mp \cosh(\kappa(k_n) L)}\, [\sinh(\kappa(k_n) L) \pm \kappa(k_n) L]}{1 \pm \frac{\sin(k_n L)}{k_n L} \mp \frac{k_n^2}{\kappa(k_n)^3 L}\, \frac{1 \mp \cos(k_n L)}{1 \mp \cosh(\kappa(k_n) L)}\, [\sinh(\kappa(k_n) L) \pm \kappa(k_n) L]}, \tag{7.4}$$

where $\kappa(k_n) = \sqrt{k_n^2 + \kappa_0^2}$, $\kappa_0^{-1} = \sqrt{\frac{Eh^2}{12\sigma}}$ the penetration depth of the end correction (from the clamped-clamped boundary conditions) in the string, and $k_n L$ with $n \in \mathbb{N}$ the roots of

$$0 = 2k\kappa(k)\,(1 - \cos(k)\cosh(\kappa(k) L)) + \kappa_0^2 L^2 \sin(k)\sinh(\kappa(k) L). \tag{7.5}$$

The signs ($\pm$ and $\mp$) in Eq. (7.4) depend on the parity (odd / even) of the mode number. While the intrinsic quality factor is a constant material parameter (as we show later), D decreases with increasing mode number. For example, the first and 17th mode of the 110 µm string feature a dilution factor of 88 and 11, respectively. In contrast to the model from Yu et al.[47], we do not rely on the string approximation, i.e. high tensile stress and low mode numbers with $\kappa_0 L \gg 1$ and $\kappa_0^2 \gg k_n^2$. Figure 7.3 shows the inverse dilution factor for the dissipation dilution model with (dashed line, referred to as established model) and without

[a] The elastic model of Chap. 6 does still fit the stress values very well (see App. D).

(solid lines, advanced model) assuming the string approximation. Note that $\kappa_0 L$ is a dimensionless parameter that depends on the stress and length of the considered string. While the advanced model converges to a value of one for vanishing stress, the established model diverges due to the invalidity of the string approximation in this regime. Physically, we expect that $\lim_{\sigma \to 0} D = 1$ and $D^{-1} \leq 1$ as an inverse dilution factor greater than one would actually decrease the intrinsic quality factor. As $\kappa_0 L$ increases, both models converge because the string approximation becomes more valid. Furthermore, we can see that for low mode numbers, the deviation is

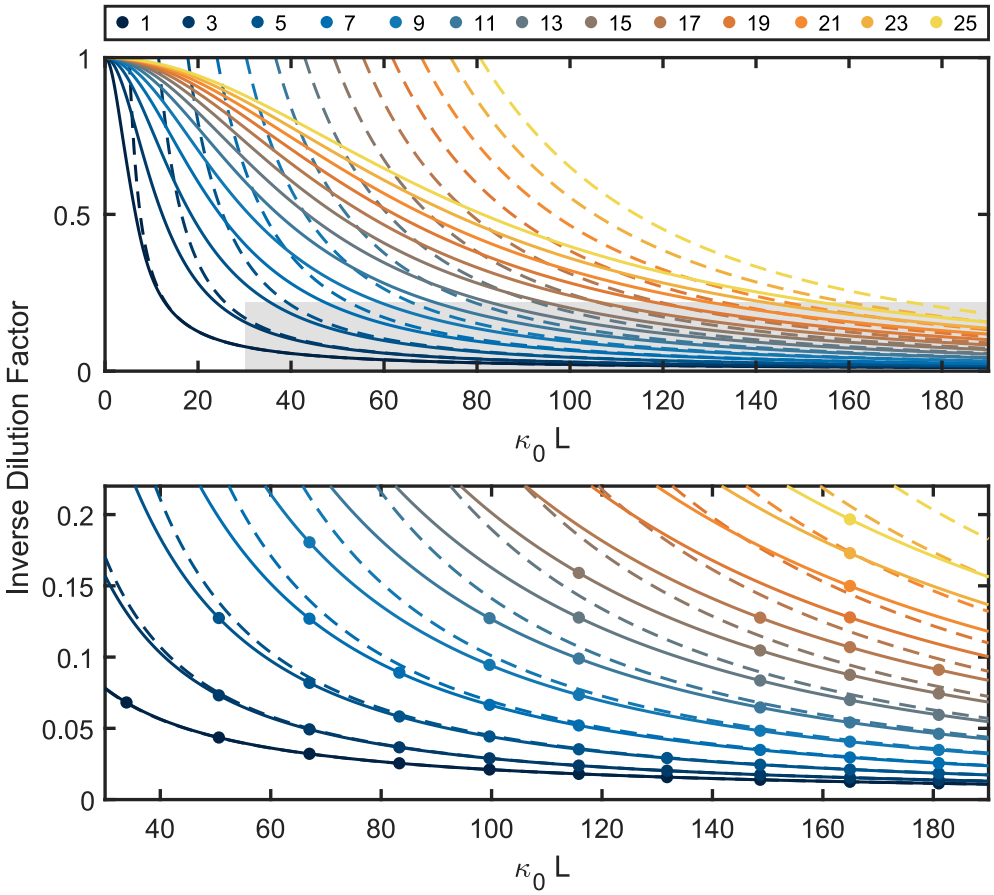

Figure 7.2: Inverse dilution factor as a function of the dimensionless parameter $\kappa_0 L$. The solid and dashed lines correspond to a loss dilution model assuming and not assuming the string approximation, respectively. Different colors symbolize different modes. For the sake of visibility, we omit even mode numbers at this point, but they are shown in App. E. Colored dots depict the parameters $\kappa_0 L$ and n of our resonators. The gray shade in the upper figure indicates the parameter space of the lower plot. Adapted from Ref. [49].

smaller than for higher mode numbers. In fact, for the first and second mode (see App. E), there is barely any deviation (except for $\kappa_0 L < 20$). On the other hand, the deviations are beyond 20 % for very high mode numbers.

Now we fit our advanced loss dilution model (i.e. Eq. (7.2) with (7.4)) to the measured quality factors as shown in Fig. 7.3.[b] We generally find a very good

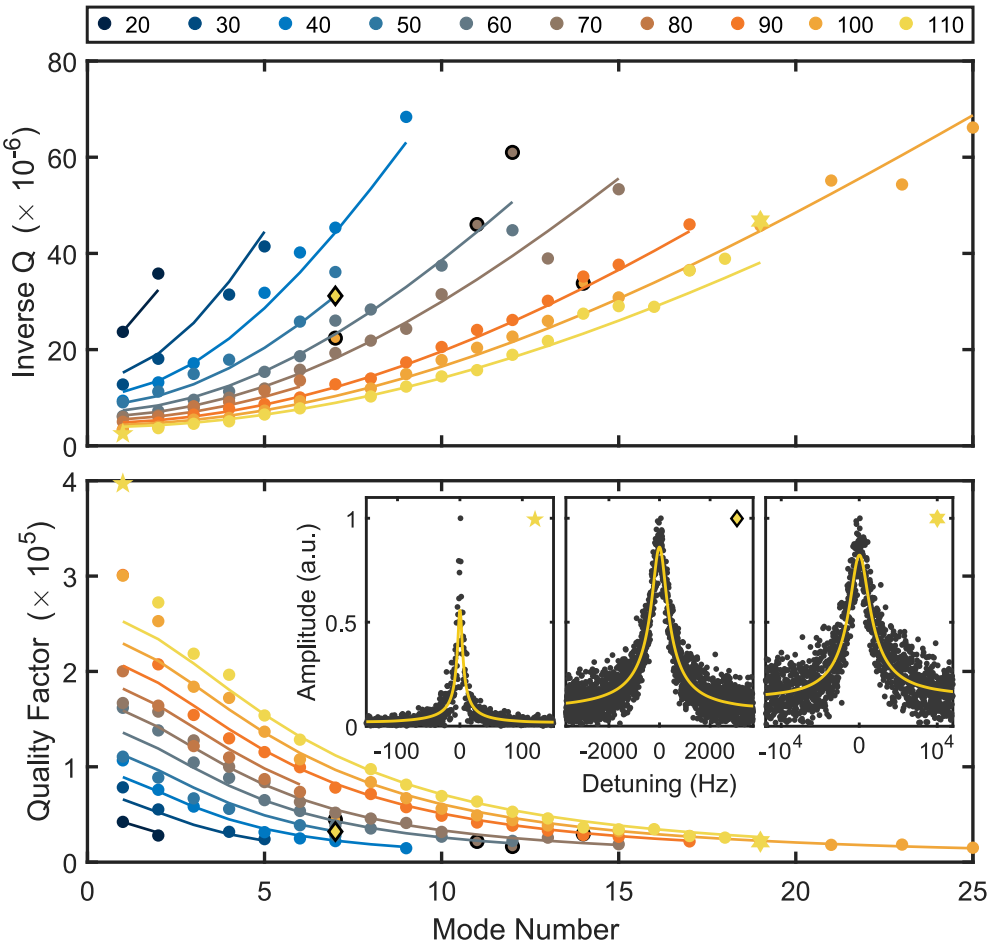

Figure 7.3: Inverse and regular quality factor as a function of mode number. Different colors correspond to different resonator lengths. Colored dots and solid lines are the measured data points and the fit of Eq. (7.2), respectively. If a colored dot has a black contour, it is ignored by the fitting algorithm. The insets show the amplitude response of the diamond and stars. The yellow line corresponds to the Lorentzian fit that is used to extract the quality factor. The data was recorded on sample A. Adapted from Ref. [49].

[b] Here, we use the stress values from Euler-Bernoulli beam theory with doubly clamped boundary conditions (see Sec. 7.1).

agreement, especially for higher mode numbers and strings shorter than 90 µm. The model slightly underestimates the first mode of the three longest strings. In fact, the biggest deviation is found for the fundamental mode of the 110 µm string, where we measure 397 000 and the model predicts 252 000.[c] The established model from Yu et al.[47] has a comparable deviation to this data point. However, for mode numbers bigger than two, the deviation drops below 4 % for this string.

7.3 Constant Loss Angle

More than 20 years ago, several groups measured on macroscopic objects that the intrinsic quality factor or (undiluted) loss angle should be independent or only weakly dependent on the frequency.[44,160,161] In 2018 Fedorov et al.[50] presented measurements indicating a constant loss angle for nanomechanical resonators. With the dilution factor determined by our model and the measured quality factors, we are able to calculate the intrinsic quality factor and loss angle with equation (7.2). Note that this is only valid if clamping losses can be neglected, as it will be discussed in detail in our upcoming publication [49]. To rule them out, the quality factors of all modes are measured twice. First on a thin aluminum sample holder ($25 \times 20 \times 2.5\,\mathrm{mm}^3$, see Fig. 4.3 (a)) and then on a very chunky copper holder ($25 \times 20 \times 20\,\mathrm{mm}^3$). For the case of clamping-loss limited resonators, the higher acoustic mismatch and the higher density of copper should reduce the clamping losses and, therefore, increase the measured quality factors.[52,162,163] However, the measurements are very similar, i.e. the resonators are not limited by clamping losses. Figure 7.4 shows the resulting intrinsic quality factor and loss angle over a frequency range of 80 MHz. In the presented frequency range, both the loss angle as well as the intrinsic quality factor are nearly constant. This was already suggested by measurements on macroscopic[44,160,161] and nanomechanical[50] devices, but it was never measured on such a wide frequency range. For very low frequencies, we find three outliers corresponding to the fundamental modes ($n = 1$) of the three longest strings. As already discussed in Sec. 7.2 and shown in Fig. 7.3, the model underestimates these quality factors, resulting in an overestimation of the intrinsic quality factors (see Eq. (7.2)). The mean and standard deviation of the intrinsic quality factor and loss angle are $\bar{Q}_{\mathrm{intr}} = 2900(330)$ and $\bar{\phi} = 3.48(34)$, respectively.[d] According to literature, amorphous SiN string resonators have an intrinsic quality factor between 2000 and 4000.[34,50,52]. My colleague Maximilian Bückle[34] measured $Q_{\mathrm{intr}} < 2500$ for crystalline InGaP and, very recently, Beccari et al.[30] reported a value of 8400 for strained crystalline Si at 8 K. Keep in mind

[c] A similar behavior is found for a second SiC data set and for Maximilian Bückle's InGaP samples.

[d] Note that we included all data points and thus also the three outliers.

that cryogenic temperatures should result in lower intrinsic quality factors.[27,30] Generally, one would expect crystalline materials to exhibit fewer material defects and, therefore, a higher intrinsic quality factor. But what is limiting our intrinsic quality factor? Although the latter question is still open for SiC and there is currently no available literature on the topic, it is known that surface loss limits the intrinsic quality factor in SiN resonators for thicknesses below a few hundred nanometers.[52] Increasing the thickness of the string resonator and hence reducing the surface-to-volume ratio diminishes the effect of surface loss until the intrinsic quality factor is dominated by volume loss.[52] One option to validate if we are indeed

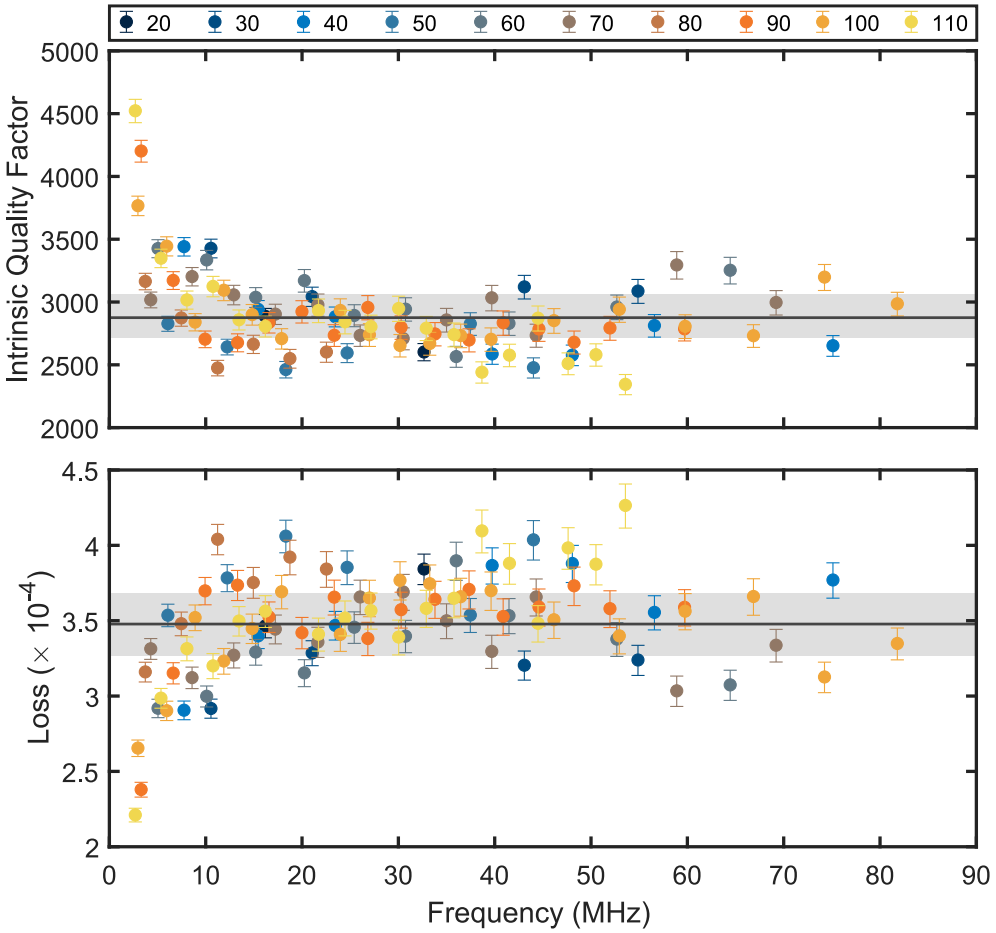

Figure 7.4: Intrinsic quality factor and (undiluted) loss angle as a function of frequency. The horizontal line and shade indicate the mean and standard deviation with values of $\bar{Q}_{\mathrm{intr}} = 2900(330)$ and $\bar{\phi} = 3.48(34)$. Colored dots correspond to different string lengths. The error bars give the uncertainty due to the uncertainty of the string's thickness. The data was measured on sample A. Adapted from Ref. [49].

limited by surface loss would be to perform a thickness-dependent measurement of the intrinsic quality factor. Alternatively, we could fabricate strings with different widths, which also affects the surface-to-volume ratio.
Taking another look at Eq. (7.2) one sees that there are two ways to boost the quality factor of our resonators, apart from applying considerable more complex methods such as soft clamping. The first is to increase the intrinsic quality factor. As just discussed, this could probably be achieved by reducing the surface-to-volume ratio. Secondly, we could increase the dilution, which is stress dominated. Raising the stress can be achieved by, e.g., optimizing the sample geometry (see Chap. 6) or by adapting the growth parameters of the wafer (see Chap. 3.1.2).

7.4 Conclusion

In this chapter, we introduce an analytical approximation of the Euler-Bernoulli beam theory for doubly clamped boundary conditions, showing very good agreement with our data. Furthermore, we discuss a loss dilution model developed by Ignacio Wilson-Rae. Compared to other models, it does not rely on the string approximation and is therefore valid for a significantly wider parameter range. This allows us to perform a comprehensive analysis of 99 resonator modes covering lengths between 20 µm and 110 µm, mode indices up to 25, and spanning a frequency range of 80 MHz. It reveals a constant stress angle, indicating that it is frequency independent, as already suggested by other groups for much smaller frequency spans.

8

SiC at Low Temperatures

Temperature dependent measurements of a material or device can be used to reveal information about the limiting loss mechanisms. One example are thermally activated defects, which are often modeled by two-level systems (TLS), as they lead to characteristic dissipation maxima.[30,164–168] To this end, we cool our SiC string resonators to cryogenic temperatures (see setup in Sec. 4.1.2). As described in

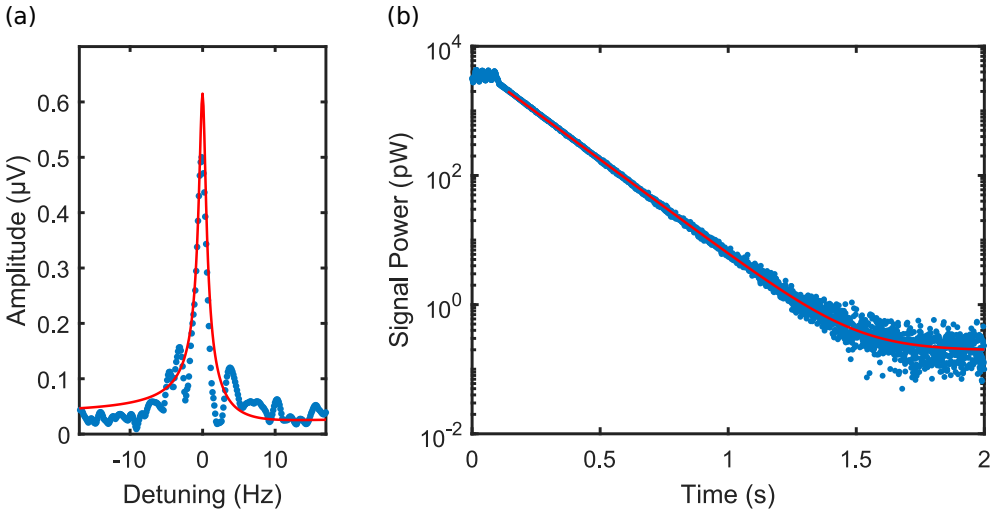

Figure 8.1: Thermal motion (a) and ring-down (b) of a 110 µm SiC string at 5.5 K. The blue dots correspond to measured data. The red lines are a complex Lorentzian and an exponential decay fitted to this data, yielding quality factors of $Q_{\mathrm{thm}} = 2.9 \times 10^6$ and $Q_{\mathrm{rd}} = 2.5 \times 10^6$, respectively. The thermal motion is only used to find the resonance frequency. The data was recorded on a 110 µm string of sample A.

detail in App. C, we determine the resonance frequency with the help of the thermal motion (if measurable) and the quality factor via a ring-down. Close to the base cryostat temperature, which is around 4.2 K, we reach the highest quality factors of 2.5 to 3.5 million for 110 µm SiC strings. The thermal motion ($f_0 = 2.72\,\mathrm{MHz}$) and a ring-down are shown in Fig. 8.1, illustrating the small linewidth ($\Gamma = 6.9\,\mathrm{Hz}$) and high quality factor ($Q_{\mathrm{rd}} = 2.5 \times 10^6$).

8.1 Temperature Dependent Frequency and Dissipation

Repeating the just presented measurement over a wide range of temperatures allows us to extract the temperature dependence of the frequency, quality factor, and dissipation. For that, we cool the system to base temperature (around 4.2 K) and utilize an internal resistive heater regulated by a PID (proportional–integral–derivative) controller. With that we can reach and stabilize temperatures ranging from base temperature up to 220 K. Another method that does not rely on the heater is to measure during the cool down procedure, where we can access temperature from 300 K down to 4.2 K. However, the sample position drifts during the cool down due to the susceptibility of the positioners to the temperature change. These drifts – that have to be corrected manually – lead to a change in the relative position of the laser beam and the resonator, causing a change in the local heating of the resonator and, therefore, the frequency.[a] Comparing the data of our cool downs reveals that the course of the frequency can not be extracted reliably (see App. F). However, as the behavior of the quality factor and damping are similar in every cool down, they seem slightly more trustworthy.

Figure 8.2 shows the frequency, quality factor and damping as a function of temperature. The frequency increases from 2.68 MHz at room temperature (RT) to 2.705 MHz at low temperatures with a small but broad dip at around 180 K. A frequency increase indicates a stress increase in the device layer. By comparing the thermal expansion coefficient of SiC and Si over a certain temperature range, we are able to predict the theoretical stress and frequency change. The thermal

[a] When using the heater, the drifts are significantly reduced because we only change the temperature locally around the heating element. During the cool down, on the other hand, the whole system is cooled, leading to more pronounced drifts. Furthermore, the cool down can not be paused and, hence, the temperature can never stabilize, i.e. we have to measure while the positioners are slowly drifting. At a temperature of around 40 K the positioners move to such an extent that we are not able to acquire any data anymore (see missing data in Fig. 8.2). Although a single data point is measured within 20 s, the small linewidth and the fast drift make it impossible to drive the resonator on resonance prior to a ring-down measurement.

expansion coefficient $\alpha(T)$ of a material is defined as[169]

$$\alpha(T) = \frac{1}{L_{\mathrm{RT}}} \frac{dL(T)}{dT}, \tag{8.1}$$

where T is the temperature, L_{RT} the length at RT, and $L(T)$ the length.[b] To

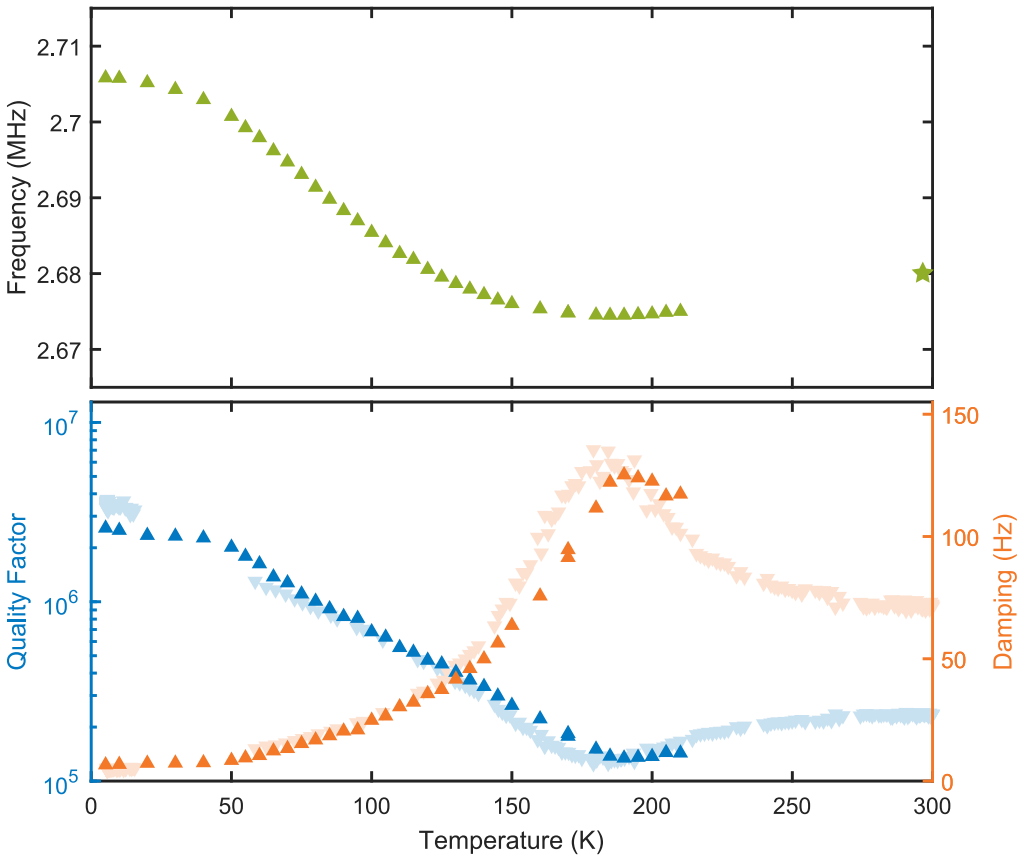

Figure 8.2: Measured frequency, quality factor, and damping as a function of temperature, recorded on a 110 µm SiC string. The temperature of the upward pointing triangles is set with the in-built heater. The shaded downward pointing triangles are acquired during a cool down of the cryostat. Note that for the shaded data, a slightly lower laser power is used, explaining the minor deviations in terms of quality factor and damping. The green star symbolizes the frequency at room temperature. The quality factor is plotted on a logarithmic scale for the sake of visibility. The data was recorded on sample A.

[b] We follow the ISO definition (also utilized in Ref. [169]). It uses the length at RT in the whole temperature range, which is in slight contrast to the physical definition.[169] However, the deviation is very small and therefore it is very convenient because we can measure the length of our resonator only at RT.[169]

calculate the expansion due to a temperature change from T_{RT} to T, we have to integrate Eq. (8.1), yielding

$$\int_{T_{\mathrm{RT}}}^{T} \alpha(\widetilde{T})\, d\widetilde{T} = \frac{1}{L_{\mathrm{RT}}} \left(L(T) - L(T_{\mathrm{RT}})\right) =: \frac{\Delta L_{\mathrm{T}}}{L_{\mathrm{RT}}}. \tag{8.2}$$

Hence, the length change ΔL_{T} is

$$\Delta L_{\mathrm{T}} = L_{\mathrm{RT}} \int_{T_{\mathrm{RT}}}^{T} \alpha(\widetilde{T})\, d\widetilde{T}. \tag{8.3}$$

A relative change of $\alpha(T)$ for Si and SiC leads to an additional strain $\epsilon(T)$ and stress $\sigma(T)$ in the material:

$$\sigma(T) = E\epsilon(T) = E\, \frac{\Delta L_{\mathrm{T}}^{\mathrm{Si}} - \Delta L_{\mathrm{T}}^{\mathrm{SiC}}}{L_{\mathrm{RT}}}, \tag{8.4}$$

where E is the Young's modulus. With the string model (see Eq. (2.3)) we can relate the additional stress to a frequency change

$$\Delta f(T) \approx \frac{1}{2L_{\mathrm{RT}}} \sqrt{\frac{\sigma_{\mathrm{RT}} + \sigma(T)}{\rho}} - f_{\mathrm{RT}}, \tag{8.5}$$

where f_{RT} and σ_{RT} are the frequency and stress at RT, respectively. While the literature provides reliable $\alpha(T)$ for Si,[169–171] it is scarce for SiC[134,172] in the temperature range relevant for us. For a rough approximation we use part of the values

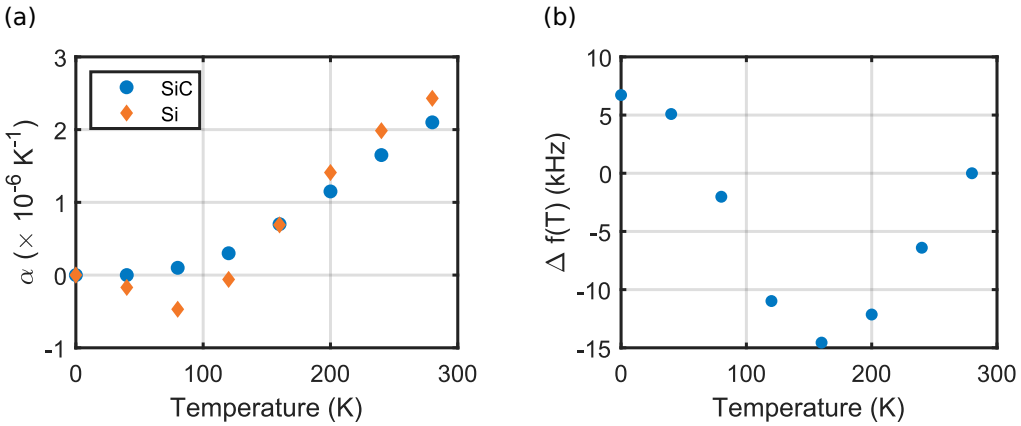

Figure 8.3: (a) Thermal expansion coefficient for Si[169] and SiC[134] as a function of temperature. (b) Calculated frequency change (see Eq.(8.5)) compared to room temperature of a 110 µm SiC string.

provided by Refs. [134] (SiC) and [169] (Si) as shown in Fig. 8.3 (a). By numerical integration of Eq. (8.3) and combining it with Eq. (8.5), we can approximate the frequency change as plotted in Fig. 8.3 (b). Similar to our measured data in Fig. 8.2, the model predicts a frequency dip at around 160 K with a frequency shift of 15 kHz, which is slightly more than the measured 5 kHz. Further, the model underestimates the frequency shift at base temperature by an order of magnitude. Note that the stress change and distribution in a real string is way more complex than assumed in our simple model since it includes e.g. shear and gradients.

Taking a close look at the dependence of the dissipation (quality factor) on the temperature, we can see that we have $\Gamma = 70$ Hz ($Q = 230\,000$) at RT and 6.6 Hz (2.6×10^6) at 5.1 K. Once fully thermalized, the damping drops just below $\Gamma = 5$ Hz, which corresponds to $Q = 3.6 \times 10^6$ (not shown).[c] As a rule of thumb, the quality factor improves by an order of magnitude when cooled to low temperatures. The dissipation peak at 190 K is in agreement with measurements performed on SiO_2,[167] SiN,[168] and Si[30] and can most likely be attributed to thermally activated defects.

Figure 8.4 shows a more detailed measurement performed between 5 K and 31 K. For that, we first heat the sample from 5 K to 35 K in steps of 2 K (orange upward pointing triangle). We let the sample thermalize at every temperature for an hour before the frequency, quality factor, and damping are measured several times. We calculate the mean and standard deviation, which are shown as symbols and error bars (hardly visible) in Fig 8.4. Then the sample is cooled back in exactly the same manner (blue downward pointing triangle). Intuitively, one would expect that both paths yield the same results. Around 23 K, however, we can see a hysteresis: If we are heating the system, we get a damping dip (peak in quality factor), reaching values of $\Gamma = 11$ Hz ($Q = 1.6 \times 10^6$). If we are cooling the sample, on the other hand, the dip is barely reproduced, but we get a nearly constant behavior in the presented temperature range with a value of 7 Hz (2.3×10^6) at 23 K. Note how the two paths of the quality factor and dissipation are merging at 15 K and 28 K. This does not hold true for the frequency, where the two paths are not merging again. Upon very close inspection, one can notice a saddle point of the orange frequency data at 23 K, which can not be found in the blue data set.
In the literature, a hysteresis of the dissipation due to temperature change has never been reported. We want to point out that it could also be an artifact which is not

[c] As mentioned before, sample A, on which this data was measured, degraded over time (it probably accumulated dirt in the course of a year). Therefore, one has to be careful when comparing different figures/measurements. However, the data presented in one figure are always comparable as recorded within a relatively short time period.

originating from the sample.[d] As thoroughly discussed in Sec. 8.3, the damping dip is indeed reproduced for thermalization times of multiple days. This suggests that both sets of measurements do follow the same path. The work of Zink et

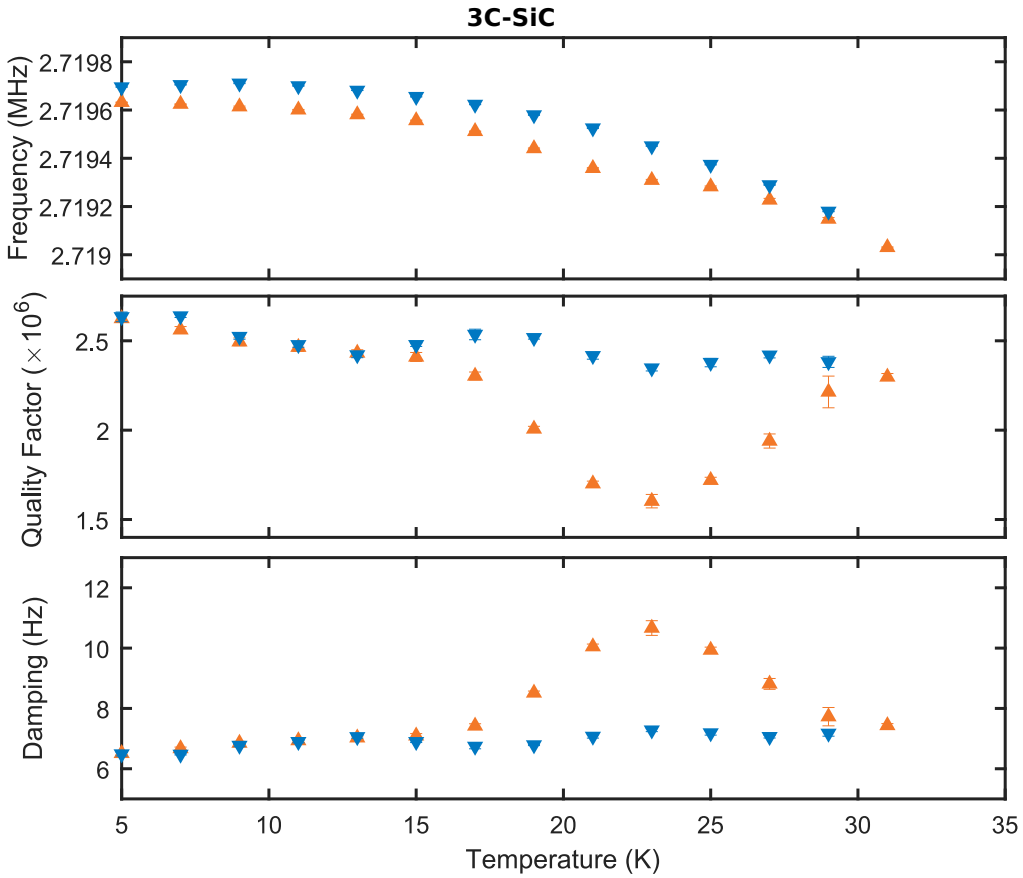

Figure 8.4: Measured frequency, quality factor, and damping as a function of temperature, recorded on a 110 µm SiC string. The frequency is extracted via the thermal motion and the quality factor, and damping via ring-downs. The temperature is controlled with the help of a heater. We start at 5 K and increase the temperature gradually to 31 K. The corresponding data is shown as orange upward pointing triangles. Then the temperature is slowly decreased again, shown as blue downward pointing triangles. Symbols and error bars are the mean and standard deviation (hardly visible) of several measurements performed at one temperature. The data was recorded on sample A.

[d]This includes foremost a bad thermalization of the sample (see Sec. 8.3). Alberto Beccari suggested that the hysteresis could be caused by the condensation of residual gas molecules on the sample surface or by mechanical vibration of the compressor. Another possibility is a phase transition in the materials of the positioning system, which was considered unlikely by Attocube engineers.

al.[166] suggests the presence of TLS for similar temperatures in Si that could cause another dissipation dip similar to the one at 180 K.
The bad thermalization should reveal itself in the form of a dip in the thermal conductivity K. According to the data shown in Ref. [78], K is following the expected T^{-N} behavior at this temperature with $N = 1.8$ (see App. G). Si, on the other hand, has a thermal conductivity maximum around 20 K, indicating that the substrate is not the heat flow bottle neck.[173–175]

8.2 Comparison to InGaP

To better understand the hysteresis, we performed the same measurement on an InGaP sample.[e] In Fig. 8.5, the temperature dependence of the frequency, quality factor, and damping are shown between 5 K and 70 K. We follow the same procedure described in Sec. 8.1 for SiC. Due to a power outage, we could, unfortunately, not finish the blue data set.
Generally, we can find a very similar behavior as for SiC. This includes the dissipation dip in the orange data (increasing temperatures) that is not reproduced in the blue data (decreasing temperatures). If the sample thermalizes for several days, the dissipation is actually reproduced, as shown by the light blue data with the black edge in Fig. 8.5 (see Sec. 8.3 for more details). In the range between 30 K and 65 K both paths match perfectly. The orange frequency data exhibits a dip at 20 K, which is not reproduced by the blue data.

8.3 Long Thermalization

In the previous section, the thermalization time between two temperature steps was around one (SiC) to two (InGaP) hours. Now we increase the time for InGaP by an order of magnitude to analyze how the frequency and dissipation behave once the sample is fully thermalized. For that, we heat the sample to 56 K and then reduce the temperature to 5 K and track frequency and damping over several hours. As shown in Fig. 8.6, the damping stabilized nearly instantly while the frequency continues to drift linearly even after seven hours. The frequency detuning over the whole measurement sums up to 0.7 kHz.
Next, the system is heated to 22 K, which is right in the dissipation dip. Here, we are following the orange path of Fig. 8.5. In a day, the damping increases linearly from 11 Hz to 13 Hz. Note the kink in the course of the frequency detuning after a few hours. Within the measurement time, the sample drifted about 1 kHz.

[e] The sample was fabricated by my colleague Maximilian Bückle. All measurements and the data analysis were performed by myself.

Heating the sample further to 33 K reveals a comparatively fast stabilization of both frequency and damping. After two hours, the string resonator seems nearly completely thermalized.

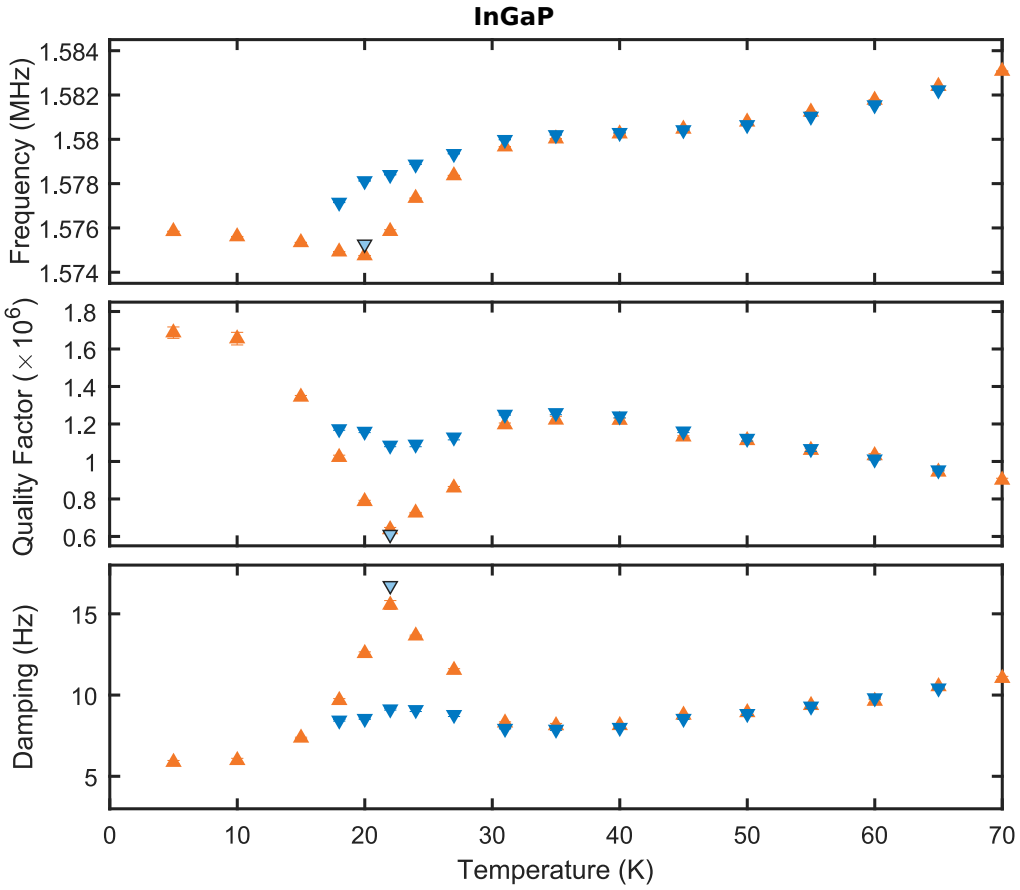

Figure 8.5: Measured frequency, quality factor, and damping as a function of temperature, recorded on a 110 µm InGaP string. While the frequency is extracted by a frequency sweep performed on a VNA, the quality factor, and damping is determined via ring-downs. The temperature is controlled with the help of a heater. We start at 5 K and increase the temperature gradually to 70 K. The corresponding data is shown as orange upward pointing triangles. Then the temperature is slowly decreased again, shown as blue downward pointing triangles. Between two temperature steps, the system thermalizes for at least two hours. The light blue triangles with the black edge indicate the frequency, quality factor and damping after thermalizing for more than 81 h. They correspond to the data marked in Fig. 8.6. Triangles and error bars are the mean and standard deviation (hardly visible) of several measurements performed at one temperature. The data was recorded on sample C.

Now we cool the sample back to 22 K, by which we are jumping to the blue path of Fig. 8.5. Even after more than 81 h the sample is still not fully thermalized. In course of this time the damping (quality factor) increased from 7.4 Hz (1.35×10^6) to 16.6 Hz (0.60×10^6) and the frequency shifted by more than 4 kHz. Again we see a kink in the course of the frequency.

With those long time measurements, we have gained some interesting insights: Outside the dissipation dip, the damping stabilizes rapidly. This is expected from Figs. 8.4 and 8.5 where both measurement paths match perfectly in terms of damping. The frequency at 5 K, on the other hand, drifts towards lower frequencies even after hours.
Within the dissipation dip (i.e. at 22 K) the thermalization of the dissipation is dramatically slower. Fitting a linear model to the two data sets (5 K→ 22 K and 33 K→ 22 K, fit not shown) yields a very similar rate of 0.1 Hz h^{-1} for both. Consequently, the difference is not the thermalization rate but the starting point,

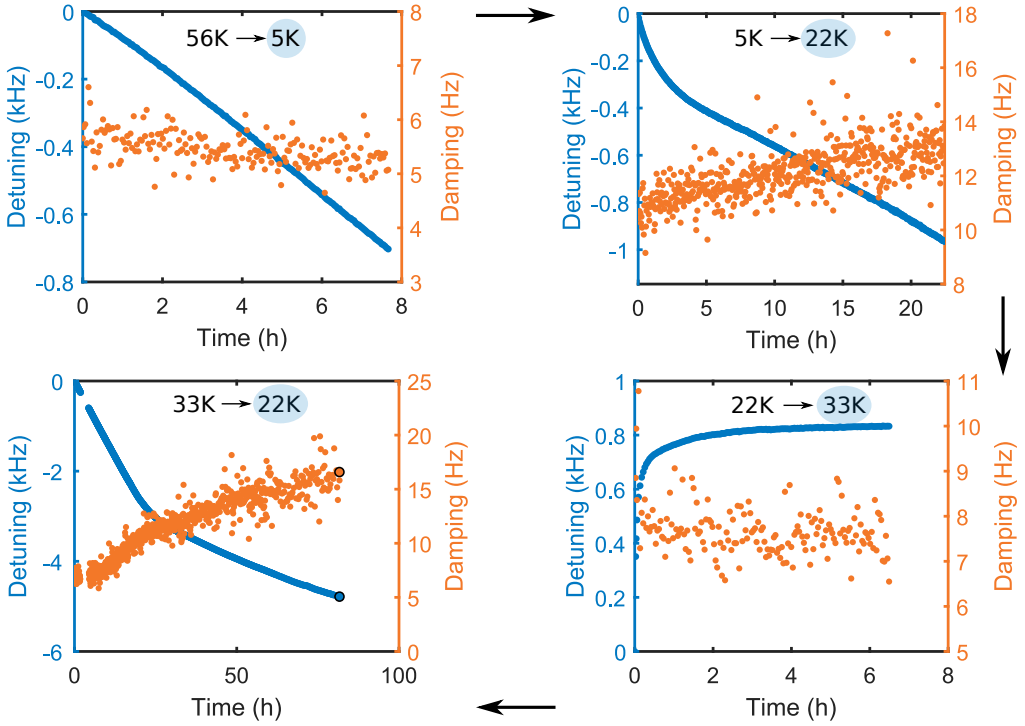

Figure 8.6: Frequency and damping of an InGaP string as a function of thermalization time for four different temperature transitions. The two temperatures stated on top of each plot give the current (right side, marked with blue shade) and previous temperature (left side). The data with the black edge in the lower right image is also plotted in Fig. 8.5. The data was recorded on sample C.

which is 11 Hz (5 K→ 22 K) and 7 Hz (33 K→ 22 K), respectively.[f]

8.3.1 Improving the Thermalization

As mentioned earlier, several possibilities could cause the hysteresis-like behavior. Arguably the most probable option is a bad thermal contact of the string resonators to the cryostat's cold head. In this section, we discuss the possible countermeasures to improve the thermalization of our sample.

Improved Sample Holder

We discussed this already in Sec. 4.1.3. In summary, the first generation of sample holders has a slight bow, leading to a small contact area to the underlying material and, hence, a low heat flow. Furthermore, conductive silver instead of an old photoresist is used to glue the sample to the holder, which should also enhance the thermal contact. However, we could not find a change in the previously discussed features.

Dielectric Drive

While all measurements shown in this chapter are actuated by a piezo, we also tried the dielectric drive (see Chap. 9 and Sec. 2.4). Consequently, we glue the sample directly to the sample holder without needing a piezo element in between. This test was already performed on a second generation sample holder. Again, the behavior of the sample remained unchanged.

Stroboscopic Measurement

The incoming laser light we use for detection heats the string resonator due to absorption. To minimize this effect, we operate the laser at the lowest power possible, which is around 1 mW. Note that this is the output power of the laser and the power reaching the string resonator is significantly lower. In order to showcase that we are not limited by laser heating, we repeat the measurement 33 K→ 22 K presented in Fig. 8.6. This time, however, the laser is mostly blocked and we just unblock it to measure a single data point every few hours. In Fig. 8.7 we compare the two measurement methods and find a remarkable agreement over hours. We conclude, therefore, that there is no laser heating for these parameters at this temperature. In App. H, we show a string resonator heated by a laser.

[f] These values correspond to the intercepts of the linear fits.

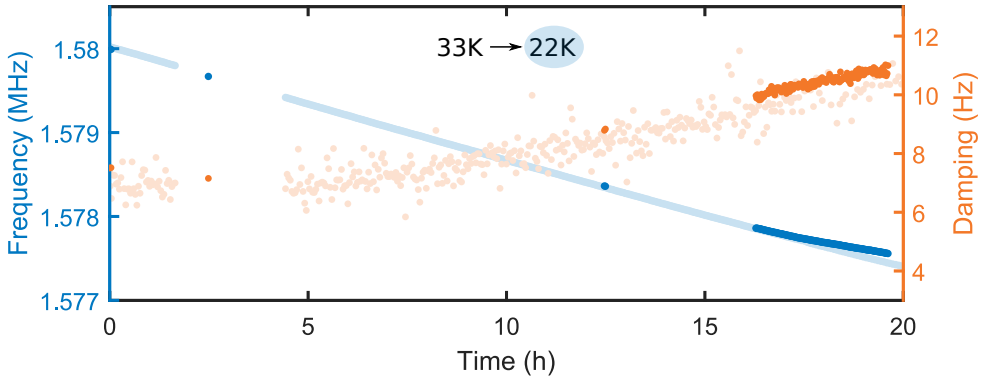

Figure 8.7: Stroboscopic measurement of the frequency and damping to rule out laser heating of a 110 µm InGaP string. The measurement is taken at a temperature of 22 K coming from 33 K. Blue and orange dots belong to the stroboscopic measurement and shaded dots of the respective color to the same measurement performed without blanking the laser (see bottom left of Fig. 8.4). The data was recorded on sample C.

Better Connection to Cold Head

Prof. Dr. Elke Scheer suggested to use fine copper threads to establish a better thermal connection between the sample and the cold head. However, this has not been tested yet but is subject to further investigation.

Shorter String Resonators

Each string can only be thermalized via two small clamping points. Therefore, it could be beneficial to use shorter string resonators, which should thermalize faster as they store less heat. However, this has not been tested yet but is subject to further investigation.

Different Setup

In order to rule out any side effects of the setup on the measurement, we could run the same measurements in a different setup. However, this has not been tested yet but is subject to further investigation.

8.4 Conclusion

In this chapter, we investigate the temperature dependence of the frequency and damping of nanomechanical SiC string resonators. The mismatch of the thermal expansion coefficients partly explains the frequency tuning. A dissipation peak

at 180 K indicates thermally activated defects, which agrees with measurements performed on amorphous SiN and strained crystalline Si. At around 23 K we find another dissipation dip, which seems, at first glance, to depend on the direction of the temperature sweep. Long thermalization measurements reveal that the dip is reproduced in both temperature sweep direction with thermalization times of multiple days. Again, thermally activated TLS could explain this feature. We expect to gain further insight into TLS by reducing the temperature to the millikelvin regime, where resonant absorption of phonons should occur.[176]

9 Dielectric Drive

In this chapter, we implement the dielectric driving scheme with SiC string resonators, enabling us to tune both the frequency and the damping. The leakage current of our doped wafers melts the bond wires for voltages above half a volt. Therefore, we employ a new set of not intentionally doped wafers that reduce the current to a similar level as for insulating SiN. While the dielectrically driven resonators presented in this work suffer from low quality factors ($Q < 100\,000$), the etching process has recently been optimized, allowing for quality factors $>200\,000$ as shown in Felix David's master thesis [177].

9.1 Dielectric Tuning

The dielectric actuation scheme enables us to tune the frequency and the dissipation quadratically by applying a dc voltage to the electrodes (see Sec. 2.4). In order to measure the frequency tuning, we first fix the dc voltage and give the system about 30 min to stabilize. Then, we perform a VNA sweep (see Sec. 4.2) and extract the resonance frequencies of the oop and ip mode. Afterwards, the voltage is changed and the procedure repeated. Figure. 9.1 shows the frequency tuning for a 100 µm SiC string at a temperature of 90 K. The upper and lower branch correspond in this case to the ip and oop mode, respectively.[a] Clearly, the frequency shift is stronger for positive than for negative voltages, which does not agree with the measurement performed on SiN.[63,64] This tuning behavior is found to be very reproducible and does not depend on the sweep direction of the voltage. To capture the asymmetry,

[a] This is in agreement with Euler-Bernoulli beam theory as our strings are fabricated wider than their thickness.

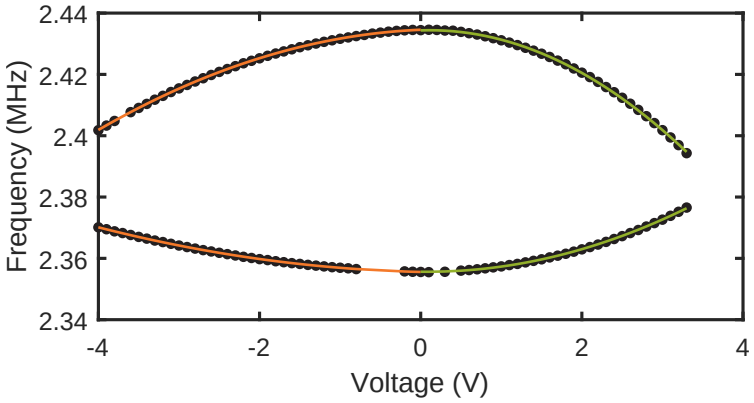

Figure 9.1: Resonance frequency of the fundamental oop and ip mode as a function of voltage. Dark blue dots correspond to measured data and colored lines to quadratic fits. In order to take the asymmetric behavior into account, we fit Eq. 9.1 to the data, which considers negative (orange line) and positive (green line) voltages separately. Data points with an insufficient signal-to-noise ratio are excluded. The data was recorded on a 100 µm string of sample G at 90 K.

we fit a function on the form

$$f(U_{\mathrm{dc}}) = \begin{cases} f_0 + c_{\mathrm{dc}-}(U_{\mathrm{dc}} - U_0)^2 & \text{for } U_{\mathrm{dc}} \leq 0, \\ f_0 + c_{\mathrm{dc}+}(U_{\mathrm{dc}} - U_0)^2 & \text{for } U_{\mathrm{dc}} > 0 \end{cases} \tag{9.1}$$

to our data, yielding the coefficients

$$c_{\mathrm{dc}-}^{\mathrm{ip,90K}} = -1.76\,\mathrm{kHz\,V^{-2}}, \qquad c_{\mathrm{dc}+}^{\mathrm{ip,90K}} = -3.90\,\mathrm{kHz\,V^{-2}},$$
$$c_{\mathrm{dc}-}^{\mathrm{oop,90K}} = 0.76\,\mathrm{kHz\,V^{-2}}, \qquad c_{\mathrm{dc}+}^{\mathrm{oop,90K}} = 2.00\,\mathrm{kHz\,V^{-2}}.$$

Positive voltages shift the frequency approximately twice as much as negative voltages. Similar to Ref. [63], we also find that the ip tunes twice as fast as the oop mode. The offset voltage U_0 is below 0.5 V for all fits and takes into account trapped charges in the resonator's material that shift the vertex of the parabolas.[63] Rieger et al.[63] report $c_{\mathrm{dc}} = 0.438\,\mathrm{Hz\,V^{-2}}$ for the oop mode of a 55 µm SiN string resonator, which is lower than our values. Note, however, that c_{dc} is influenced by many parameters like the resonator's mass and frequency. Therefore, the comparison should be treated with care and we do not dare to make conclusive statements about the materials.

Not only the frequency depends on the applied dc voltage but also the damping as shown in Fig 9.2 for low (5 K) and room temperature. Again we can see an asymmetry between positive and negative voltages. Therefore, we fit an equation

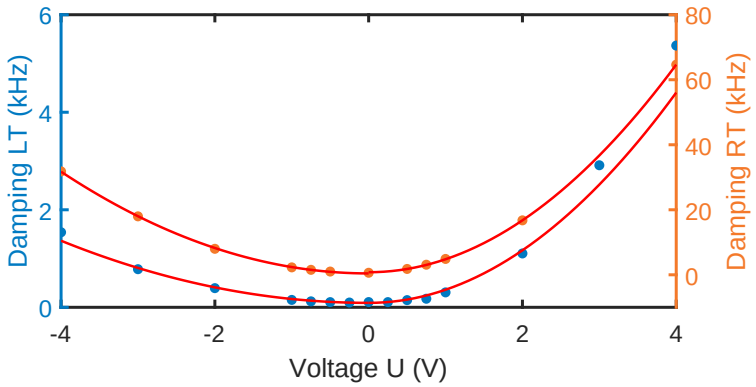

Figure 9.2: Dissipation as a function of dc voltage at low (5 K, blue dots) and room (orange) temperature. A fit similar to Eq. 9.1 is shown as red lines. The data was recorded on an ip mode of sample H.

similar to Eq. 9.1 to the data, yielding the coefficients

$$c_{\Gamma-}^{\mathrm{ip,RT}} = 2.0\,\mathrm{kHz\,V^{-2}}, \qquad c_{\Gamma+}^{\mathrm{ip,RT}} = 4.0\,\mathrm{kHz\,V^{-2}},$$
$$c_{\Gamma-}^{\mathrm{ip,LT}} = 0.1\,\mathrm{kHz\,V^{-2}}, \qquad c_{\Gamma+}^{\mathrm{ip,LT}} = 0.3\,\mathrm{kHz\,V^{-2}}.$$

Positive voltages increase the damping more than twice as much as negative voltages. By sweeping the voltage from 0 V to 4 V, the damping increases from $\Gamma = 1\,\mathrm{kHz}$ ($Q = 25\,000$) to 64 kHz (250) at RT and from 0.1 kHz (152 000) to 5.4 kHz (3000) at LT. This suggests that our SiC is really affected by dielectric damping. Rieger et al.[63] report a value of $c_\Gamma = 5.2\,\mathrm{Hz\,V^{-2}}$ for a SiN resonator at RT, which is nearly two orders of magnitude lower than our values. Again, this comparison has to be treated with some care as already mentioned previously.

For dc voltages beyond ± 8 V, our longest string resonators are displaced to such an extent that they touch the electrodes and stick to them permanently, as shown in Fig. 9.2. Shorter strings exhibit a higher stress and smaller displacements and are therefore less prone to stick to the electrodes. To this end, we limit ourselves to dc voltages between ± 8 V in all our experiments.

9.2 Coupling of Two Mechanical Modes

The dielectric tuning allows us to tune the frequency of the oop and ip modes in different directions and, therefore, into resonance. Then, these modes can couple to each other and exchange energy, leading to the characteristic avoided crossing as introduced in Sec. 2.4.1. Figure 9.4 summarizes how we measure and extract the frequency splitting from an avoided crossing. First, we measure multiple VNA

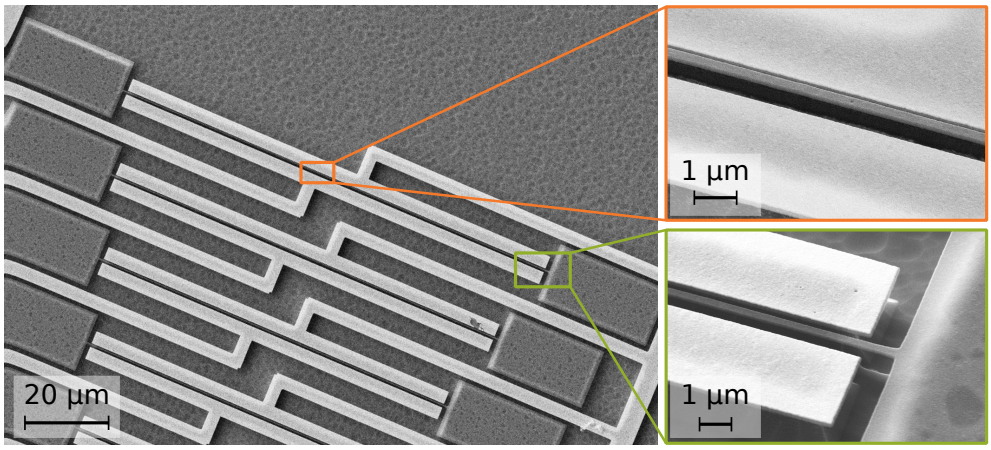

Figure 9.3: SEM image of string resonators with adjacent electrodes. After applying a voltage of more than 10 V the string touched the electrode and stuck to it.

sweeps at different voltages and join them to one color map (Fig. 9.4,left image). Second, we extract the resonance frequencies of the two branches, as indicated by the green and orange dots (middle image). Peaks with an insufficient signal-to-noise ratio (SNR) are excluded automatically.[b] Lastly, we fit the model of the avoided crossing[73] (two coupled harmonic oscillators) to the extracted frequencies and determine the frequency splitting (right image).

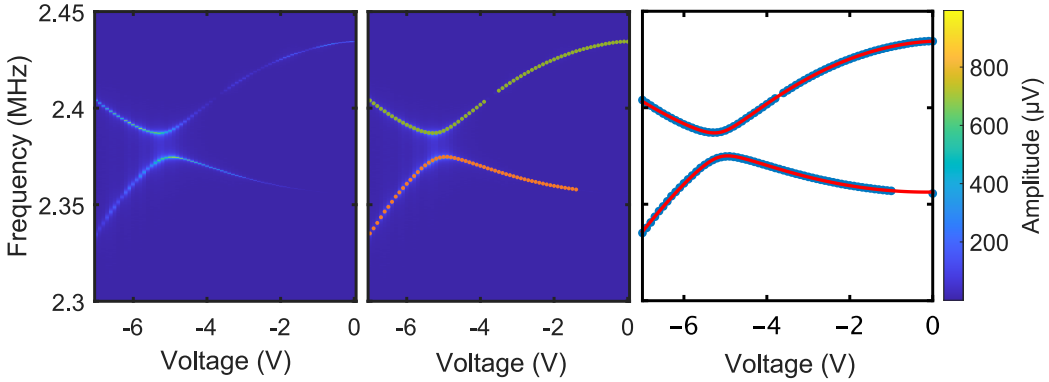

Figure 9.4: Process flow of the determination of the frequency splitting of an avoided crossing. Left image: Several VNA sweeps are combined to one color map. Middle: Extraction of the frequencies of the two modes. Right: Fitting of the data with the avoided crossing model. This measurement was recorded on a 100 µm string of sample G at 90 K

[b]The automatic exclusion of peaks works as follows: The mean amplitude of the whole color plot is taken as the noise level. Peaks that are smaller than three times this noise level are excluded.

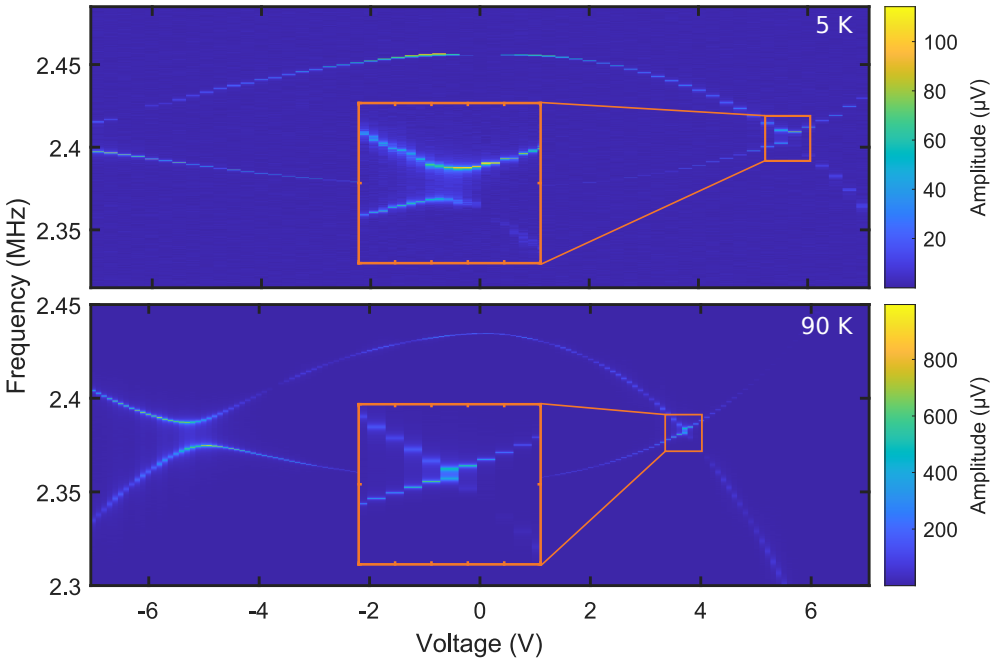

Figure 9.5: Resonator amplitude in volts as a function of frequency and applied dc voltage recorded at 5 K (top) and 90 K (bottom). The data was recorded on a 100 µm string of sample G.

In Fig. 9.4 we limited ourselves to negative voltages. Taking also the positive voltages into account reveals a second avoided crossing as shown in Fig. 9.5. It features, however, a noticeably smaller frequency splitting. For a temperature of 90 K, the frequency splitting is $\Gamma_{c-} = 12.7\,\text{kHz}$ and $\Gamma_{c+} = 2.4\,\text{kHz}$ at negative and positive voltages, respectively, which corresponds to a difference of a factor of five. Note that this behavior is perfectly reproducible and does not depend on the direction of the voltage sweep. Again, we can see the asymmetric frequency tuning discussed in Sec. 9.1.

We also want to examine the temperature dependence of the avoided crossing. For that we vary the temperature between 5 K and 90 K (both are plotted in Fig. 9.5) and extract the frequency splitting for the avoided crossings at negative and positive voltages. A summary of the resulting values can be found in Tab. 9.1. For higher temperatures, the center of the avoided crossings moves towards lower voltages. While the left avoided crossing at negative voltages is not within the accessible voltage range at 5 K (see Fig. 9.5 (top)), it is well resolved at 90 K (see Fig. 9.5 (bottom)). Furthermore, we find that lower temperatures lead to a slightly wider frequency splitting. For example, the left avoided crossing decreases from 15.0 kHz at 30 K to 12.7 kHz at 90 K.

Table 9.1: Frequency splitting of the avoided crossing at negative (Γ_{c-}) and positive (Γ_{c+}) voltages. Missing values (–) are either caused by a not perfectly converging fit or because the avoided crossing is not withing the accessible voltage range. Italic values are not very reliable. The data was recorded on a 100 µm string of sample G.

Temperature (K)	Γ_{c-} (kHz)	Γ_{c+} (kHz)
5	–	6.0
20	*15.1*	5.6
30	15.0	2.7
40	13.9	–
60	–	3.2
90	12.7	*2.4*
RT	–	–

9.3 Conclusion

In this chapter, we successfully implemented the dielectric actuation scheme for SiC. We find that a dc voltage sweep leads to an asymmetric frequency and dielectric tuning, which seems much stronger than in SiN. To keep the quality factor as high as possible, it is beneficial to tune towards negative instead of positive voltages. Further, the temperature dependence of the avoided crossing is analyzed, exhibiting that higher temperatures decrease the frequency splitting. Again, we find an asymmetric behavior, where the frequency splitting of the avoided crossing at negative is bigger than at positive voltages. This behavior as well as the frequency and dissipation tuning are subject to further investigation.

10

Outlook and Summary

This work investigates high Q nanomechanical string resonators fabricated from crystalline 3C-SiC(111). In order to harness the full potential of this material, we determine two growth dependent material parameters: The Young's modulus and the tensile stress. Due to the high tensile stress, SiC string resonators offer exceptional quality factors at room and low temperatures. We measure a constant loss angle over a broad frequency range with the help of a new dissipation model developed by Ignacio Wilson-Rae.

Since SiC has not been used in our group before, we first develop a top-down nanofabrication process. The most challenging part of the process was the release of the final resonator. The best and most reliable results are achieved with our new isotropic two step ICP-RIE process.[a] A Fabry-Pérot interferometer combined with piezo actuation is used to characterize the fabricated sample. We measure exceptional quality factors of around 400 000 at room temperature without utilizing stress engineering or phononic bandgaps.
Because the Young's modulus and the tensile stress depend on growth parameters, we could not rely on literature values. To this end, we developed a new method to determine the Young's modulus by analyzing the eigenmode spectrum of our resonators. Consequently, it is susceptible to the orientation and stress of the resonator's material. For our SiC(111), we find a Young's modulus of 400 GPa, which is, according to our calculations, valid for all directions in the (111)-plane. Knowing the exact Young's modulus allows us to extract the tensile stress for individual string resonators. It turns out that the stress depends on the length of the resonator, following approximately $\sigma(L) \propto L^{-1}$. We find this effect for SiC, SiN,

[a] Recently, we developed an even better three step ICP-IRE process presented in Felix David's master thesis [177].

as well as InGaP, suggesting that this effect is material independent. With the help of an elastic model, we can replicate our findings and predict which geometric changes affect the resonator's stress, paving the way for stress engineering.
We measure the quality factor as a function of mode number and resonator length. This data is fit with an advanced dissipation dilution model developed by Ignacio Wilson-Rae, which offers unprecedented precision for the extracted dilution factor. We find a constant loss angle over a range of 80 MHz, indicating that it is frequency independent.
Cooling the SiC resonators to low temperatures boosts the quality factor up to 3.5×10^6. Temperature dependent measurements of the dissipation and frequency indicate thermally activated defects at 180 K. For both SiC and InGaP we find a hysteresis-like behavior at around 23 K that vanishes for thermalization times of multiple days. Thermally activated defects could again be the origin of this behavior. However, further investigations are needed to understand the underlying physics. This includes, for instance, cooling the system to millikelvin, where we expect resonant absorption of phonons.
Lastly, we implement the dielectric driving scheme with SiC string resonators, allowing us to tune the frequency and dissipation of the mechanical modes. Both show an asymmetric behavior, which is not found in SiN. We also find that the dielectric damping in SiC is around two orders of magnitude stronger than in SiN. Additionally, we analyzed the temperature dependence of the avoided crossing, exhibiting that lower temperatures lead to a stronger coupling.

In collaboration with the group of Artur Erbe and Georgy Astakhov from the Helmholtz-Zentrum Dresden-Rossendorf, we plan to analyze ion-induced defects in the resonator's material. Characterization before and after the implantation should reveal any radiation damage or effects of the defects on the mechanical quality factor. Additionally, this couples the motion of the string resonator to the defects.
Further, we plan to combine the exceptional quality factor of SiC with a newly developed 3D Cavity from Anh Tuan Le,[178] allowing for optomechanical experiments. This is especially interesting in combination with aluminum electrodes, as we did in our collaboration with Eddy Collin.[179] Cooling to millikelvin would provide us with a superconducting cavity and electrodes.
My colleague Jana Ochs[119] presented a plethora of interesting nonlinear phenomena in her thesis. However, she was slightly hampered by the inability to resolve the thermal motion of the SiN resonator. This problem would be solved by switching to SiC because we can easily resolve the thermal motion. Vincent Blavy started already to join both projects during his internship in our group.[180]

Appendices

A

Samples, Wafers and Material Parameters

Table A.1 and A.2 list all samples and wafers that are used in this work. Table A.3 summarizes the growth parameters of the wafers employed in Chap. 5 and 6, stating the thickness of the device layer, sacrificial layer (if the system has one), substrate, and the corresponding supplier. The two SiN wafers were grown by Low Pressure Chemical Vapor Deposition (LPCVD), the SiC in a two-stage Chemical Vapor Deposition process, and the $In_{1-x}Ga_xP$ using Metal-Organic Chemical Vapor Deposition (MOCVD). All material parameters employed in the theoretical calculations are listed in Tab. A.4.

Table A.1: Sample name, material (wafer number), label (backside of the sample) and person that fabricated the chip.

	Material	Label	Electrodes	Fabricated by
Sample A	3C-SiC (W1)	WC100	No	me
Sample B	3C-SiC (W1)	VD3	No	F. David
Sample C	InGaP		No	M. Bückle
Sample D	SiN-FS	GD1	No	me
Sample E	SiN-Si		No	me
Sample F	3C-SiC (W5)	WA100	Yes	me
Sample G	3C-SiC (W5)	N2C10	Yes	me
Sample H	3C-SiC (W5)	N2C11	Yes	me

Table A.2: Basic parameters of the SiC wafers. All non SiC wafers are listed in Tab. A.3 The thickness of most wafers is determined via ellipsometry.

	Device layer	Substrate	Doping	ID	Chapter
W1	110 nm 3C-SiC(111)	1 mm Si	doped	18C1-008	5, 6, 7
W2	210 nm 3C-SiC(111)	1 mm Si	doped	19C1-017	
W3	210 nm 3C-SiC(111)	1 mm Si	doped	19C1-018	
W4	*210 nm*[a] 3C-SiC(100)	1 mm Si	doped	19C1-173	
W5	120 nm 3C-SiC(111)	1 mm Si	nid	21C1-012	9, 8
W6	30 nm 3C-SiC(111)	1 mm Si	nid	21C1-015	
W7	90 nm 3C-SiC(111)	1 mm Si	nid	21C1-020	

[a]This thickness was never confirmed via ellipsometry, therefore, we do not have reliable data about the thickness.

Table A.3: Basic parameters of the non SiC wafers on which the string resonators were fabricated that are presented in Chap. 5 and 6. All SiC wafers are listed in Tab. A.2. Adapted from Ref. [39].

	resonator / device layer	sacrificial layer	substrate	source
SiC (W1)	110 nm 3C-SiC	—	Si(111)	NOVASiC
SiN-FS	100 nm SiN	—	SiO_2	HSG-IMIT
SiN-Si	100 nm SiN	400 nm SiO_2	Si(100)	HSG-IMIT
$In_{1-x}Ga_xP$	100 nm $In_{0.415}Ga_{0.585}P$	1000 nm $Al_{0.85}Ga_{0.15}As$	GaAs	CNRS

Table A.4: Young's modulus, shear modulus and density of the materials used within this work. All shear mouduli where calculated via $G = \frac{E}{2(1+\nu)}$. Adapted from Ref. [39].

	Young's modulus E (GPa)	Shear modulus G (GPa)	Poisson's ratio ν	density ρ (g/cm^3)
SiC	400(36)[a]	184	0.14[149]	3.2(1)[78,152]
Si	160[149]	66	0.22[149]	2.4[149]
SiN-FS	254(26)[a]	104	0.25[149]	3.1(1)[149–151]
SiN-Si	198(21)[a]	104	0.25[149]	3.1(1)[149–151]
SiO_2	73[149]	31	0.17[149]	2.2[149]
$In_{1-x}Ga_xP$	108(7)[a]	47	0.32[153b]	4.4[153]
GaAs	75[149]	29	0.31[153]	5.3[149]

[a]Measured by us, as demonstrated in Chap. 5.

[b]Calculated with $\nu = \frac{c_{12}}{c_{11}+c_{12}}$ where c_{ij} are the elastic constants.

B

Process Parameters

B.1 Harp of Strings

Preparation

Process step	Equipment	Details
Labelling	Diamond scratcher	mark crystal direction label sample
Cleaning	Ultrasonic bath & acetone Ultrasonic bath & IPA	lowest intensity, 2 min lowest intensity, 2 min

Electron Beam Lithography

Process step	Equipment	Details
Spin coat	Spincoater & PMMA 950k A6	Ramp up: 1 s at 800 rpm Spin: 30 s at 5000 rpm
Softbake	Hot plate	90 s at 180 °C
Lithography	Zeiss Crossbeam	Aperture: 20 µm Acceleration voltage: 10 kV Working distance: 8.6 mm Dose clamping pad: 170 µC cm^{-2} Dose strings: 255 µC cm^{-2} Aperture: 20 µm Aperture: 20 µm
Develop	MIBK:IPA (1:3) IPA	50 s at least 1 min

Evaporation of the Etch Mask

Process step	Equipment	Details
Evaporation	E-beam evaporator or thermal evaporator	Chromium: 30 nm at 1 Å s^{-1}
Lift-off	Ultrasonic bath & acetone Ultrasonic bath & IPA	lowest intensity, 10 min lowest intensity, 2 min

Releasing the resonator

Process step	Equipment	Details
SF_6 Etch	ICP-RIE	Time: 150 s ICP-Power: 350 W RF-Power: 65 W SF_6 flow: 2 sccm Ar flow: 4 sccm Pressure: 2 mTorr Temperature: 10 °C
Ar mill	ICP-RIE	Time: 45 s ICP-Power: 800 W RF-Power: 70 W Ar flow: 30 sccm Pressure: 3 mTorr Temperature: 10 °C
Removing etch mask	IPA (60 °C) DI water Chromium Etchant DI water IPA	dip in IPA dip in 2 consecutive baths 40 s dip in 2 consecutive baths dip in IPA
Drying	Critical point dryer	Exchange Gas: CO_2

B.2 Strings with Adjacent Electrodes

Preparation

Process step	Equipment	Details
Labelling	Diamond scratcher	mark crystal direction label sample
Cleaning	Ultrasonic bath & acetone	lowest intensity, 2 min
	Ultrasonic bath & IPA	lowest intensity, 2 min

Electron Beam Lithography (Electrodes)

Process step	Equipment	Details
Spin coat	Spincoater & PMMA 950k A6	Ramp up: 1 s at 800 rpm Spin: 30 s at 5000 rpm
Softbake	Hot plate	90 s at 180 °C
Lithography	Zeiss Crossbeam	Acceleration voltage: 10 kV Working distance: 8.6 mm Aperture electrodes: 20 µm Dose electrodes: 170 µC cm^{-2} Aperture bond pads: 60 µm Dose bond pads: 190 µC cm^{-2}
Develop	MIBK:IPA (1:3) IPA	50 s at least 1 min

Evaporation of the Electrodes

Process step	Equipment	Details
Evaporation	E-beam evaporator or thermal evaporator	Cr: 5 nm at 1 Å s^{-1} Au: 50 nm at 1 Å s^{-1} Cr: 5 nm at 1 Å s^{-1}
Lift-off	Ultrasonic bath & acetone Ultrasonic bath & IPA	lowest intensity, 10 min lowest intensity, 2 min

Electron Beam Lithography (Strings)

Process step	Equipment	Details
Spin coat	Spincoater & PMMA 950k A6	Ramp up: 1 s at 800 rpm Spin: 30 s at 5000 rpm
Softbake	Hot plate	90 s at 180 °C
Lithography	Zeiss Crossbeam	Aperture: 20 µm Acceleration voltage: 10 kV Working distance: 8.6 mm Dose clamping pad: 170 µC cm^{-2} Dose strings: 255 µC cm^{-2} Aperture: 20 µm
Develop	MIBK:IPA (1:3) IPA	50 s at least 1 min

Evaporation of the Etch Mask (Strings)

Process step	Equipment	Details
Evaporation	E-beam evaporator or thermal evaporator	Cr: 30 nm at 1 Å s^{-1}
Lift-off	Ultrasonic bath & acetone	lowest intensity, 10 min
	Ultrasonic bath & IPA	lowest intensity, 2 min

Releasing the resonator

Process step	Equipment	Details
SF_6 Etch	ICP-RIE	Time: 150 s ICP-Power: 350 W RF-Power: 65 W SF_6 flow: 2 sccm Ar flow: 4 sccm Pressure: 2 mTorr Temperature: 10 °C
Ar mill	ICP-RIE	Time: 45 s ICP-Power: 800 W RF-Power: 70 W Ar flow: 30 sccm Pressure: 3 mTorr Temperature: 10 °C
Removing etch mask	IPA (60 °C)	dip in IPA
	DI water	dip in 2 consecutive baths
	Chromium Etchant	40 s
	DI water	dip in 2 consecutive baths
	IPA	dip in IPA
Drying	Critical point dryer	Exchange Gas: CO_2

C

Measuring Ring-Downs with VNA and SA

Here, we describe a measurement scheme to perform a ring-down with a vector network analyzer (VNA) and a spectrum analyzer (SA). For every ring down measurement, we have to determine the resonance frequency of the corresponding mode, drive at this frequency, switch off the drive, and measure the energy decay. As we utilize a VNA and SA for that, we have to use the wiring presented in Fig. 4.2. If the signal-to-noise ratio (SNR) is sufficient, the resonance frequency is extracted via the thermal motion, measured with the SA. Otherwise, the VNA has to be used. Because we are only interested in the resonance frequency (and not the quality factor), we are able to use a relatively high bandwidth of around 100 Hz - 1000 Hz, which allows for a quick extraction of the resonance frequency while completely underestimating the quality factor. Next, we use the VNA to drive exactly at the extracted frequency with a 1 Hz bandwidth and 8001 points. In order to get a clean drive spectrum (i.e., a single sharp peak at the drive frequency), it is crucial to stick to those parameters. Otherwise, parasitic drive peaks can arise, disturbing the measurement. Now we are ready to perform the actual measurement. For that, we turn on the output of the VNA with the previously mentioned settings. Then we start the time resolved SA measurement[a] and switch off the power shortly after, which leads to the characteristic energy decay. By fitting Eq. (2.8) to the recorded data, we can extract the ring-down time τ and calculate the quality factor.

[a]The SA needs to be in *zero span mode*. Also, a sufficient ring-up time of at least 3 s is important.

D

Comparison of Euler-Bernoulli Boundary Conditions

Figure. D.1 shows a comparison of Euler-Bernoulli beam theory with clamped and simply supported boundary conditions. We find that they follow exactly the same course but yield slightly different stress values as can be seen in Fig. D.2. Note that our elastic model from Chap. 6 is still fitting very well.

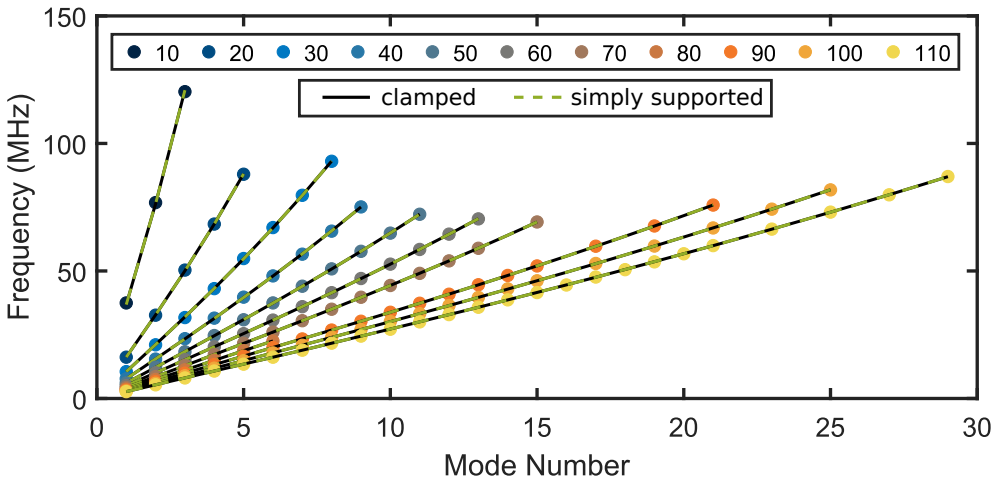

Figure D.1: Eigenfrequencies of the oop modes as a function of the mode number. The measured frequencies of resonators of different length are shown as colored dots. The solid and dashed line corresponds to a fit of the Euler-Bernoulli beam theory with clamped and simply supported boundary conditions, respectively. The data was recorded on sample A.

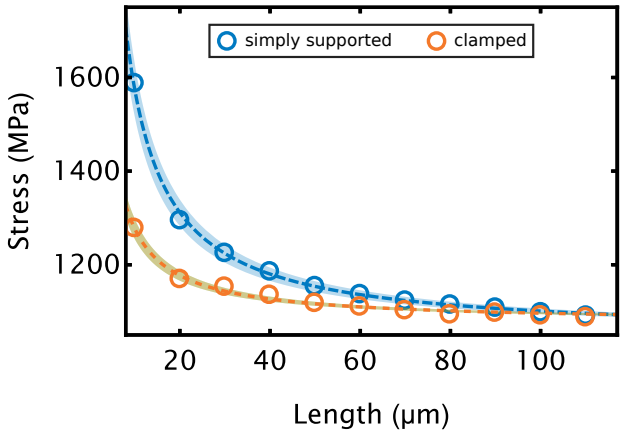

Figure D.2: Stress as a function of resonator length. The stress values are determined by fitting Euler-Bernoulli beam theory with simply supported (blue dots) and clamped boundary conditions (orange) to the data (see Fig. D.1). Fits of Eq. (6.9) are included as solid lines. The shaded areas indicate the uncertainty resulting from measurement errors of the pedestal height h_0 and undercut a_{uc}. The data was recorded on sample A.

E

Even Mode Numbers of the Loss Dilution Model

Figure E.1 shows the inverse dilution factor as a function of the dimensionless parameter $\kappa_0 L$ for even mode numbers.

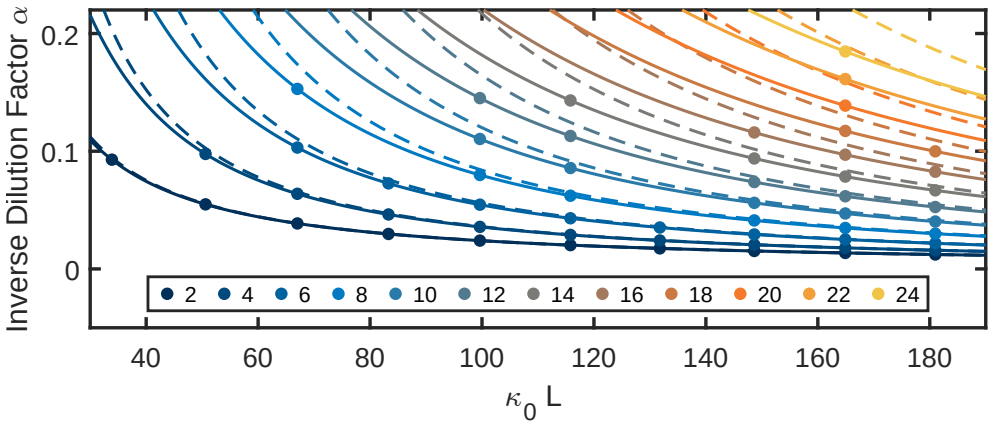

Figure E.1: Inverse dilution factor as a function of the dimensionless parameter $\kappa_0 L$. The solid and dashed lines correspond to a loss dilution model assuming and not assuming the string approximation, respectively. Different colors symbolize different modes. For the sake of visibility, we omit odd mode numbers at this point, but they are shown in Fig. 7.2. Colored dots depict the parameters $\kappa_0 L$ and n of our resonators.

F

Comparison of Multiple Cooldowns

As explained in Chap. 8, the positioners drift during the cooldown of the cryostat. Here, we compare the frequency and damping acquired during three different cooldowns. While the behavior of the damping is nearly identical for the three runs, the course of the frequency changes significantly. Note that the plot limits are identical for all three images. Significantly less drifting and reproducible results can be achieved with an internal heater.

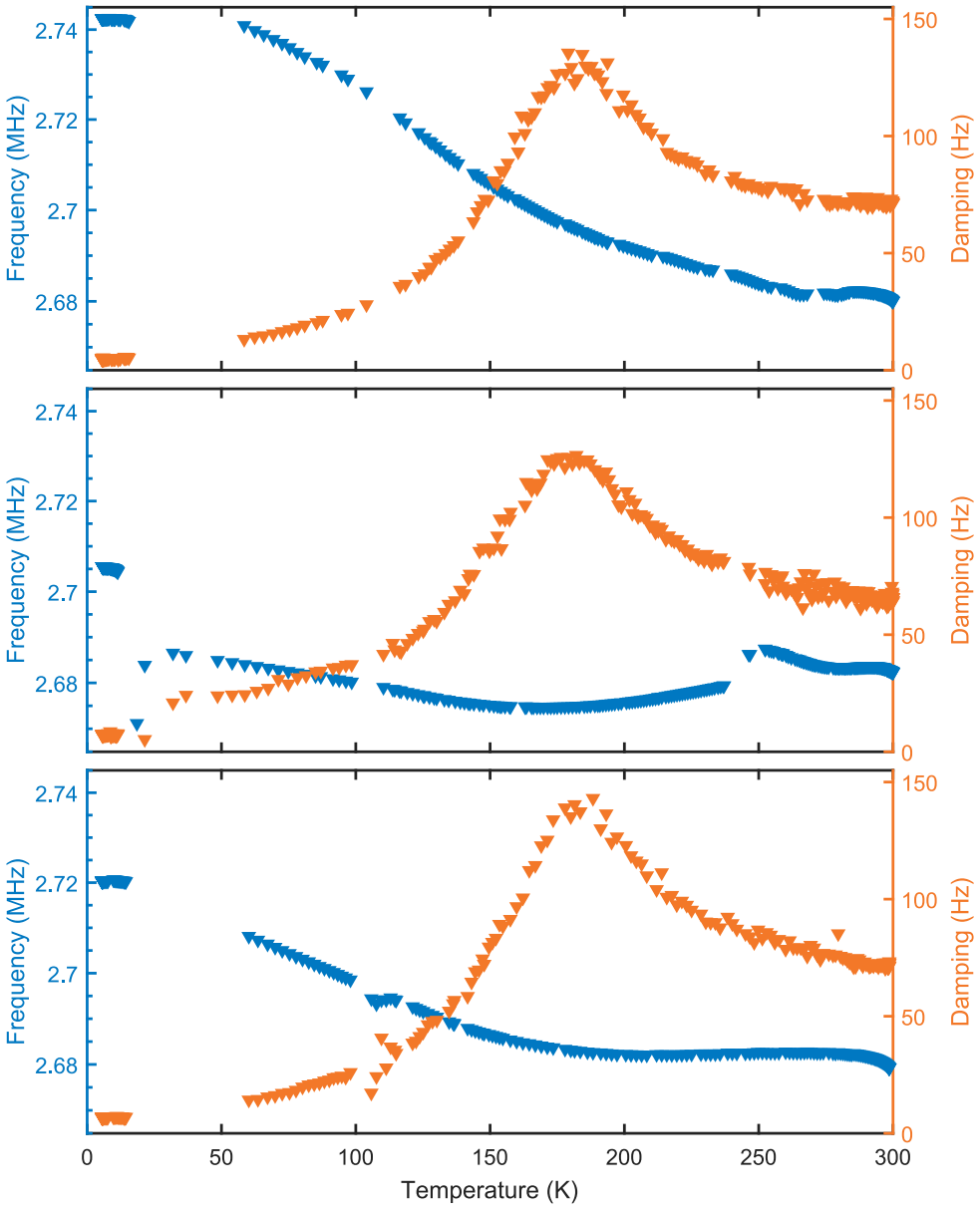

Figure F.1: Measured frequency and damping as a function of temperature for three different cooldowns. All measurements are performed in the same setup and on the same sample. The data was recorded on sample A.

G

Thermal Conductivity SiC

The thermal conductivity of 3C-SiC follows

$$K = A\,T^{-N} \tag{G.1}$$

in the temperature range shown in Fig. G.1. Fitting Eq. (G.1) to the data[78] presented in Fig. G.1, yields the parameter $N = 1.8$.

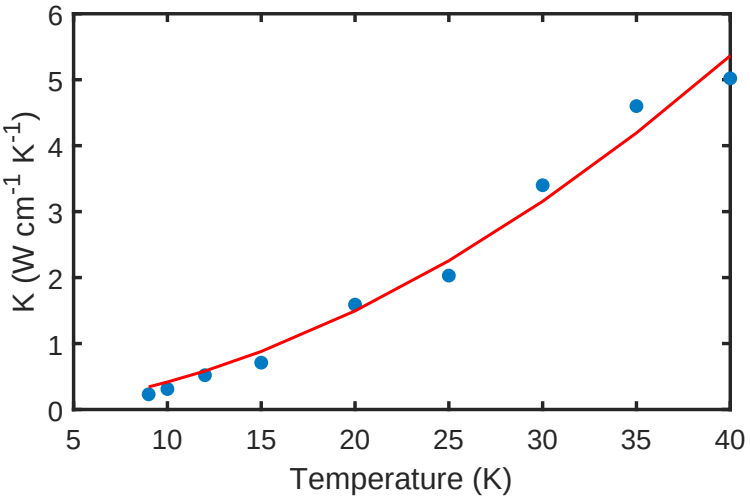

Figure G.1: Thermal conductivity K of 3C-SiC in the range between 9 K and 40 K. The blue data points and the red line correspond to data points takenn from Ref. [78] and a the fit of Eq. (G.1).

H

Laser Heating at Cryogenic Temperatures

To show a laser heated string resonator at low temperatures, we combine a high laser power with a stroboscopic measurement. First, the sample is radiated for a while with an initial laser power of around 12 mW. Then, the laser is blocked and just unblocked to take several fast measurements (see Fig. H.1 fist five hours). Clearly, the damping decreases over time until it stabilizes at around 10 Hz, indicating that the sample is now thermalized. Parallel to that, the frequency increases. Comparing this to the measurements in Chap. 8 suggests a raise in the string's temperature. After five hours, we switch back to a continuous measurement (still a laser power of 12 mW), leading to an increase in temperature. Three hours later (i.e. eight

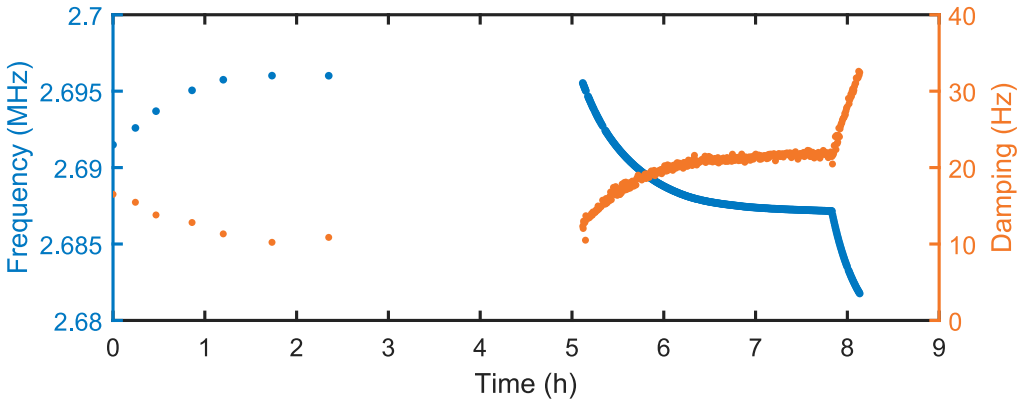

Figure H.1: Stroboscopic measurement of the frequency and damping of a 110 µm SiC string at low temperatures. At times where no data is shown, the laser is blocked to allow the sample too cool down. After five hours the laser is turned on permanently with a power of 12 mW. After eight hours the laser power is increased to 40 mW.

hours in Fig.H.1) the laser power is raised to approximately 40 mW). Again the string's temperature is increasing, as can be seen from the course of the frequency and damping.

I

Supporting Calculations: Calibration with Thermal Amplitude

These calculations are based on personal communication with Sophia and Jonathan Rau.

In Sec. 4.3 we follow the calculations of Hauer et al. [42] to calibrate our setup via a thermal motion. They quote Ref. [181] for the calculations of

$$\int_0^\infty \frac{1}{(\omega_0^2-\omega^2)^2+(\Gamma\omega)^2}d\omega = \frac{\pi}{2\Gamma\omega_0^2}. \tag{I.1}$$

While the result is correct, the calculations are partially questionable. Here, we try to provide a mathematically more accurate calculation of Eq. (I.1). For that we assume $2\omega_0 > \Gamma$, which is valid for high Q resonators. First, we notice

$$\begin{aligned}\int_{-\infty}^\infty \frac{1}{(\omega_0^2-\omega^2)^2+(\Gamma\omega)^2}d\omega &= \int_{-\infty}^\infty \frac{1}{(\omega^2-\Gamma\omega i-\omega_0^2)(\omega^2+\Gamma\omega i-\omega_0^2)}d\omega \\ &= \int_{-\infty}^\infty \frac{1}{\left(\omega-\frac{s+\Gamma i}{2}\right)\left(\omega-\frac{-s+\Gamma i}{2}\right)\left(\omega-\frac{s-\Gamma i}{2}\right)\left(\omega-\frac{-s-\Gamma i}{2}\right)}d\omega,\end{aligned}$$

with $s \coloneqq \sqrt{4\omega_0^2-\Gamma^2}$. Applying the residue theorem[182] known from complex

analysis leads to

$$
\begin{aligned}
&\int_{-\infty}^{\infty} \frac{1}{(\omega_0^2-\omega^2)^2+(\Gamma\omega)^2} d\omega \\
&\qquad = \left. \frac{2\pi i}{\left(\omega-\frac{-s+\Gamma i}{2}\right)\left(\omega-\frac{s-\Gamma i}{2}\right)\left(\omega-\frac{-s-\Gamma i}{2}\right)} \right|_{\omega=\frac{s+\Gamma i}{2}} \\
&\qquad\quad + \left. \frac{2\pi i}{\left(\omega-\frac{s+\Gamma i}{2}\right)\left(\omega-\frac{s-\Gamma i}{2}\right)\left(\omega-\frac{-s-\Gamma i}{2}\right)} \right|_{\omega=\frac{-s+\Gamma i}{2}} \\
&\qquad = \frac{2\pi i}{s\Gamma i(s+\Gamma i)} + \frac{2\pi i}{-s(-s+\Gamma i)\Gamma i} \\
&\qquad = \frac{2\pi(-s+\Gamma i)}{s\Gamma(s+\Gamma i)(-s+\Gamma i)} - \frac{2\pi(s+\Gamma i)}{s\Gamma(s+\Gamma i)(-s+\Gamma i)} \\
&\qquad = \frac{4\pi s}{s\Gamma(\Gamma^2+s^2)} \\
&\qquad = \frac{\pi}{\Gamma\omega_0^2}.
\end{aligned}
$$

Due to symmetry reasons, we get

$$
\int_0^{\infty} \frac{1}{(\omega_0^2-\omega^2)^2+(\Gamma\omega)^2} d\omega = \frac{\pi}{2\Gamma\omega_0^2},
$$

which is identical to the result stated in Ref. [181].

Bibliography

[1] J. J. Berzelius, "Untersuchungen über die Flussspathsäure und deren merkwürdigsten Verbindungen," Annalen der Physik **77**, 169–230 (1824).

[2] N. Jepps and T. Page, "Polytypic transformations in silicon carbide," Progress in crystal growth and characterization **7**, 259–307 (1983).

[3] X. Guo, Q. Xun, Z. Li, and S. Du, "Silicon carbide converters and MEMS devices for high-temperature power electronics: A critical review," Micromachines **10**, 406 (2019).

[4] R. Bogue, "MEMS sensors: past, present and future," Sensor Review (2007).

[5] H. Morkoc, S. Strite, G. Gao, M. Lin, B. Sverdlov, and M. Burns, "Large-band-gap SiC, III-V nitride, and II-VI ZnSe-based semiconductor device technologies," Journal of Applied physics **76**, 1363–1398 (1994).

[6] V. Cimalla, J. Pezoldt, and O. Ambacher, "Group III nitride and SiC based MEMS and NEMS: materials properties, technology and applications," Journal of Physics D: Applied Physics **40**, 6386 (2007).

[7] M. Mehregany, C. A. Zorman, N. Rajan, and C. H. Wu, "Silicon carbide MEMS for harsh environments," Proceedings of the IEEE **86**, 1594–1609 (1998).

[8] D. G. Senesky, B. Jamshidi, K. B. Cheng, and A. P. Pisano, "Harsh environment silicon carbide sensors for health and performance monitoring of aerospace systems: A review," IEEE Sensors Journal **9**, 1472–1478 (2009).

[9] D. Garrido-Diez and I. Baraia, "Review of wide bandgap materials and their impact in new power devices," in 2017 IEEE International work-

shop of electronics, control, measurement, signals and their Application to mechatronics (ECMSM) (IEEE, 2017), pp. 1–6.

[10] N. Marsi, B. Y. Majlis, A. A. Hamzah, and F. Mohd-Yasin, "Development of high temperature resistant of 500° C employing silicon carbide (3C-SiC) based MEMS pressure sensor," Microsystem Technologies **21**, 319–330 (2015).

[11] K. Ekinci, X. Huang, and M. Roukes, "Ultrasensitive nanoelectromechanical mass detection," Applied Physics Letters **84**, 4469–4471 (2004).

[12] A. Naik, M. Hanay, W. Hiebert, X. Feng, and M. Roukes, "Towards single-molecule nanomechanical mass spectrometry," Nature nanotechnology **4**, 445–450 (2009).

[13] Y. Yang, C. Callegari, X. Feng, K. Ekinci, and M. Roukes, "Zeptogram-scale nanomechanical mass sensing," Nano letters **6**, 583–586 (2006).

[14] T. P. Burg, M. Godin, S. M. Knudsen, W. Shen, G. Carlson, J. S. Foster, K. Babcock, and S. R. Manalis, "Weighing of biomolecules, single cells and single nanoparticles in fluid," nature **446**, 1066 (2007).

[15] M. Li, H. X. Tang, and M. L. Roukes, "Ultra-sensitive NEMS-based cantilevers for sensing, scanned probe and very high-frequency applications," Nature nanotechnology **2**, 114–120 (2007).

[16] J. Chaste, A. Eichler, J. Moser, G. Ceballos, R. Rurali, and A. Bachtold, "A nanomechanical mass sensor with yoctogram resolution," Nature nanotechnology **7**, 301–304 (2012).

[17] T. Stowe, K. Yasumura, T. Kenny, D. Botkin, K. Wago, and D. Rugar, "Attonewton force detection using ultrathin silicon cantilevers," Applied Physics Letters **71**, 288–290 (1997).

[18] J. Moser, J. Güttinger, A. Eichler, M. J. Esplandiu, D. Liu, M. Dykman, and A. Bachtold, "Ultrasensitive force detection with a nanotube mechanical resonator," Nature nanotechnology **8**, 493–496 (2013).

[19] P. Kim, B. Hauer, C. Doolin, F. Souris, and J. Davis, "Approaching the standard quantum limit of mechanical torque sensing," Nature communications **7**, 1–6 (2016).

[20] M. Wu, A. C. Hryciw, C. Healey, D. P. Lake, H. Jayakumar, M. R. Freeman, J. P. Davis, and P. E. Barclay, "Dissipative and dispersive optomechanics in a nanocavity torque sensor," Physical Review X **4**, 021052 (2014).

[21] T. Faust, P. Krenn, S. Manus, J. P. Kotthaus, and E. M. Weig, "Microwave cavity-enhanced transduction for plug and play nanomechanics at room temperature," Nature communications **3**, 728 (2012).

[22] J. S. Ochs, M. Seitner, M. I. Dykman, and E. M. Weig, "Amplification and spectral evidence of squeezing in the response of a strongly driven nanoresonator to a probe field," Physical Review A **103**, 013506 (2021).

[23] M. J. Seitner, H. Ribeiro, J. Kölbl, T. Faust, J. P. Kotthaus, and E. M. Weig, "Classical Stückelberg interferometry of a nanomechanical two-mode system," Physical Review B **94**, 245406 (2016).

[24] S. S. Verbridge, J. M. Parpia, R. B. Reichenbach, L. M. Bellan, and H. G. Craighead, "High quality factor resonance at room temperature with nanostrings under high tensile stress," Journal of Applied Physics **99**, 124304 (2006).

[25] A. H. Ghadimi, D. J. Wilson, and T. J. Kippenberg, "Radiation and internal loss engineering of high-stress silicon nitride nanobeams," Nano letters **17**, 3501–3505 (2017).

[26] A. H. Ghadimi, S. A. Fedorov, N. J. Engelsen, M. J. Bereyhi, R. Schilling, D. J. Wilson, and T. J. Kippenberg, "Elastic strain engineering for ultralow mechanical dissipation," Science **360**, 764–768 (2018).

[27] E. Romero, V. M. Valenzuela, A. R. Kermany, L. Sementilli, F. Iacopi, and W. P. Bowen, "Engineering the dissipation of crystalline micromechanical resonators," Physical Review Applied **13**, 044007 (2020).

[28] A. R. Kermany, G. Brawley, N. Mishra, E. Sheridan, W. P. Bowen, and F. Iacopi, "Microresonators with Q-factors over a million from highly stressed epitaxial silicon carbide on silicon," Applied Physics Letters **104**, 081901 (2014).

[29] K. Onomitsu, M. Mitsuhara, H. Yamamoto, and H. Yamaguchi, "Ultrahigh-Q micromechanical resonators by using epitaxially induced tensile strain in GaNAs," Applied Physics Express **6**, 111201 (2013).

[30] A. Beccari, D. Visani, S. Fedorov, M. Bereyhi, V. Boureau, N. Engelsen, and T. Kippenberg, "Strained crystalline nanomechanical resonators with quality factors above 10 billion," Nature Physics **18**, 436–441 (2022).

[31] K. Petersen, "Silicon as a mechanical material," Proceedings of the IEEE **70**, 420–457 (1982).

[32] Y. S. Klaß, J. Doster, M. Bückle, R. Braive, and E. M. Weig, "Determining Young's modulus via the eigenmode spectrum of a nanomechanical string resonator," Submitted manuscript, 1–6 (2022).

[33] S. Schmid, L. G. Villanueva, and M. L. Roukes, *Fundamentals of nanomechanical resonators*, Vol. 49 (Springer, 2016).

[34] M. Bückle, "Nanomechanical Systems Based on Tensile-Stressed Crystalline Indium Gallium Phosphide," PhD thesis at the Universität of Konstanz (2020).

[35] S. M. Han, H. Benaroya, and T. Wei, "Dynamics of transversely vibrating beams using four engineering theories," Journal of Sound and vibration **225**, 935–988 (1999).

[36] W. Weaver Jr, S. P. Timoshenko, and D. H. Young, *Vibration problems in engineering* (John Wiley & Sons, 1991).

[37] A. N. Cleland, *Foundations of nanomechanics: from solid-state theory to device applications* (Springer, Berlin, Heidelberg, 2003).

[38] W. S. Kurt Magnus Karl Popp, *Schwingungen: Physikalische Grundlagen und mathematische Behandlung von Schwingungen* (Springer Vieweg, Wiesbaden, 2013).

[39] M. Bückle, Y. S. Klaß, F. B. Nägele, R. Braive, and E. M. Weig, "Universal length dependence of tensile stress in nanomechanical string resonators," Physical Review Applied **15**, 034063 (2021).

[40] R. Traill-Nash and A. Collar, "The effects of shear flexibility and rotatory inertia on the bending vibrations of beams," The Quarterly Journal of Mechanics and Applied Mathematics **6**, 186–222 (1953).

[41] S. Schmid, C. Hierold, and A. Boisen, "Modeling the Kelvin polarization force actuation of micro-and nanomechanical systems," Journal of Applied Physics **107**, 054510 (2010).

[42] B. Hauer, C. Doolin, K. Beach, and J. Davis, "A general procedure for thermomechanical calibration of nano/micro-mechanical resonators," Annals of Physics **339**, 181–207 (2013).

[43] W. Nolting, *Grundkurs Theoretische Physik 1: Klassische Mechanik*, Vol. 10 (Springer, Berlin, Heidelberg, 2013).

[44] G. I. González and P. R. Saulson, "Brownian motion of a mass suspended by an anelastic wire," The Journal of the Acoustical Society of America **96**, 207–212 (1994).

[45] G. González, "Suspensions thermal noise in the LIGO gravitational wave detector," Classical and Quantum Gravity **17**, 4409 (2000).

[46] Q. P. Unterreithmeier, T. Faust, and J. P. Kotthaus, "Damping of nanomechanical resonators," Physical review letters **105**, 027205 (2010).

[47] P.-L. Yu, T. Purdy, and C. Regal, "Control of material damping in high-Q membrane microresonators," Physical review letters **108**, 083603 (2012).

[48] S. Schmid and C. Hierold, "Damping mechanisms of single-clamped and prestressed double-clamped resonant polymer microbeams," Journal of Applied Physics **104**, 093516 (2008).

[49] Y. S. Klaß, I. Wilson-Rae, and E. M. Weig, "Constancy of the undiluted inverse Q from the stress-diluted dissipation of crystalline nanomechanical resonators," Manuscript in preparation (2022).

[50] S. Fedorov, V. Sudhir, R. Schilling, H. Schütz, D. J. Wilson, and T. Kippenberg, "Evidence for structural damping in a high-stress silicon nitride nanobeam and its implications for quantum optomechanics," Physics Letters A **382**, 2251–2255 (2018).

[51] Q. P. Unterreithmeier, E. M. Weig, and J. P. Kotthaus, "Universal transduction scheme for nanomechanical systems based on dielectric forces," Nature **458**, 1001–1004 (2009).

[52] L. G. Villanueva and S. Schmid, "Evidence of surface loss as ubiquitous limiting damping mechanism in SiN micro-and nanomechanical resonators," Physical review letters **113**, 227201 (2014).

[53] A. Cleland and M. Roukes, "Fabrication of high frequency nanometer scale mechanical resonators from bulk Si crystals," Applied Physics Letters **69**, 2653–2655 (1996).

[54] D. Rugar and P. Grütter, "Mechanical parametric amplification and thermomechanical noise squeezing," Physical Review Letters **67**, 699 (1991).

[55] M. LaHaye, O. Buu, B. Camarota, and K. Schwab, "Approaching the quantum limit of a nanomechanical resonator," Science **304**, 74–77 (2004).

[56] L. Sekaric, D. Carr, S. Evoy, J. Parpia, and H. Craighead, "Nanomechanical resonant structures in silicon nitride: fabrication, operation and dissipation issues," Sensors and Actuators A: Physical **101**, 215–219 (2002).

[57] G. Sosale, K. Das, L. Fréchette, and S. Vengallatore, "Controlling damping and quality factors of silicon microcantilevers by selective metallization," Journal of Micromechanics and Microengineering **21**, 105010 (2011).

[58] M. J. Seitner, K. Gajo, and E. M. Weig, "Damping of metallized bilayer nanomechanical resonators at room temperature," Applied Physics Letters **105**, 213101 (2014).

[59] W. Demtröder, *Experimentalphysik 2: Elektrizität und Optik*, Springer-Lehrbuch (Springer Spektrum, 2013).

[60] J. Voldman, "Electrical forces for microscale cell manipulation," Annu. Rev. Biomed. Eng. **8**, 425–454 (2006).

[61] T. Hunt and R. Westervelt, "Dielectrophoresis tweezers for single cell manipulation," Biomedical microdevices **8**, 227–230 (2006).

[62] H. Li and R. Bashir, "Dielectrophoretic separation and manipulation of live and heat-treated cells of Listeria on microfabricated devices with interdigitated electrodes," Sensors and Actuators B: Chemical **86**, 215–221 (2002).

[63] J. Rieger, T. Faust, M. J. Seitner, J. P. Kotthaus, and E. M. Weig, "Frequency and Q factor control of nanomechanical resonators," Applied Physics Letters **101**, 103110 (2012).

[64] Y. S. Klaß, "Multi-electrode geometries for refined dielectric control of nanoelectromechanical systems," Master's thesis at Universität Konstanz (2017).

[65] A. Wallraff, D. I. Schuster, A. Blais, L. Frunzio, R.-S. Huang, J. Majer, S. Kumar, S. M. Girvin, and R. J. Schoelkopf, "Strong coupling of a single photon to a superconducting qubit using circuit quantum electrodynamics," Nature **431**, 162–167 (2004).

[66] S. Gröblacher, K. Hammerer, M. R. Vanner, and M. Aspelmeyer, "Observation of strong coupling between a micromechanical resonator and an optical cavity field," Nature **460**, 724–727 (2009).

[67] T. Kippenberg, H. Rokhsari, T. Carmon, A. Scherer, and K. Vahala, "Analysis of radiation-pressure induced mechanical oscillation of an optical microcavity," Physical Review Letters **95**, 033901 (2005).

[68] J. á. Reithmaier, G. Sęk, A. Löffler, C. Hofmann, S. Kuhn, S. Reitzenstein, L. Keldysh, V. Kulakovskii, T. Reinecke, and A. Forchel, "Strong coupling in a single quantum dot–semiconductor microcavity system," Nature **432**, 197–200 (2004).

[69] T. Yoshie, A. Scherer, J. Hendrickson, G. Khitrova, H. Gibbs, G. Rupper, C. Ell, O. Shchekin, and D. Deppe, "Vacuum Rabi splitting with a single quantum dot in a photonic crystal nanocavity," Nature **432**, 200–203 (2004).

[70] E. Peter, P. Senellart, D. Martrou, A. Lemaitre, J. Hours, J. Gérard, and J. Bloch, "Exciton-photon strong-coupling regime for a single quantum dot embedded in a microcavity," Physical review letters **95**, 067401 (2005).

[71] T. Aoki, B. Dayan, E. Wilcut, W. P. Bowen, A. S. Parkins, T. Kippenberg, K. Vahala, and H. Kimble, "Observation of strong coupling between one atom and a monolithic microresonator," Nature **443**, 671–674 (2006).

[72] J. P. Mathew, R. N. Patel, A. Borah, R. Vijay, and M. M. Deshmukh, "Dynamical strong coupling and parametric amplification of mechanical modes of graphene drums," Nature nanotechnology **11**, 747–751 (2016).

[73] T. Faust, J. Rieger, M. J. Seitner, P. Krenn, J. P. Kotthaus, and E. M. Weig, "Nonadiabatic dynamics of two strongly coupled nanomechanical resonator modes," Physical review letters **109**, 037205 (2012).

[74] K. Gajo, S. Schüz, and E. M. Weig, "Strong 4-mode coupling of nanomechanical string resonators," Applied Physics Letters **111**, 133109 (2017).

[75] L. Novotny, "Strong coupling, energy splitting, and level crossings: A classical perspective," American Journal of Physics **78**, 1199–1202 (2010).

[76] S. Tian, "Monte Carlo simulation of ion implantation in crystalline SiC with arbitrary polytypes," IEEE transactions on electron devices **55**, 1991–1996 (2008).

[77] S. Goel, A. Stukowski, X. Luo, A. Agrawal, and R. L. Reuben, "Anisotropy of single-crystal 3C–SiC during nanometric cutting," Modelling and Simulation in Materials Science and Engineering **21**, 065004 (2013).

[78] G. L. Harris, *Properties of silicon carbide*, 13 (Iet, 1995).

[79] C. Long, S. Ustin, and W. Ho, "Structural defects in 3C–SiC grown on Si by supersonic jet epitaxy," Journal of Applied Physics **86**, 2509–2515 (1999).

[80] K. Ashida, T. Kajino, Y. Kutsuma, N. Ohtani, and T. Kaneko, "Crystallographic orientation dependence of SEM contrast revealed by SiC polytypes," Journal of Vacuum Science & Technology B, Nanotechnology and Microelectronics: Materials, Processing, Measurement, and Phenomena **33**, 04E104 (2015).

[81] H. Matsunami, "Technological breakthroughs in growth control of silicon carbide for high power electronic devices," Japanese Journal of Applied Physics **43**, 6835 (2004).

[82] J. Li, Q. Wang, G. He, M. Widom, L. Nemec, V. Blum, M. Kim, P. Rinke, and R. M. Feenstra, "Formation of graphene atop a Si adlayer on the C-face of SiC," Physical Review Materials **3**, 084006 (2019).

[83] G. Fisher and P. Barnes, "Towards a unified view of polytypism in silicon carbide," Philosophical Magazine B **61**, 217–236 (1990).

[84] C. A. Zorman and R. J. Parro, "Micro-and nanomechanical structures for silicon carbide MEMS and NEMS," physica status solidi (b) **245**, 1404–1424 (2008).

[85] W. J. Choyke, H. Matsunami, and G. Pensl, *Silicon carbide: recent major advances* (Springer Science & Business Media, 2003).

[86] P. Rai-Choudhury and N. Formigoni, "β-Silicon Carbide Films," Journal of The Electrochemical Society **116**, 1440 (1969).

[87] S. Nishino, J. A. Powell, and H. A. Will, "Production of large-area single-crystal wafers of cubic SiC for semiconductor devices," Applied Physics Letters **42**, 460–462 (1983).

[88] M. Portail, M. Zielinski, T. Chassagne, S. Roy, and M. Nemoz, "Comparative study of the role of the nucleation stage on the final crystalline quality of (111) and (100) silicon carbide films deposited on silicon substrates.," Journal of Applied Physics **105**, 083505 (2009).

[89] H. Nagasawa and K. Yagi, "3C-SiC Single-Crystal Films Grown on 6-Inch Si Substrates," physica status solidi (b) **202**, 335–358 (1997).

[90] S. Nishino, H. Suhara, H. Ono, and H. Matsunami, "Epitaxial growth and electric characteristics of cubic SiC on silicon," Journal of applied physics **61**, 4889–4893 (1987).

[91] A. J. Steckl and J. Li, "Epitaxial growth of beta-SiC on Si by RTCVD with C3H8 and SiH4," IEEE transactions on electron devices **39**, 64–74 (1992).

[92] M. S. Hu and L. S. Hong, "Surface carbonization of Si (1 1 1) by C2H2 and the subsequent SiC (1 1 1) epitaxial growth from SiH4 and C2H2," Journal of crystal growth **265**, 382–389 (2004).

[93] P. Liaw and R. Davis, "Epitaxial Growth and Characterization of β-SiC Thin Films," Journal of the Electrochemical Society **132**, 642 (1985).

[94] A. Gupta, J. Sengupta, and C. Jacob, "An atomic force microscopy and optical microscopy study of various shaped void formation and reduction in 3C-SiC films grown on Si using chemical vapor deposition," Thin Solid Films **516**, 1669–1676 (2008).

[95] F. Iacopi, R. E. Brock, A. Iacopi, L. Hold, and R. H. Dauskardt, "Evidence of a highly compressed nanolayer at the epitaxial silicon carbide interface with silicon," Acta materialia **61**, 6533–6540 (2013).

[96] F. Iacopi, G. Walker, L. Wang, L. Malesys, S. Ma, B. V. Cunning, and A. Iacopi, "Orientation-dependent stress relaxation in hetero-epitaxial 3C-SiC films," Applied physics letters **102**, 011908 (2013).

[97] M. Zielinski, S. Ndiaye, T. Chassagne, S. Juillaguet, R. Lewandowska, M. Portail, A. Leycuras, and J. Camassel, "Strain and wafer curvature of 3C-SiC films on silicon: influence of the growth conditions," physica status solidi (a) **204**, 981–986 (2007).

[98] B. Hähnlein, M. Stubenrauch, S. Michael, and J. Pezoldt, "Mechanical properties and residual stress of thin 3C-SiC (111) films determined using MEMS structures," in Materials Science Forum, Vol. 778 (Trans Tech Publ, 2014), pp. 444–448.

[99] B. Hähnlein, M. Stubenrauch, and J. Pezoldt, "Mechanical properties and residual stress of thin 3C-SiC (100) films determined using MEMS structures," in Materials Science Forum, Vol. 821 (Trans Tech Publ, 2015), pp. 281–284.

[100] V. Kulikovsky, V. Vorlíček, P. Boháč, M. Stranyánek, R. Čtvrtlík, A. Kurdyumov, and L. Jastrabik, "Hardness and elastic modulus of amorphous and nanocrystalline SiC and Si films," Surface and Coatings Technology **202**, 1738–1745 (2008).

[101] M. Bückle, V. C. Hauber, G. D. Cole, C. Gärtner, U. Zeimer, J. Grenzer, and E. M. Weig, "Stress control of tensile-strained $In_{1-x}Ga_xP$ nanomechanical string resonators," Applied Physics Letters **113**, 201903 (2018).

[102] L. Pakula, H. Yang, H. Pham, P. French, and P. Sarro, "Fabrication of a CMOS compatible pressure sensor for harsh environments," Journal of Micromechanics and Microengineering **14**, 1478 (2004).

[103] M. Zielinski, A. Leycuras, S. Ndiaye, and T. Chassagne, "Stress relaxation during the growth of 3 C-Si C/ Si thin films," Applied physics letters **89**, 131906 (2006).

[104] J. Kölbl, "Kohärente Dynamik von gekoppelten nanomechanischen Resonatormoden," Master's thesis at Universität Konstanz (2015).

[105] P. Panduranga, A. Abdou, Z. Ren, R. H. Pedersen, and M. P. Nezhad, "Isotropic silicon etch characteristics in a purely inductively coupled SF6 plasma," Journal of Vacuum Science & Technology B, Nanotechnology and Microelectronics: Materials, Processing, Measurement, and Phenomena **37**, 061206 (2019).

[106] V. M. Donnelly, "Reactions of fluorine atoms with silicon, revisited, again," Journal of Vacuum Science & Technology A: Vacuum, Surfaces, and Films **35**, 05C202 (2017).

[107] H. Jansen, H. Gardeniers, M. de Boer, M. Elwenspoek, and J. Fluitman, "A survey on the reactive ion etching of silicon in microtechnology," Journal of micromechanics and microengineering **6**, 14 (1996).

[108] K. Bordo and H.-G. Rubahn, "Effect of deposition rate on structure and surface morphology of thin evaporated Al films on dielectrics and semiconductors," Materials Science **18**, 313–317 (2012).

[109] I. Shah, A. Koekkoek, W. Van Enckevort, and E. Vlieg, "Influence of additives on alkaline etching of silicon (111)," Crystal growth & design **9**, 4315–4323 (2009).

[110] H. Seidel, L. Csepregi, A. Heuberger, and H. Baumgärtel, "Anisotropic etching of crystalline silicon in alkaline solutions: I. Orientation dependence and behavior of passivation layers," Journal of the electrochemical society **137**, 3612 (1990).

[111] P. Brack, S. Dann, K. Wijayantha, P. Adcock, and S. Foster, "An assessment of the viability of hydrogen generation from the reaction of silicon powder and sodium hydroxide solution for portable applications," International Journal of Energy Research **41**, 220–228 (2017).

[112] S. Campbell, K. Cooper, L. Dixon, R. Earwaker, S. Port, and D. Schiffrin, "Inhibition of pyramid formation in the etching of Si p (100) in aqueous potassium hydroxide-isopropanol," Journal of Micromechanics and Microengineering **5**, 209 (1995).

[113] K. Sato, M. Shikida, Y. Matsushima, T. Yamashiro, K. Asaumi, Y. Iriye, and M. Yamamoto, "Characterization of orientation-dependent etching

properties of single-crystal silicon: effects of KOH concentration," Sensors and Actuators A: Physical **64**, 87–93 (1998).

[114] K. Biswas and S. Kal, "Etch characteristics of KOH, TMAH and dual doped TMAH for bulk micromachining of silicon," Microelectronics journal **37**, 519–525 (2006).

[115] T. R. Albrecht, P. Grütter, D. Horne, and D. Rugar, "Frequency modulation detection using high-Q cantilevers for enhanced force microscope sensitivity," Journal of applied physics **69**, 668–673 (1991).

[116] M. Higgins, R. Proksch, J. E. Sader, M. Polcik, S. Mc Endoo, J. Cleveland, and S. Jarvis, "Noninvasive determination of optical lever sensitivity in atomic force microscopy," Review of Scientific Instruments **77**, 013701 (2006).

[117] T. B. Gabrielson, "Mechanical-thermal noise in micromachined acoustic and vibration sensors," IEEE transactions on Electron Devices **40**, 903–909 (1993).

[118] F. Nägele, "Fabrication and Characterisation of High Q Nanomechanical Resonators made from Highly Stressed 3C-SiC," Master's thesis at Universität Konstanz (2020).

[119] J. S. Ochs, "Nonlinear and noise-induced dynamics of high Q nanomechanical resonators," PhD thesis at the Universität of Konstanz (2021).

[120] H. Guo and A. Lal, "Characterization of micromachined silicon nitride membrane using resonant ultrasound spectroscopy," in 2001 IEEE Ultrasonics Symposium. Proceedings. An International Symposium (Cat. No. 01CH37263), Vol. 2 (IEEE, 2001), pp. 863–866.

[121] T.-Y. Zhang, Y.-J. Su, C.-F. Qian, M.-H. Zhao, and L.-Q. Chen, "Microbridge testing of silicon nitride thin films deposited on silicon wafers," Acta materialia **48**, 2843–2857 (2000).

[122] R. Edwards, G. Coles, and W. Sharpe, "Comparison of tensile and bulge tests for thin-film silicon nitride," Experimental Mechanics **44**, 49–54 (2004).

[123] W.-H. Chuang, T. Luger, R. K. Fettig, and R. Ghodssi, "Mechanical property characterization of LPCVD silicon nitride thin films at cryogenic temperatures," Journal of Microelectromechanical Systems **13**, 870–879 (2004).

[124] O. Tabata, K. Kawahata, S. Sugiyama, and I. Igarashi, "Mechanical property measurements of thin films using load-deflection of composite rectangular membranes," Sensors and actuators **20**, 135–141 (1989).

[125] T. Yoshioka, T. Ando, M. Shikida, and K. Sato, "Tensile testing of SiO2 and Si3N4 films carried out on a silicon chip," Sensors and Actuators A: Physical **82**, 291–296 (2000).

[126] O. Maillet, X. Zhou, R. Gazizulin, A. M. Cid, M. Defoort, O. Bourgeois, and E. Collin, "Nonlinear frequency transduction of nanomechanical Brownian motion," Physical Review B **96**, 165434 (2017).

[127] P. Sadeghi, M. Tanzer, S. L. Christensen, and S. Schmid, "Influence of clamp-widening on the quality factor of nanomechanical silicon nitride resonators," Journal of Applied Physics **126**, 165108 (2019).

[128] Y. Tsaturyan, A. Barg, E. S. Polzik, and A. Schliesser, "Ultracoherent nanomechanical resonators via soft clamping and dissipation dilution," Nature Nanotechnology **12**, 776–783 (2017).

[129] J. Chan, M. Eichenfield, R. Camacho, and O. Painter, "Optical and mechanical design of a "zipper" photonic crystal optomechanical cavity," Optics Express **17**, 3802–3817 (2009).

[130] R. J. Meyer and L. Gmelin, *Gmelins Handbuch der anorganischen chemie* (Verlag Chemie gmbh, Weinheim, 1926).

[131] K. Pestka, J. Maynard, D. Gao, and C. Carraro, "Measurement of the elastic constants of a columnar SiC thin film," Physical review letters **100**, 055503 (2008).

[132] Z. Li and R. C. Bradt, "The single-crystal elastic constants of cubic (3C) SiC to 1000 C," Journal of materials science **22**, 2557–2559 (1987).

[133] C.-Z. Wang, R. Yu, and H. Krakauer, "Pressure dependence of Born effective charges, dielectric constant, and lattice dynamics in SiC," Physical Review B **53**, 5430 (1996).

[134] K. Karch, P. Pavone, W. Windl, O. Schütt, and D. Strauch, "Ab initio calculation of structural and lattice-dynamical properties of silicon carbide," Physical Review B **50**, 17054 (1994).

[135] A. Bachtold, J. Moser, and M. Dykman, "Mesoscopic physics of nanomechanical systems," arXiv preprint arXiv:2202.01819 (2022).

[136] M. Aspelmeyer, T. J. Kippenberg, and F. Marquardt, "Cavity optomechanics," Reviews of Modern Physics **86**, 1391 (2014).

[137] P. Delsing, A. N. Cleland, M. J. Schuetz, J. Knörzer, G. Giedke, J. I. Cirac, K. Srinivasan, M. Wu, K. C. Balram, C. Bäuerle, et al., "The 2019 surface acoustic waves roadmap," Journal of Physics D: Applied Physics **52**, 353001 (2019).

[138] A. Clerk, K. Lehnert, P. Bertet, J. Petta, and Y. Nakamura, "Hybrid quantum systems with circuit quantum electrodynamics," Nature Physics **16**, 257–267 (2020).

[139] S. Volz, J. Ordonez-Miranda, A. Shchepetov, M. Prunnila, J. Ahopelto, T. Pezeril, G. Vaudel, V. Gusev, P. Ruello, E. M. Weig, et al., "Nanophononics: state of the art and perspectives," The European Physical Journal B **89**, 1–20 (2016).

[140] M. Perdriat, C. Pellet-Mary, P. Huillery, L. Rondin, and G. Hétet, "Spin-mechanics with nitrogen-vacancy centers and trapped particles," Micromachines **12**, 651 (2021).

[141] K. Babaei Gavan, H. J. Westra, E. W. van der Drift, W. J. Venstra, and H. S. van der Zant, "Size-dependent effective Young's modulus of silicon nitride cantilevers," Applied Physics Letters **94**, 233108 (2009).

[142] D. Schneider and M. Tucker, "Non-destructive characterization and evaluation of thin films by laser-induced ultrasonic surface waves," Thin Solid Films **290**, 305–311 (1996).

[143] S. Schmid, K. Jensen, K. Nielsen, and A. Boisen, "Damping mechanisms in high-Q micro and nanomechanical string resonators," Physical Review B **84**, 165307 (2011).

[144] M. Bao, *Analysis and design principles of MEMS devices* (Elsevier, 2005).

[145] M. A. Hopcroft, W. D. Nix, and T. W. Kenny, "What is the Young's Modulus of Silicon?" Journal of microelectromechanical systems **19**, 229–238 (2010).

[146] R. Gross and A. Marx, *Festkörperphysik* (Walter de Gruyter GmbH & Co KG, 2014).

[147] J. F. Nye et al., *Physical properties of crystals: their representation by tensors and matrices* (Oxford university press, 1985).

[148] W. Lambrecht, B. Segall, M. Methfessel, and M. Van Schilfgaarde, "Calculated elastic constants and deformation potentials of cubic SiC," Physical Review B **44**, 3685 (1991).

[149] N. Maluf and K. Williams, *An introduction to microelectromechanical systems engineering* (Artech House, Norwood, 2004).

[150] S. M. Sze, Y. Li, and K. K. Ng, *Physics of semiconductor devices* (John wiley & sons, New York, 2021).

[151] S.-L. Zhang, J.-T. Wang, W. Kaplan, and M. Östling, "Silicon nitride films deposited from SiH_2C_{12}-NH_3 by low pressure chemical vapor deposition: kinetics, thermodynamics, composition and structure," Thin Solid Films **213**, 182–191 (1992).

[152] H. K. Henisch and R. Roy, *Silicon Carbide 1968 - Proceedings of the International Conference on Silicon Carbide* (Elsevier, New York, 2013).

[153] M. S. Shur, M. Levinshtein, and S. Rumyantsev, *Handbook Series on Semiconductor Parameters, Vol. 2: Ternary and Quaternary III-V Compounds*, Vol. 2, See also: http://www.ioffe.ru/SVA/NSM/ (World Scientific Publishing Co, Singapore, 1999).

[154] S. Hong, T. Weihs, J. Bravman, and W. Nix, "Measuring stiffnesses and residual stresses of silicon nitride thin films," Journal of Electronic Materials **19**, 903–909 (1990).

[155] T. Taylor and F. Yuan, "Thermal stress and fracture in shear-constrained semiconductor device structures," IRE Transactions on Electron Devices **9**, 303–308 (1962).

[156] E. Suhir and M. Vujosevic, "Interfacial stresses in a bi-material assembly with a compliant bonding layer," Journal of Physics D: Applied Physics **41**, 115504 (2008).

[157] M. J. Bereyhi, A. Beccari, S. A. Fedorov, A. H. Ghadimi, R. Schilling, D. J. Wilson, N. J. Engelsen, and T. J. Kippenberg, "Clamp-Tapering Increases the Quality Factor of Stressed Nanobeams," Nano Letters **19**, 2329–2333 (2019).

[158] J. Yang and O. Paul, "Fracture properties of LPCVD silicon nitride thin films from the load–deflection of long membranes," Sensors and Actuators A: Physical **97-98**, 520–526 (2002).

[159] A. Kaushik, H. Kahn, and A. Heuer, "Wafer-level mechanical characterization of silicon nitride MEMS," Journal of Microelectromechanical Systems **14**, 359–367 (2005).

[160] M. Kajima, N. Kusumi, S. Moriwaki, and N. Mio, "Wide-band measurement of mechanical thermal noise using a laser interferometer," Physics Letters A **264**, 251–256 (1999).

[161] A. Bernardini, E. Majorana, Y. Ogawa, P. Puppo, P. Rapagnani, F. Ricci, and G. Testi, "Characterization of mechanical dissipation spectral behavior using a gravitomagnetic pendulum," Physics Letters A **255**, 142–146 (1999).

[162] I. Wilson-Rae, R. Barton, S. Verbridge, D. Southworth, B. Ilic, H. G. Craighead, and J. Parpia, "High-Q nanomechanics via destructive interference of elastic waves," Physical review letters **106**, 047205 (2011).

[163] I. Wilson-Rae, "Intrinsic dissipation in nanomechanical resonators due to phonon tunneling," Physical Review B **77**, 245418 (2008).

[164] D. Tielbürger, R. Merz, R. Ehrenfels, and S. Hunklinger, "Thermally activated relaxation processes in vitreous silica: An investigation by Brillouin scattering at high pressures," Physical review B **45**, 2750 (1992).

[165] R. O. Pohl, X. Liu, and E. Thompson, "Low-temperature thermal conductivity and acoustic attenuation in amorphous solids," Reviews of Modern Physics **74**, 991 (2002).

[166] B. Zink, R. Pietri, and F. Hellman, "Thermal conductivity and specific heat of thin-film amorphous silicon," Physical review letters **96**, 055902 (2006).

[167] R. Vacher, E. Courtens, and M. Foret, "Anharmonic versus relaxational sound damping in glasses. II. Vitreous silica," Physical Review B **72**, 214205 (2005).

[168] T. Faust, J. Rieger, M. J. Seitner, J. P. Kotthaus, and E. M. Weig, "Signatures of two-level defects in the temperature-dependent damping of nanomechanical silicon nitride resonators," Physical Review B **89**, 100102 (2014).

[169] T. Middelmann, A. Walkov, G. Bartl, and R. Schödel, "Thermal expansion coefficient of single-crystal silicon from 7 K to 293 K," Physical Review B **92**, 174113 (2015).

[170] H. Ibach, "Thermal expansion of silicon and zinc oxide (I)," physica status solidi (b) **31**, 625–634 (1969).

[171] C. Swenson, "Recommended values for the thermal expansivity of silicon from 0 to 1000 K," Journal of physical and chemical reference data **12**, 179–182 (1983).

[172] D. Talwar and J. C. Sherbondy, "Thermal expansion coefficient of 3C–SiC," Applied physics letters **67**, 3301–3303 (1995).

[173] M. Kazan, G. Guisbiers, S. Pereira, M. Correia, P. Masri, A. Bruyant, S. Volz, and P. Royer, "Thermal conductivity of silicon bulk and nanowires: Effects of isotopic composition, phonon confinement, and surface roughness," Journal of Applied Physics **107**, 083503 (2010).

[174] A. Sparavigna, "Role of nonpairwise interactions on phonon thermal transport," Physical Review B **67**, 144305 (2003).

[175] T. Ruf, R. Henn, M. Asen-Palmer, E. Gmelin, M. Cardona, H.-J. Pohl, G. Devyatych, and P. Sennikov, "Thermal conductivity of isotopically enriched silicon," Solid State Communications **115**, 243–247 (2000).

[176] R. Riviere, S. Deleglise, S. Weis, E. Gavartin, O. Arcizet, A. Schliesser, and T. J. Kippenberg, "Optomechanical sideband cooling of a micromechanical oscillator close to the quantum ground state," Physical Review A **83**, 063835 (2011).

[177] F. David, "Fabrication and characterization of nanomechanical resonators based on silicon carbide," Master's thesis at Technical University Munich (TUM) (2022).

[178] A. T. Le, A. Brieussel, and E. M. Weig, "Room temperature cavity electromechanics in the sideband-resolved regime," Journal of Applied Physics **130**, 014301 (2021).

[179] S. Kumar, Y. Klaß, B. Alperin, S. Venkatachalam, X. Zhou, E. Weig, E. Collin, and A. Fefferman, "Microwave optomechanical measurement of non-metallized SiN strings at mK temperatures," arXiv preprint arXiv:2110.00228 (2021).

[180] V. Blavy, "Spectral characterization of noise-induced motion in a weakly damped driven nanostring resonator," lab report (2021).

[181] M. Salapaka, H. Bergh, J. Lai, A. Majumdar, and E. McFarland, "Multi-mode noise analysis of cantilevers for scanning probe microscopy," Journal of Applied Physics **81**, 2480–2487 (1997).

[182] L. V. Ahlfors, "Complex analysis: an introduction to the theory of analytic functions of one complex variable," New York, London **177** (1953).

Acknowledgment

First and foremost, I want to thank you, Eva, for giving me the opportunity to work for more than four years on this exciting project. Your constant support and expertise guided me on my long journey to this thesis. No matter the problem, you always had an open ear and found some time for helpful discussions. I really enjoyed working in your group; thank you!

Thank you, Elke, for your mentoring and for reading and reviewing my thesis.

Thank you, Prof. Dr.-Ing. Christian Jirauschek for taking the chair of my examining committee.

Of course, a very special thank you goes to you, Susi. You keep several chairs and a complete building alive with your vitality, energy, and organization. Moreover, you notified me that I have to hand in within the next three weeks :-).

A thank you goes to you, Ignacio. It was very inspiring to work with a theorist of your class. I wish you a fast and complete recovery, my friend! Also I'm very grateful that you allowed me to use your unpublished theory in this work.

Thank you Nagesh, Artur, Georgy, and Jens from the Helmholtz-Zentrum Dresden-Rossendorf for the very nice collaboration. I enjoyed our work and fruitful discussions. A special thanks goes to Nagesh, who organized the meetings and helped with reminder emails.

I also want to thank our collaborators Andrew Fefferman, Sumit Kumar, Xin Zhou, and Eddy Collin from France. We had a hard time with the fabrication of the aluminum electrodes, but in the end, it worked out very nicely.

Thank you to Matthias and Gillian, the masters of the Nanolab in Konstanz. No matter the problem, you always solved it quickly! We had a lot of fun, especially disposing all the leftover chemicals before moving to Munich.

Another very special thanks goes to my two master's students, Felix and Felix. I enjoyed every minute of working with you, and together we promoted SiC to the group. Thanks also to Vincent Blavy for joining our group for an internship.

And of course, I want to thank the fantastic NQS group and all the former members from Konstanz: (in no particular order) Avi, Tuan, Irene, Berke, Berke, Jonny, Ahmed, Philipp, Maximilian, Katrin, Jana, Juliane, Louis, David, Alex, and last but not least, Felix (David), Felix (Nägele), Felix (Eichin), and Felix (Rochau). It was a pleasure working with you and together we enjoyed countless of cakes, self-made nitrogen ice cream, bar events, lunch breaks, coffee breaks, and restaurant visits. Oddly, it was mostly about food, I realize now ;-). The wine festivals in Konstanz are also legendary. Tuan, our visit to the FNS and LA is unforgettable, especially with the "free" upgrade to our 300-hp car. Berke (2x), I really enjoy your culinary input to the group, be it donuts, baklava, or sucuk. Maximilian, your LN2 ice creams were nothing but spectacular. When we were not eating, we pondered over our length-dependent stress model. Jana, I really enjoyed our joint trips to Munich. We had a fantastic time discovering all the features of the different cars. Louis, the master of all parts bigger than a few millimeters, it was inspiring to see how you solved all the small (or big) mechanical issues we had in the lab. In the last months, you also served as a post office in Konstanz; thank you. Hopefully, your hamstring is recovering quickly.

Irene, saying thank you doesn't do it justice. You (nearly) single-handedly corrected my thesis and provided me with hundreds of valuable comments, tips, and insights. Thank you so much! We spend uncountable evenings dining, drinking cinque terre, and playing board games. You're also our sole provider for jamon, chorizo, lomo, and (very recently) lazy lomo. Thank you for keeping me alive in the last three weeks of writing my thesis :-).

Sophia, thank you for the wonderful nine years and hopefully many more to come. Thank you for proofreading my thesis and finding some embarrassing mistakes. Thank you for solving all the mathematical problems I encountered during my PhD project. And thank you for your constant support and for tolerating Penelope beside our bed ;-).

And last but not least, I want to thank my family. Your lifelong support allowed me to conquer this PhD-project; thank you so much.